UNIVERSITY OF CALIFORNIA SAN DIEGO

Time-series of stable isotopes in dissolved inorganic carbon of surface seawater near Bermuda and Hawaii

A dissertation submitted in partial satisfaction of the requirements for the degree Doctor of Philosophy

in

Oceanography

by

Mariela Ke'o-lani Brooks

Committee in charge:

Professor Ralph F. Keeling, Chair
Professor Andreas J. Andersson
Professor Elsa Cleland
Professor Andrew G. Dickson
Professor Janet Sprintall

2020

The Dissertation of Mariela Ke'o-lani Brooks is approved, and it is acceptable in quality and form for publication on microfilm and electronically:

Chair

University of California San Diego

2020

EPIGRAPH

There is an art to flying… or rather a knack.
The knack lies in learning how to throw yourself at the ground and miss.
– Douglas Adams, The Hitchhiker's Guide to the Galaxy

With every drop of water you drink, every breath you take,
you're connected to the sea, no matter where on Earth you live.
– Sylvia Earle

TABLE OF CONTENTS

LIST OF FIGURES

LIST OF TABLES

ACKNOWLEDGEMENTS

I need to start by thanking my PhD advisor, Ralph Keeling, whose support, guidance, and feedback have been invaluable. Thank you for always challenging me to improve my understanding and scientific thinking. I'd like to also thank my committee members: Andreas Andersson, Elsa Cleland, Andrew Dickson, and Janet Sprintall, each of whom have contributed to my dissertation work in many ways. I appreciate your encouragement, willingness to share advice, and your help in making me a better scientist.

Thank you to the Keeling Lab members, past and present. Special thanks to Tim Lueker who, throughout my time at Scripps, has been a constant advocate and source of support and guidance for me. Whether it was brainstorming ideas, helping me make new seawater standards, doing seawater extractions and measuring DIC, being supportive even when I broke things (R.I.P. GES1), or just hearing me out, thank you for always being there with words of encouragement and perspective. Thank you to Alane Bollenbacher who, among many other things, helped to teach me the inner workings of running isotope samples on the Keeling Lab mass spectrometer and helped to demystify the seawater isotope program, archived samples, and standards.

I would also like to acknowledge and thank Andrew Dickson, Guy Emanuele, and the Dickson Lab for all of the work they have contributed to maintaining the Scripps seawater time-series record. In addition, I would like to thank the Bermuda Institute for Ocean Science (BIOS) and Hawaii Ocean Time-series (HOT) station personnel without whom these samples could not have been collected and this dataset would not be possible. The BIOS and HOT programs also measure and maintain independent station data for each of their respective time-series which have provided supporting data for understanding the wider influences on our time-series data.

Thank you to NCAR and the CESM community for providing support via the University Graduate Student Allocation and for allowing us to use model output and computing resources during this project. Special thanks to Matthew Long at NCAR for being patient and willing to provide mentorship, guidance, and advice to improve my abilities as a scientist and writer.

During my time at Scripps I have been supported financially by a variety of sources to conduct research and participate in conferences and workshops. These include the E.W. Scripps Fellowship, the National Science Foundation, the Schmidt Foundation, SIO department travel funds, and the many other donors who made it possible for me to take advantage of incredible opportunities like attending the UNFCCC COP21 in Paris. My research and these experiences would not have been possible without this financial support and I am incredibly grateful.

Thank you to all of my friends and the SIO community who help to make this place an incredible place to work (and play). My time here would not have been the same without you all. I also owe many thanks to everyone in the graduate office who work tirelessly to support the graduate students and community at SIO.

Thank you to my family for always supporting me in pursuing my dreams to learn and understand the world around me better. Mom, Dad, Barrow, Kalima, and Ashley, I could not have done this without you. Special thanks to my beautiful niece, Mila Nāhi'ōle'a Brooks, who was born toward the end of this PhD journey and has brought incredible and unimaginable joy to me in this final stretch. Thank you, Liz, Jim, and Hobbes for giving me a place to seek refuge in San Diego, and always making me feel at home. Thank you to Abby, Charley, Max, Caleb, and Molly for all of the additional family fun and support these last few years. Thank you to Jayme, you've been by my side through all the ins and outs and in betweens, and for that I am forever grateful.

Special thanks to John Harley for being such a wonderful and supportive partner. You've been there for me in all of the ups and downs, to encourage me whether things went as expected or not, including when I crashed my hard drive (twice) and promptly deleted my back-up, and the other numerous pitfalls and challenges along the way. Thank you for always believing in me, for reminding me of the importance of saving things in multiple locations, and believing that this was possible, even (and especially) when I didn't believe it myself. Words cannot express how grateful I am to have you in my life.

Countless friends and family in San Diego and beyond have provided encouragement and support, and I could not have done this without all of you. Thank you!

Chapter 2, in part is currently being prepared for submission for publication of the material. Brooks, Mariela K.; Lueker, Timothy J.; Bollenbacher, Alane F.; Walker, Stephen J.; Dickson, Andrew G.; Emanuele III, Guy; Keeling, Ralph F. The dissertation author was the primary investigator and author of this material.

Chapter 3, in part is currently being prepared for submission for publication of the material. Brooks, Mariela K.; Lueker, Timothy J.; Dickson, Andrew G., Emanuele III, Guy; Bollenbacher, Alane; Keeling, Ralph F. The dissertation author was the primary investigator and author of this material.

Chapter 4, in part is currently being prepared for submission for the publication of the material. Brooks, Mariela K.; Long, Matthew C.; Keeling, Ralph F. The dissertation author was the primary investigator and author of this material.

VITA

2011	Bachelor of Science (Physics), Portland State University
2011 – 2012	Laboratory Technician, Portland State University
2012 – 2019	Graduate Student Researcher, University of California San Diego
2014	Master of Science (Earth Sciences), University of California San Diego
2018	Teaching Assistant, University of California San Diego
2020	Doctor of Philosophy (Oceanography), University of California San Diego

ABSTRACT OF THE DISSERTATION

Time-series of stable isotopes in dissolved inorganic carbon
of surface seawater near Bermuda and Hawaii

by

Mariela Ke'o-lani Brooks

Doctor of Philosophy in Oceanography

University of California San Diego, 2020

Professor Ralph F. Keeling, Chair

The $^{13}C/^{12}C$ ratio of stable carbon isotopes in dissolved inorganic carbon (DIC) can provide insight into carbon cycle variability and trends in the surface ocean. Measurements of $\delta^{13}C$-DIC when combined with DIC can be used to estimate anthropogenic carbon uptake and marine productivity and can contribute to our understanding of the role that the ocean plays in the global carbon cycle. This dissertation describes surface ocean time-series measurements near Bermuda (S-BATS) and Hawaii (HOT) of $\delta^{13}C$-DIC, DIC, and alkalinity (ALK) as a part of the

Scripps Seawater Program, focusing on δ^{13}C-DIC. Prior to this study, there was a hiatus in seawater δ^{13}C-DIC measurements at Scripps, while samples continued to be collected and archived for future analysis. This dissertation details the resumption of these measurements along with the calibration and methodology used for Scripps measurements of δ^{13}C-DIC. We quantify the calibration contributions to uncertainty in the context of consistency between newer and older measurements. In addition, we introduce and document the stability of three new seawater secondary standards, including a method based on CO_2 in compressed N_2 gas.

In these time-series records of nearly three decades, we show that the long-term trends and seasonal cycles in sDIC and δ^{13}C-DIC at both S-BATS and HOT are consistent with earlier studies and independent time-series records. From the full record we find no long-term changes in the seasonal cycle of sDIC, δ^{13}C-DIC, or computed pCO_2. Consistent to some earlier studies we find significant correlations at S-BATS with the North Atlantic Oscillation and at HOT with the Pacific Decadal Oscillation (PDO). We also find correlations at HOT that were not previously noted including the PDO with sea surface temperature and mixed layer depth (MLD), as well as El Nino Southern Oscillation (NINO3.4) with sDIC and MLD. Lastly, we use a combination of observations and CESM hindcast simulations to explore upper ocean carbon variability in subtropical gyres. This allows us to examine the time-series in a broader geographic context, showing coherent patterns of variability across the North Atlantic and North Pacific subtropical gyres and illustrating key differences in the controls of variability at BATS and HOT.

CHAPTER 1: INTRODUCTION

1.1 THE CARBON CYCLE AND SUBTROPICAL GYRES

The global carbon cycle has three primary reservoirs; the atmosphere, the terrestrial biosphere, and the ocean. The natural state of the carbon cycle is maintained through a relative balance between these carbon reservoirs. Anthropogenic perturbation of the carbon cycle resulting from fossil fuel burning, land use changes, and cement production have disturbed this balance and resulted in a significant increase of atmospheric CO_2, a major greenhouse gas. As atmospheric levels of CO_2 continue to rise, it is increasingly important to be able to predict the resulting response of the global carbon cycle which has significant implications for predictions of future climate change. The ocean plays a critical role in the global carbon cycle and it is especially important to improve our understanding of how marine carbon uptake and storage may respond to climate change (Quay et al., 2003; Sabine and Tanhua, 2010). An important side effect of the uptake of anthropogenic CO_2 by the ocean is that the process by which it enters the ocean lowers seawater *p*H, resulting in ocean acidification (Bates et al., 2014; Caldeira and Wickett, 2003; Zeebe, 2012). According to recent estimates, ~45% of the anthropogenic carbon emissions remain in the atmosphere, while ~30% are removed by the land, and ~24% enter the ocean (Le Queré et al., 2018). An illustration of the global carbon budget with dominant sources and sinks is shown in Figure 1.1.

The Scripps seawater program time-series measurements of dissolved inorganic carbon (DIC), total alkalinity (ALK), and $^{13}C/^{12}C$ of DIC ($\delta^{13}C$-DIC) began as part of an effort to better understand the carbon cycle in the subtropical gyre regions of the ocean. The Subtropical gyres encompass over 40% of the surface oceans (Karl, 2002, 1999) and these highly stratified, oligotrophic regions are important for the global carbon cycle due to the significant surface area

of the ocean that they cover. The subtropical gyres could be responsible for as much as 60% of global organic carbon export from the surface ocean (Quay and Stutsman, 2003). There is also significant interannual variability, up to 50% of the total signal, in subtropical carbon export and anthropogenic carbon uptake rates (Bates, 2007; Brix et al., 2004; Gruber et al., 2002; Quay and Stutsman, 2003). Understanding productivity and anthropogenic carbon uptake and how this may be changing over time is important for predicting how these regions may be impacted by climate change as well as global carbon climate feedbacks.

1.2 STABLE CARBON ISOTOPES

Within the surface ocean, dissolved inorganic carbon (DIC) and the $^{13}C/^{12}C$ ratio of dissolved inorganic carbon ($\delta^{13}C$-DIC) are both influenced by physical and biological processes which include air-sea gas exchange, lateral mixing and advection, vertical mixing and diffusion, photosynthesis and respiration (Figure 1.2), as well as calcification and dissolution. We ignore the impacts of calcification and dissolution on DIC and $\delta^{13}C$-DIC when ALK remains relatively constant (Keeling et al., 2004; Chapter 3). Each of these processes changes the $\delta^{13}C$-DIC in a distinct and unique way, and high precision measurements of $\delta^{13}C$-DIC are a powerful tool for understanding how each of these processes cause changes in the upper ocean carbon cycle (Bacastow et al., 1996; Gruber et al., 2002, 1998; Keeling et al., 2004; Quay et al., 2017, 2007; Quay and Stutsman, 2003). Changes in the $^{13}C/^{12}C$ ratio are normally expressed in delta notation ($\delta^{13}C$), defined as:

$$\delta^{13}C = \left(\frac{\left(^{13}C/^{12}C\right)_s}{\left(^{13}C/^{12}C\right)_r} - 1\right) \cdot 1000 \tag{1.1}$$

where subscript *s* designates the sample, subscript *r* is the reference, and the factor of 1000 converts to per mil units (‰).

A notable contribution to our understanding of ocean uptake of anthropogenic carbon results from δ^{13}C-DIC records (Bacastow et al., 1996; Gruber et al., 1999; Heimann and Maier-Reimer, 1996; Körtzinger et al., 2003; McNeil et al., 2001; Quay et al., 2003; Sonnerup et al., 1999; Tanaka et al., 2003; Tans et al., 1993; Watanabe et al., 2011). The burning of fossil fuels leaves a signature of ^{13}C depletion in the atmospheric $\delta^{13}C_{atm}$ of CO_2, and this depleted $\delta^{13}C_{atm}$ signal is transferred into the surface mixed layer DIC during air-sea gas exchange and/or atom-swapping. There is a difference of about an order of magnitude in the equilibration timescales for DIC (~1 year) and δ^{13}C-DIC (~10 years). Thus, a decadal "smoothing" of the trend in seawater incorporation of anthropogenic carbon is reflected in the δ^{13}C-DIC (Bacastow et al., 1996; Lynch-Steiglitz et al., 1995).

The δ^{13}C-DIC and DIC time-series have also been used to study upper ocean biogeochemistry as it relates to net ecosystem and export production, as well as to calculate carbon budget estimates in the marine environment (Brix et al., 2004; Gruber et al., 2002, 1998; Keeling et al., 2004; Quay and Stutsman, 2003). These studies used upper ocean box models which take advantage of the simultaneous measurements of DIC and δ^{13}C-DIC, combined with additional relevant physical and chemical parameters. These box models allow the quantification of the dominant processes that control the upper ocean carbon cycle. It is thus possible to estimate the relative strength of air-sea gas exchange, net community production (NCP), horizontal advection, and vertical entrainment on the upper ocean carbon cycle.

There has also been research into how organismal photosynthetic fractionation may be changing over time as the atmospheric isotopic pool of $\delta^{13}C_{atm}$ is depleted and the background concentrations of atmospheric CO_2 and DIC continue to increase (Jasper and Hayes, 1990; Rau, 1989). The Scripps seawater program δ^{13}C-DIC time-series records provide the opportunity to

further explore these ideas and examine how these changes may show up in the marine environment. Additionally, it is possible to make use of these time-series datasets to study the impacts of ocean acidification. As the records grow longer, our ability to further our understanding and discover new information about long-term climate impacts increases as well. These time-series records can also be used to reduce uncertainties in ocean budget estimates and improve important validation checks to help constrain global earth system models which attempt to depict feedbacks between changing greenhouse gases and climate.

1.3 HISTORY OF SCRIPPS SEAWATER TIME-SERIES MEASUREMENTS

The Scripps seawater program started in 1983 in collaboration with the on-going time-series measurement program of the Bermuda Institute for Ocean Science (BIOS) (originally the Bermuda Biological Station for Research (BBSR)) at Hydrostation S in an effort to characterize inorganic carbon chemistry in the upper ocean. Since then, seawater bottle samples have been collected at roughly monthly time intervals and shipped to Scripps for analysis. The Scripps seawater measurements include dissolved inorganic carbon (DIC), alkalinity (ALK), and the stable isotopic ratio $^{13}C/^{12}C$ of DIC ($\delta^{13}C$-DIC). In 1988, the Scripps seawater program expanded to also obtain samples from the Hawaii Ocean Time-series (HOT) Station ALOHA as well as samples from the Bermuda Atlantic Time-series Study (BATS). Samples were obtained at two depths for each station (1 m and 10 m for BATS and Station S, 5 m and 25 m for HOT Station ALOHA) until 2004. Since then, samples have been obtained from a single sample depth for each station (10 m for BATS and Station S, 5 m for HOT Station ALOHA).

From 2005 to 2014 ALK and DIC measurements were continued primarily by Professor Andrew Dickson and members of his research group. Since ~2015, DIC measurements have been made by members of Professor Ralph Keeling's group while ALK measurements continue

to be made by members of Prof. Dickson's group. Since 2005, the CO_2 group led by Prof. Keeling has been responsible for the isotopic analysis. At the beginning of this project, measurements of δ^{13}C-DIC had fallen behind and were not available beyond 2004. During this measurement hiatus, the Scripps Seawater Program continued to have seawater samples collected. At the onset of this project, over 200 of these samples had been extracted, with the CO_2 gas samples collected in break seal tubes and archived for analysis at a future date to extend the isotopic time-series record. Additional seawater sample bottles from the more recent years had also been stored, awaiting analysis. As a part of this research effort, we have since updated the time-series measurements of all three variables (δ^{13}C-DIC, DIC, and ALK) beyond the previously published record length which ended in 2002 (Brix et al., 2004; Gruber et al., 2002; Keeling et al., 2004). The time-series records now extend through 2016 to 2017 at all three stations, roughly doubling the length of the isotopic record.

1.4 OVERVIEW OF THIS DISSERTATION

Chapter 2 describes the calibration, uncertainty analysis, and methodology used by the Scripps CO_2 program for measuring stable carbon isotopes in seawater samples with a dual-inlet Optima isotope ratio mass spectrometer (IRMS). This chapter expands on previous isotope calibration reports (Bollenbacher et al., 2000; Guenther et al., 2001) to include the time period from 2001 to 2018. Three new seawater secondary standards are presented and characterized, one of which involves a new and unique method based on a high-pressure mixture of pure CO_2 and high purity nitrogen gas in a 50L aluminum tank. The new seawater secondary standards behave reliably on the Optima IRMS and the calibration contribution to uncertainty over the full time-period of seawater measurements for δ^{13}C is ±0.025‰.

Chapter 3 presents the updated $^{13}C/^{12}C$, DIC, ALK seawater time-series measurements, which now extend to 2017, an additional 14 to 15 years beyond the previously published records

(Brix et al., 2004; Gruber et al., 2002; Keeling et al., 2004). The long-term trends for δ^{13}C-DIC are essentially the same, and essentially linear over the length of the records, at the time-series locations in both the North Pacific and North Atlantic. The seasonal amplitudes of δ^{13}C-DIC, sDIC, pCO_2 vary interannually, but do not appear to have a significant trend of increasing or decreasing amplitudes. The NAO is strongly correlated with interannual variability in the majority of reported time-series variables observed at Station S and BATS. The PDO is correlated with the sDIC, SST, pCO_2, and MLD interannual variability observed at HOT, in support of earlier publications (Brix et al., 2004). We also show correlation between NINO3.4 and sDIC and MLD at HOT, which was not evident in the shorter records previously. This chapter discusses the observed long-term trends, seasonal cycles, and interannual variability in the context of additional oceanographic variables as well as relevant atmospheric variables and dominant modes of climate variability and how they relate to earlier published records.

Chapter 4 explores upper ocean carbon variability in subtropical gyres using a combination of observations and hindcast simulations from the Community Earth System Model (CESM) that includes stable carbon isotopes in the ocean biogeochemistry. The observations are used to verify the model at the time-series sites (HOT and BATS) and then basin-scale relationships are explored within the model, with a focus on interannual variability and spatial patterns of variability within the subtropical gyres. There are spatially coherent patterns of variability in the North Atlantic and North Pacific subtropical gyres, which can in part be explained by dominant modes of climate variability in these regions. The interannual variability at the BATS time-series station is largely explained by vertical mixing structure and broadly representative of the variability throughout the majority of the North Atlantic subtropical gyre. In contrast, the location for the HOT time-series station may represent only a subsection of the

variability throughout the North Pacific subtropical gyre which has more complex patterns and controls of variability.

1.5 REFERENCES

Bacastow, R.B., Keeling, C.D., Lueker, T.J., Wahlen, M., 1996. The 13C Suess effect in the world surface oceans and its implication for oceanic uptake of CO2: Analysis of observations at Bermuda. Global Biogeochemical Cycles 10, 335–346.

Bates, N., Astor, Y., Church, M., Currie, K., Dore, J., Gonaález-Dávila, M., Lorenzoni, L., Muller-Karger, F., Olafsson, J., Santa-Casiano, M., 2014. A Time-Series View of Changing Ocean Chemistry Due to Ocean Uptake of Anthropogenic CO2 and Ocean Acidification. Oceanography 27, 126–141. https://doi.org/10.5670/oceanog.2014.16

Bates, N.R., 2007. Interannual variability of the oceanic CO2 sink in the subtropical gyre of the North Atlantic Ocean over the last 2 decades. Journal of Geophysical Research 112. https://doi.org/10.1029/2006JC003759.

Bollenbacher, A.F., Guenther, P.R., Keeling, C.D., Stewart, E.F., Wahlen, M., Whorf, T.P., 2000. Calibration Methodology for the Scripps 13C/12C and 18O/16O Stable Isotope Program.

Brix, H., Gruber, N., Keeling, C.D., 2004. Interannual variability of the upper ocean carbon cycle at station ALOHA near Hawaii. Global Biogeochemical Cycles 18. https://doi.org/10.1029/2004GB002245.

Caldeira, K., Wickett, M.E., 2003. Anthropogenic carbon and ocean pH. Nature 425, 365–365. https://doi.org/10.1038/425365a.

Gruber, N., Keeling, C.D., Bacastow, R.B., Guenther, P.R., Lueker, T.J., Wahlen, M., Meijer, H.A.J., Mook, W.G., Stocker, T.F., 1999. Spatiotemporal patterns of carbon-13 in the global surface oceans and the oceanic Suess Effect. Global Biogeochemical Cycles 13, 307–335. https://doi.org/10.1029/1999GB900019.

Gruber, N., Keeling, C.D., Bates, N.R., 2002. Interannual Variability in the North Atlantic Ocean Carbon Sink. Science 298.

Gruber, N., Keeling, C.D., Stocker, T.F., 1998. Carbon-13 constraints on the seasonal inorganic carbon budget at the BATS site in the northwestern Sargasso Sea. Deep-Sea Research I 45, 673–717.

Guenther, P.R., Bollenbacher, A.F., Keeling, C.D., Stewart, E.F., Wahlen, M., 2001. Calibration methodology for the Scripps 13C/12C and 18O/16O stable isotope program, 1996-2000. A Report Prepared for the Global Environmental Monitoring Program of the World Meteorological Organization.

Heimann, M., Maier-Reimer, E., 1996. On the relations between the oceanic uptake of CO2 and its carbon isotopes. Global Biogeochemical Cycles 10, 89–110.

Jasper, J.P., Hayes, J.M., 1990. A carbon isotope record of C02 levels during the late Quaternary 347, 462–464.

Karl, D.M., 2002. Nutrient dynamics in the deep blue sea. Trends in Microbiology 10, 410–418. https://doi.org/10.1016/S0966-842X(02)02430-7.

Karl, D.M., 1999. A Sea of Change: Biogeochemical Variability in the North Pacific Subtropical Gyre 34.

Keeling, C.D., Brix, H., Gruber, N., 2004. Seasonal and long-term dynamics of the upper ocean carbon cycle at Station ALOHA near Hawaii. Global Biogeochemical Cycles 18. https://doi.org/10.1029/2004GB002227.

Körtzinger, A., Quay, P.D., Sonnerup, R.E., 2003. Relationship between anthropogenic CO2 and the 13C Suess effect in the North Atlantic Ocean. Global Biogeochemical Cycles 17, 5-1-5–20. https://doi.org/10.1029/2001GB001427.

McNeil, B.I., Matear, R.J., Tilbrook, B., 2001. Does carbon 13 track anthropogenic CO2 in the Southern Ocean?. Global Biogeochemical Cycles 15, 597–613.https://doi.org/10.1029/2000GB001352.

Quay, P., Sonnerup, R., Munro, D., Sweeney, C., 2017. Anthropogenic CO2 accumulation and uptake rates in the Pacific Ocean based on changes in the 13C/12C of dissolved inorganic carbon. Global Biogeochemical Cycles 2016GB005460.https://doi.org/10.1002/2016GB005460.

Quay, P., Sonnerup, R., Stutsman, J., Maurer, J., Körtzinger, A., Padin, X.A., Robinson, C., 2007. Anthropogenic CO2 accumulation rates in the North Atlantic Ocean from changes in the 13C/12C of dissolved inorganic carbon. Global Biogeochemical Cycles 21. https://doi.org/10.1029/2006GB002761.

Quay, P., Sonnerup, R., Westby, T., Stutsman, J., McNichol, A., 2003. Changes in the 13C/12C of dissolved inorganic carbon in the ocean as a tracer of anthropogenic CO2 uptake. Global Biogeochemical Cycles 17, 1004. https://doi.org/10.1029/2001GB001817.

Quay, P., Stutsman, J., 2003. Surface layer carbon budget for the subtropical N. Pacific: constraints at station ALOHA. Deep Sea Research Part I: Oceanographic Research Papers 50, 1045–1061. https://doi.org/10.1016/S0967-0637(03)00116-X.

Rau, G.H., 1989. Latitudinal variations in plankton d13C: Implications for CO2 and productivity in past oceans. Letters to Nature 341.

Sabine, C.L., Tanhua, T., 2010. Estimation of Anthropogenic CO2 Inventories in the Ocean. Annual Review of Marine Science 2, 175–198. https://doi.org/10.1146/annurev-marine-120308-080947.

Sonnerup, R.E., Quay, P.D., McNichol, A.P., Bullister, J.L., Westby, T.A., Anderson, H.L., 1999. Reconstructing the oceanic 13C Suess Effect. Global Biogeochemical Cycles 13, 857–872. https://doi.org/10.1029/1999GB900027.

Tanaka, T., Watanabe, Y.W., Watanabe, S., Noriki, S., Tsurushima, N., Nojiri, Y., 2003. Oceanic Suess effect of δ13C in subpolar region: The North Pacific. Geophysical Research Letters 30. https://doi.org/10.1029/2003GL018503.

Tans, P.P., Berry, J.A., Keeling, R.F., 1993. Oceanic 13C/12C observations: A new window on ocean CO2 uptake. Global Biogeochemical Cycles 7, 353–368. https://doi.org/10.1029/93GB00053.

Watanabe, Y.W., Chiba, T., Tanaka, T., 2011. Recent change in the oceanic uptake rate of anthropogenic carbon in the North Pacific subpolar region determined by using a carbon-13 time series. Journal of Geophysical Research 116. https://doi.org/10.1029/2010JC006199.

Zeebe, R.E., 2012. History of Seawater Carbonate Chemistry, Atmospheric CO2, and Ocean Acidification. Annual Review of Earth and Planetary Sciences 40, 141–165. https://doi.org/10.1146/annurev-earth-042711-105521.

1.6 FIGURES

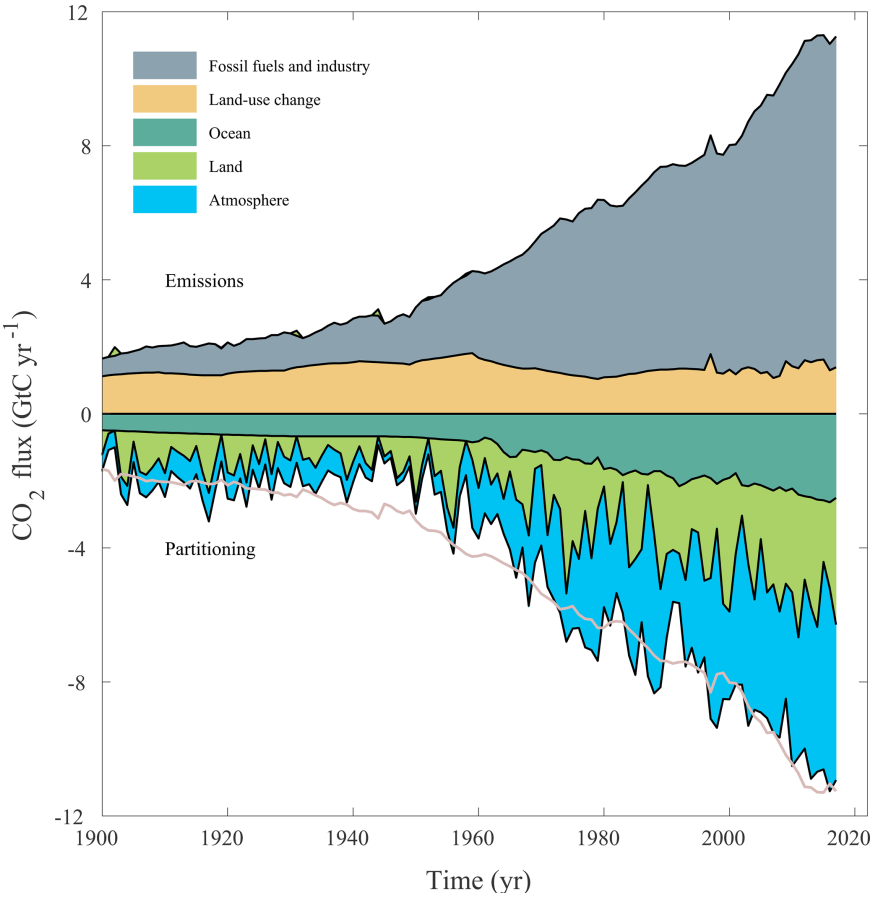

Figure 1.1: Global carbon budget from Le Queré et al. (2018) showing anthropogenic emissions sources and sinks since 1900.

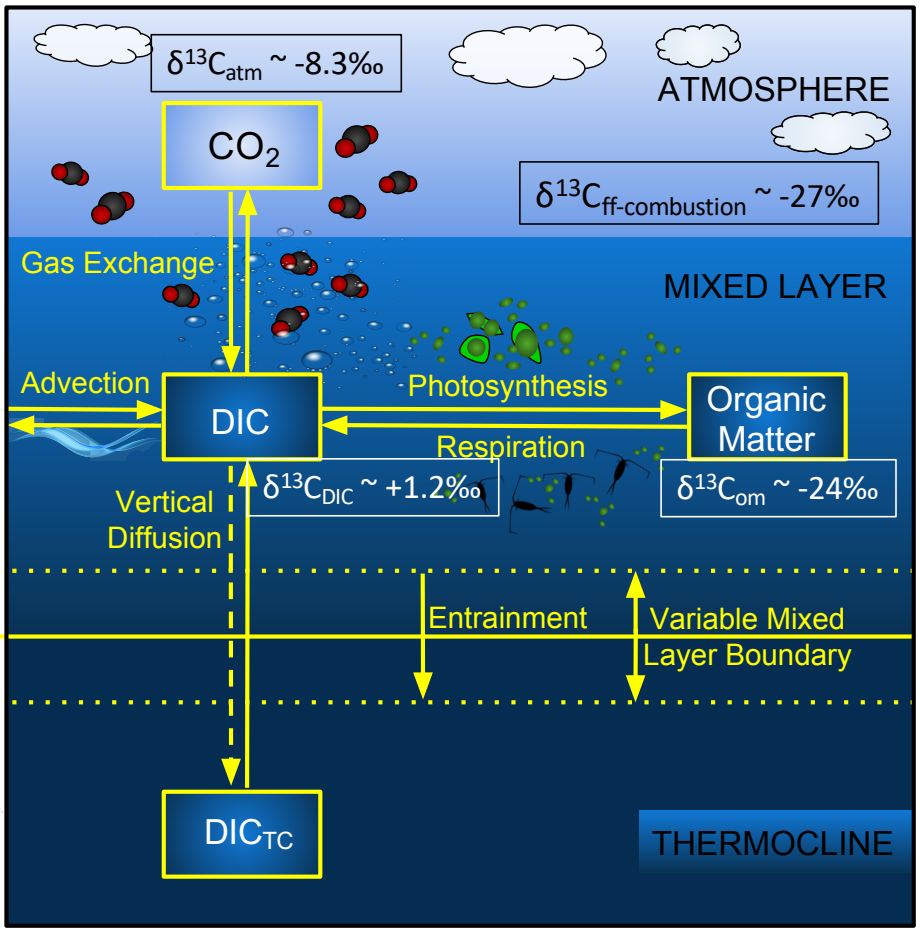

Figure 1.2: Schematic of the different processes which impact DIC and δ^{13}C-DIC in the surface ocean. Modified from Gruber et al. (1998). We note that calcification and dissolution are not represented here (see text).

CHAPTER 2: CALIBRATION METHODS FOR MEASUREMENTS OF $^{13}C/^{12}C$ IN DISSOLVED INORGANIC CARBON IN SEAWATER

ABSTRACT

The Scripps Seawater Program has measured stable isotope values of $^{13}C/^{12}C$ in seawater dissolved inorganic carbon (DIC) from seawater samples collected at roughly monthly intervals from three separate stations since the 1980s. We report on the calibration methods and uncertainty analysis for measurements of $^{13}C/^{12}C$ in DIC using a dual-inlet Optima isotope ratio mass spectrometer (IRMS) with secondary standards. We also present and characterize three new seawater secondary standards, including one based on a high-pressure mixture of pure CO_2 with high purity nitrogen gas in a 50L aluminum tank. We find that the new seawater secondary standards behave reliably on the Optima MS and show that the calibration contribution to uncertainty in the seawater $\delta^{13}C$ data is ±0.025‰.

2.1 INTRODUCTION

Stable isotope measurements of $^{13}C/^{12}C$ in seawater dissolved inorganic carbon (DIC) have been made by the Scripps Seawater Program on seawater samples collected at roughly monthly intervals from three separate stations since the 1980s. In coordination with the U.S. Joint Global Ocean Flux Study (JGOFS), this monitoring was initiated in 1983 in the North Atlantic at HydroStation S (32°10'N, 64°30'W), ~26 km southeast of the island of Bermuda. Two additional sample collection sites were added in 1988, the JGOFS Bermuda Atlantic Time-series Study (BATS) (31°50'N, 64°10'W), ~80 km southeast of Bermuda in the North Atlantic (Bates et al., 1996), and the Hawai'i Ocean Time-series (HOT) Station ALOHA (22°45'N, 158°00'W), ~100 km north of the island of 'Oahu, Hawai'i in the North Pacific (Karl and Lukas, 1996).

Several publications present prior results from these isotopic measurements through 2002 (Gruber et al., 1998, 2002; Brix et al., 2004; Keeling et al., 2004). Calibration methods for the isotopic measurements were presented previously in (Bollenbacher et al., 2000; Guenther et al., 2001). There was a hiatus in the seawater sample isotopic measurements from roughly 2004 to 2015. During this ~11-year period, samples were archived either in the originally collected sample bottles, or as pure CO_2 extracted from acidified seawater samples in glass "flame-off-tubes" (FOTs; see below). Before resuming isotopic measurements in 2015, it was necessary to develop new reference materials because the old secondary standards were partly depleted.

Prior to 1992, the isotope measurements were done in the laboratory of Prof. Willem Mook of the Centrum voor Isotopen Onderzeok (CIO) at the University of Groningen, in the Netherlands. Subsequently, measurement were made at Scripps in the laboratory of Prof. Martin Wahlen, using a VG Prism II isotope ratio mass spectrometer (IRMS). Beginning in August 2000, the measurements at Scripps transitioned to an Optima IRMS, first housed in the lab of Prof C.D. Keeling and subsequently housed in the lab of Prof. R.F. Keeling. The Scripps measurements using both the Prism and then the Optima IRMS have been calibrated based on linear calibration equations anchored to three NBS standard (NBS16, NBS17, and NBS19) (Bollenbacher et al., 2000). This initial 1994 calibration was retrospectively applied to the measurements made between 1992 and 1994. A Craig correction is also applied to account for the influence of ^{17}O on measured $\delta^{13}C$ values (Craig, 1957). The calibration of the VG Prism instrument is detailed in previous reports (Bollenbacher et al., 2000; Guenther et al., 2001). The calibration methods for the Optima have not been previously discussed.

This report covers methods and results associated with calibration of the Optima IRMS for measurements of $^{13}C/^{12}C$ in total dissolved CO_2 in seawater using secondary standards that

are essentially pure CO_2 gas with negligible N_2O, reflective of the absence of N_2O in seawater samples (Bollenbacher et al., 2000). This report also discusses the transition between the Prism and Optima IRMS instruments and discusses the development of secondary gas standards for calibrating seawater $^{13}C/^{12}C$, including one based on a high-pressure mixture of CO_2 in N_2. A separate report will discuss the calibration of the Optima IRMS for measurements of $^{13}C/^{12}C$ and $^{18}O/^{16}O$ in air, which depends on additional secondary standards containing a mixture of CO_2 and N_2O in atmospheric proportions (Lueker et al., 2020).

2.2 MATERIALS AND METHODS

2.2.1 Preparation of Secondary Standards

Specific preparation and storage techniques for each secondary standard are discussed in more detail below and are summarized in Table 2.1 and 2.2. The seawater secondary standards consist of two sets, where Set 1 refers to four standards that were obtained or prepared in the 1990s (GS19, GS20, GEA4, and GES1). Set 2 includes three secondary standards (GES2, 2342, and DCS1) that were prepared in 2015/2016. All the secondary standards except GS19 and GS20 were prepared from sodium bicarbonate or calcium carbonate materials by acidifying ground carbonates in a vacuum extraction system and subsequently cryogenically isolating the CO_2 gas into an evacuated flask. GS19 and GS20 consist of pure CO_2 gas purchased from CIO (Bollenbacher et al., 2000).

Set 1:

2.2.1.1 GS19 & GS20, used as standards from June/July 1992 through 2004:

The preparation and usage of these secondary standards have been discussed in two previous reports (Bollenbacher et al., 2000; Guenther et al., 2001). They consist of pure CO_2 in 0.5 L stainless steel flasks with bronze double Nupro-valves. The valves are connected in series

with 1/4" O.D. stainless steel tubing allowing for ~2 cm^3 volume between the valves. They were obtained from Dr. Mook of CIO in 1992, with original fill pressure of ~202 kPa. They were in regular use as secondary standards from June/July 1992 through 2004. From 2004 through 2010, they continued to be analyzed but they were no longer used as secondary standards for seawater measurements. By July 2010, their pressures had dropped through usage to ~20 kPa. A reanalysis of these secondaries on October 13, 2016 and December 9, 2016 against other secondaries suggested that $\delta^{13}C$ for both GS19 and GS20 had drifted upwards by ~0.04‰ during the intervening six years.

2.2.1.2 GEA4, used as standard from October 1995 to present:

The preparation and use of this secondary standard has been discussed in two previous reports (Bollenbacher et al., 2000; Guenther et al., 2001). Briefly, GEA4 was prepared by Guy Emanuele on October 26, 1995 by acidifying approximately 20 grams of $NaHCO_3$ with 40% H_3PO_4 under vacuum and capturing the evolved CO_2 after removing the evolved H_2O via a series of traps. GEA4 was stored as pure CO_2 in a 5L glass round-bottom flask and 1517 1-2 cm^3 aliquots of this flask were transferred by Guy Emanuele into glass FOTs between October 1995 and December 1996. Both the flask and 520 break-seal glass tubes of GEA4 still exist as of 2018.

2.2.1.3 GES1, used as standard from December 1997 to October 2016:

The preparation and use of this secondary standard has been discussed previously (Guenther et al., 2001). GES1 was prepared on November 24, 1997 by Guy Emanuele from 22 grams of $CaCO_3$ Dover chalk using the same acidification method as GEA4 and the resulting pure CO_2 was also stored in a 5 L glass round-bottom flask. About 99 aliquots were transferred

to FOTs between November 1997 and June 1998. The remainder of CO_2 was left in the glass flask and stored in the seawater lab until August 2015.

Set 2:

2.2.1.4 GES2, used as standard from August 2015 to present:

The preparation and use of the standard has not previously been discussed. It consists of CO_2 in FOTs filled from the GES1 flask and is given different designation because of a long hiatus in the usage of the GES1 flask. GES2 exists only as discrete samples in FOTs, which were filled from the GES1 flask between August 11, 2015 and August 28, 2015. This was more than ten years since the previous use of the GES1 flask. We compared GES2 FOTs with the earlier transfers from GES1 and found a statistically non-zero offset in $\delta^{13}C$. On August 28, 2015, the GES1 flask broke and the CO_2 was lost. At that time ~43 of the total 50 GES2 FOTs remained to be used as a secondary standard.

2.2.1.5 2342, used as standard from April 2016 to present:

The preparation and usage of this standard has not been previously discussed. It consists of CO_2 in N_2 in a high-pressure cylinder. 2342 was prepared by Mariela Brooks and Timothy Lueker on April 6, 2016 by acidifying approximately 11 grams of $CaCO_3$ from a ground up Palmyra atoll coral sample, using essentially the same method as for GEA4. The pure CO_2 was transferred to a 0.42 L stainless-steel flask with a final pressure of 38 psi, and this flask was used to prepare three FOTs. On May 5, 2016, the CO_2 remaining in the stainless-steel flask was transferred to a ~50 L aluminum tank (Tank 2342) and topped up to 920 psi with high purity N_2 gas, which yielded a CO_2 concentration of ~350 ppm. Since then, 2342 has been extracted roughly monthly on the automated extraction rack (AERII, discussed further below). As of

August 2017, a total of 117 aliquots had been transferred to FOTs from 2343, with ~700 psi remaining in the tank.

2.2.1.6 DCS1, used as standard from April 2016 to present:

The preparation and usage of this standard has not been previously discussed. DCS1 was prepared on April 22, 2016 by Mariela Brooks and Timothy Lueker from 21 grams of Dover chalk using essentially the same acidification method as GEA4. The resulting pure CO_2 was stored in the repaired and annealed 5 L glass round-bottom flask (previously used for GES1) using stopcocks with Viton O-rings. As of November 2, 2016, 189 aliquots had been transferred to FOTs using on the seawater lab manual extraction line (discussed further below), with the remainder of the gas remaining in the 5 L glass flask for future use.

2.2.2 Transfer of Standard Material to Break-Seal Glass Tubes

The "break seal" glass tubes used for both for seawater and air secondary standards consist of 1/4" outer diameter borosilicate-glass that are typically ~5 to 10 cm long with the ends either flame-sealed or fused with an electronic fuser after the CO_2 has been frozen (using liquid nitrogen) into the tube under vacuum. The break-seal glass tubes for Set 1 have been previously described (Bollenbacher et al., 2000; Guenther et al., 2001). We prepared the break-seal glass tubes for Set 2 either on the seawater lab manual vacuum transfer line or the automatic extraction rack (AERII).

2.2.2.1 Manual Transfer Rack

A schematic of the manual vacuum transfer rack is shown in Figure 2.1 (top). We used this to fill break-seal glass tubes from Set 2 flasks containing pure CO_2 (GES2, DCS1). We attach the flask as indicated on the left side of the transfer line which we pump out up to the lower valve on the flask (FV1). We then close the upper valve on the flask (FV2) and close the

vacuum pump valve (PV6). We place liquid nitrogen on the break-seal glass tube that the aliquot of CO_2 will be frozen into and ensure that only the valve (of F1-F6) leading to that particular break-seal glass tube is open. With FV2 closed, we open FV1 to expand and equilibrate the standard gas into the ~2cc volume between FV1 and FV2. We then close FV1, isolating the CO_2 aliquot and subsequently open FV2 to allow the aliquot of CO_2 to pass through a cryo-trap of ethanol and dry ice to remove water vapor and freeze the CO_2 into the break-seal glass tube in liquid nitrogen. We allow ~4.5 minutes for the transfer to complete, assessed by observing that the pressure gauge on the transfer line (G3) has dropped back down to the evacuated pressure (signifying that the gas has been transferred fully) and waiting an additional 30 seconds. At this point, we raise the liquid nitrogen on the break-seal glass tube, and an electric fuser is used for 2-3min to seal the aliquot of the standard gas into the glass break-seal glass tube.

2.2.2.2 Automatic Transfer Rack

A schematic of the automatic extraction rack, AERII, is shown in Figure 2.1 (bottom). In the context of seawater isotope calibration, we use this rack for transfer from tank 2342 to break-seal glass tubes. AERII follows the general procedure of cryo-traps described above but valve switching, the liquid nitrogen traps, and fusing are automated and used for secondary standards that are stored in tanks (including air secondaries). We attach 2342 to the inlet at v1 as indicated in Figure 2.1 (bottom). When transferring 2342 aliquots into break-seal glass tubes v2 to v12 on the upper and lower manifolds remain shut. The gas flows down and then left-to-right through the various traps before entering the break-seal glass tube it is being isolated into, which is controlled by the valves F1-F6.

2.2.3 Data Reduction Methods

2.2.3.1 OPTIMA software calculations: The OPTIMA software requires the user to input the declared $\delta^{13}C$ and $\delta^{18}O$ values of the instrument reference gas used on the reference inlet. The instrument software converts the reference values to 'standard format' so that the instrument can compare the 45/44 and 46/44 ion current ratios of the measured sample and reference values as detailed in the Optima User Manual. To do this, the Optima software uses the following formulation which essentially is the reverse Craig correction:

$$\delta(45/44)_{REF} = (\delta^{13}C_{REF} + 0.0338 * \delta^{18}O_{REF})/1.0676 \quad (2.1)$$

$$\delta(46/44)_{REF} = (\delta^{18}O_{REF} + 0.0021 * \delta^{13}C_{REF})/1.0010 \quad (2.2)$$

where $\delta^{13}C_{REF}$ = -3.964‰ and $\delta^{18}O_{REF}$ = -15.696‰.

After a sample is measured, the Optima software then computes:

$$\delta(45/44)_{SA} = \delta(45/44)_{SA\ wrt\ REF} + \delta(45/44)_{REF} + (\delta(45/44)_{SA\ wrt\ REF} * \delta(45/44)_{REF})/1000 \quad (2.3)$$

$$\delta(46/44)_{SA} = \delta(46/44)_{SA\ wrt\ REF} + \delta(46/44)_{REF} + (\delta(46/44)_{SA\ wrt\ REF} * \delta(46/44)_{REF})/1000 \quad (2.4)$$

where $\delta(45/44)_{SA\ wrt\ REF}$ and $\delta(46/44)_{SA\ wrt\ REF}$ are delta values measured with respect to the instrument reference gas. The dual inlet system allows for the instrument to switch between the reference and sample gases 12 times and determines an average measured value based on these 6 comparisons.

The Optima software then applies the Craig correction:

$$\delta^{13}C_{MS} = ((1.0676 * \delta(45/44)_{SA}) - (0.0338338 * \delta(46/44)_{SA}))/0.99992902 \quad (2.5)$$

$$\delta^{18}O_{MS} = ((1.0010 * \delta(46/44)_{SA}) - (0.00224196 * \delta(45/44)_{SA})/0.99992902 \quad (2.6)$$

where $\delta^{13}C_{MS}$ and $\delta^{18}O_{MS}$ are the main output of the OPTIMA software, made available in print form to the user along with each of the 12 reference-sample measurements mentioned above, corresponding trace plots, precision for the delta value obtained, and details of instrument settings used for that particular run.

2.2.3.2 Subsequent calculations: Using the instrument output for $\delta^{13}C_{MS}$ and $\delta^{18}O_{MS}$ values, we apply a 4-step procedure to compute final processed δ values:

Step 1: Undo the instrument-generated Craig correction to yield δ values based on original ion currents (Bollenbacher et al., 2000, equation (2.1)).

$$\delta(45/44) = (\delta^{13}C_{MS} + 0.0338 * \delta^{18}O_{MS})/1.0676 \quad (2.7)$$

$$\delta(46/44) = (\delta^{18}O_{MS} + 0.0021 * \delta^{13}C_{MS})/1.0010 \quad (2.8)$$

where $\delta^{18}O_{MS}$ and $\delta^{13}C_{MS}$ are the delta values reported by the instrument software.

Step 2: Apply the 1994 NBS correction (Bollenbacher et al., 2000) for analysis dates before October 1, 1996 and the 1997 NBS correction (Guenther et al., 2001) for analysis dates on or after October 1, 1996. The change in NBS correction has no bearing on the final numbers because it is corrected for through the use of daily terms (Step 4 below).

$$\delta(45/44)' = 0.995034 * \delta(45/44) + 0.05901 \quad (< 1 \text{ Oct. } 1996) \quad (2.9)$$

$$= 0.994228 * \delta(45/44) + 0.017353 \quad (\geq 1 \text{ Oct. } 1996)$$

$$\delta(46/44)' = 1.00758 * \delta(46/44) + 0.21137 \quad (< 1 \text{ Oct. } 1996) \quad (2.10)$$

$$= 1.00487 * \delta(46/44) + 0.007153 \quad (\geq 1 \text{ Oct. } 1996)$$

Step 3: Reapply the ion (Craig) correction (Bollenbacher et al., 2000, Eqn (2.3)).

$$\delta^{13}C_{nbscorr} = ((1.0676 * \delta(45/44)') - (0.0338338 * \delta(46/44)'))/0.99992902 \quad (2.11)$$

$$\delta^{18}O_{nbscorr} = ((1.0010 * \delta(46/44)') - (0.00224196 * \delta(45/44)')/0.99992902 \quad (2.12)$$

Step 4: Results from runs of the secondary standards are used to apply day-to-day corrections to the sample measurements. The secondary standards are analyzed identically to samples through Step 3. These results are then used to compute

$$^{13}D_i = (\delta^{13}C_{assigned,\,i} - \delta^{13}C_{nbscorr,\,i}) \quad (2.13)$$

$$^{18}D_i = (\delta^{18}O_{assigned,\,i} - \delta^{18}O_{nbscorr,\,i}) \quad (2.14)$$

where $\delta^{13}C_{assigned,\,i}$ is the assigned value of standard *i* (described below), and $\delta^{13}C_{nbscorr,\,i}$ is the $\delta^{13}C_{nbscorr}$ value computed from Step 3 for standard *i*. Typically, more than one standard is analyzed on the same day, (i.e. at the beginning and at the end of sample runs). A "daily term" is then calculated as an average of the difference terms $^{13}D_i$ and $^{18}D_i$ for any seawater secondary standards run on a given day.

$$^{13}D_{sw} = mean(^{13}D_i) \quad (2.15)$$

$$^{18}D_{sw} = mean(^{18}D_i) \quad (2.16)$$

The samples run on that date are then corrected according to

$$\delta^{13}C_{termcorr} = \delta^{13}C_{nbscorr} + {}^{13}D_{sw} \quad (2.17)$$

$$\delta^{18}O_{termcorr} = \delta^{18}O_{nbscorr} + {}^{18}D_{sw} \quad (2.18)$$

This correction is similarly but separately done for the atmospheric samples using the atmospheric air secondary standards instead of the seawater secondary standards due to the influence of N_2O in air which could result in differences in day-to-day drift.

Final isotope values: For the seawater measurements, no further corrections are applied, and the final δ values are given by:

$$\delta^{13}C = \delta^{13}C_{termcorr} \quad (2.19)$$

$$\delta^{18}O = \delta^{18}O_{termcorr} \quad (2.20)$$

We note that for air samples which contain N_2O, the calculation of final δ values involves two additional corrections that are not used with seawater samples. The first is the standard N_2O correction, based on measured N_2O of a sample. The second correction allows for an offset between the CIO and SIO labs. This CIO or "Mook" correction is assumed to be zero for seawater samples based on results reported in (Bollenbacher et al., 2000) where it was shown that N_2O-free samples compared between CIO and SIO might have a small offset on the order of ~0.02‰, but there was insufficient data and the results of the comparison were not conclusive enough to warrant the use of an offset correction for the seawater measurements.

2.3 RESULTS

2.3.1 Assignments of Secondary Standards

The original assignment of GS19, GS20, GES1 and GEA4 was described in two previous reports (Bollenbacher et al., 2000; Guenther et al., 2001). GS19 was assigned $\delta^{13}C$ and $\delta^{18}O$ values based on a comparison with a three-point calibration using NBS16, NBS17, and NBS19 in Jan 1994. GS20 and GES1 were assigned based on their average offset from GS19, and GEA4 was assigned based on the average offset from both GS19 and GS20, for a given set of measurements made on the same day. The assignment for GS20 was made based on 29 days of measurements, the assignment for GEA4 was made based on 17 days of measurements, and the assignment for GES1 was made based on 13 days of measurements. These four secondary standards span a range of -8.6 to +1.9‰ for $\delta^{13}C$ and -1.8 to +1.8‰ for $\delta^{18}O$.

As the archive studies described below suggest no drift in GES1 and GEA4 over time, we consequently freeze their assignments to be constant over time at the original assigned values (see Table 2.2 for assigned values). This report therefore entails no scale revision, i.e. no change

to data reported in previous publications (Gruber et al., 1998, 2002; Brix et al., 2004; Keeling et al., 2004).

In order to make assignments on GES2, 2342, and DCS1, we ran aliquots from flame-off tubes as unknowns against GEA4 and/or GES1 on the Optima IRMS. We then averaged he measured values for $\delta^{13}C_{termcorr}$ and $\delta^{18}O_{termcorr}$ for each standard (GES2, 2342, or DCS1) and all values outside of 2-sigma from the mean were discarded. We based the assigned value for each secondary standard on the mean of the remaining values. GES2 was assigned using a total of 43 runs, 2342 was assigned using a total of 65 runs, and DCS1 was assigned using a total of 106 runs. Figure 2.2 shows the data used to make these assignments as detailed in Table 2.2. These three standards span a range of -0.8 to +2.0‰ in $\delta^{13}C$, which compares to a range of ~+1 to +2‰ for surface seawater. They span a range of -3.6 to -1.6‰ in $\delta^{18}O$ which compares to typical value of ~+0.9‰ for $\delta^{18}O$ in the seawater sample CO_2 extracts.

2.3.2 Stability of Secondary Standards

To help diagnose the stability of the secondary standards, we have periodically carried out "archive studies", in which break-seal glass tubes of the given secondary that were archived (i.e. transferred to break-seal glass tubes) on different dates are all analyzed on the same date. Under the seemingly reasonable assumption that the CO_2 isotopes are stable in the break-seal glass tubes, these archive studies then provide a measure of the stability of the secondary standard in its original source container (i.e. the container used prior to transfer to the break-seal glass tube). By completing these analyzes on a single date, this stability check is independent of the long-term calibration of the mass spectrometer.

The archive studies' results are plotted in Figure 2.4, with the drift and corresponding uncertainties summarized in Table 2.3, and with the basic data tabulated in Tables 2.4.1-2.4.5.

For each analysis date, $\delta^{13}C$ measurements on a given standard had a standard deviation between ±0.008 and ±0.016‰, except for GES2 which had a standard deviation of ±0.039‰. For GES1 and GES2 the transfer dates did not span a sufficient time interval to assess drift. For GEA4, 2342, and DCS1 a drift rate was calculated using a linear least-squares fit that allowed for an arbitrary additive constant for each analysis date but a single slope versus transfer date. None of the slopes were statistically different from zero, and thus no drift corrections were applied to the seawater secondary standards.

2.3.4 Daily Terms

Figures 2.3.1 and 2.3.2 show the daily terms assessed based on analyses of the seawater secondary standards plotted against the analysis date. Also shown are daily terms for CO_2 in air standards, which contain N_2O and are not directly relevant to seawater measurements. The standard deviation of the daily terms is typically consistent to within ±0.05‰ and ±0.27‰ for $\delta^{13}C$ and $\delta^{18}O$ respectively. Periods of systematic drift are also evident, as well as seemingly abrupt shifts typically associated with documented changes in the instrument configuration. The drift in the daily term accounts for changes in the raw observed differences between the standards and the instrument reference gas. These shifts could have any of many causes and are not understood in detail. The daily terms do not show any striking shift during the transition from the Prism to the Optima in August 2000, which also entailed using a new instrument reference gas. Our use of a daily term effectively relates seawater samples directly to the secondary standards, which we have tracked carefully over time, thus canceling the impact of these shifts in the daily terms on any measured seawater trends.

2.3.5 Scale Contraction Stability

An important diagnostic of mass spectrometer performance is the stability of the difference between two standards with large differences in $\delta^{13}C$. This is relevant to the extent that our seawater measurements sometimes have relied on standards that are not isotopically close in $\delta^{13}C$ to seawater (such as GEA4). Any expansion or contraction of these differences over time would indicate an additional source of uncertainty in the measurements.

To address this issue, we examine the history of the differences between GEA4 and GES1. This pair has been run over the longest period of time (1992-2016) of any of the secondary standards and also spans a large range in $\delta^{13}C$ from -7.5‰ to +1.9‰. Figure 2.5 shows the differences in $\delta^{13}C_{termcorr}$ for GEA4 and GES1 for each date that we ran both GEA4 and GES1 plotted versus analysis date. A linear regression indicates no significant trend ($p = 0.109$) over the 24-year measurement period with a standard deviation of ±0.019‰ corresponding to a ±0.2% of the difference in $\delta^{13}C$ between GEA4 and GES1. The results suggest that variations in scale contraction or expansion have impacted the seawater measurements to, at most, the ±0.019‰ level and that the span calibration for both the Optima and Prism was stable to ±0.2% of the span range.

2.3.6 Calibration Contribution to Measurement Uncertainty

We are principally interested here in the ability to detect trends (secular, seasonal, etc.) in $\delta^{13}C$ in seawater over time. An important metric is the expected uncertainty of the observations. To assess this, we model the total variance of the seawater measurements according to

$$\sigma_{tot}^2 = \sigma_1^2 + \sigma_2^2 + \sigma_3^2 \tag{2.21}$$

where σ_1 includes machine imprecision and other within-day variations, σ_2 includes day-to-day calibration offsets, and σ_3 includes errors from sampling, storage, and extraction

We first looked at the pooled standard deviation of multiple break-seal glass tubes from the same standard that were run on same day:

$$sd_{pooled} = [((n_1\text{-}1)\cdot sd_1^2 + (n_2\text{-}1)\cdot sd_2^2 + \ldots + (n_i\text{-}1)\cdot sd_i^2) \div (n_1 + n_2 + \ldots + n_i - k)]^{-1/2} \quad (2.22)$$

Here sd_i is the standard deviation of the break-seal glass tube runs of this standard on day i, n_i is the number of runs, and k is the total number of analysis dates with two more break-seal glass tube runs of this standard. GEA4 by far had the most replicates run on the same day with a total of k = 161 days that had a range of 2 to 7 counts of GEA4 measurements. For GEA4, this yielded sd_{pooled} = ±0.011‰ for $\delta^{13}C$ and ±0.029‰ for $\delta^{18}O$. We repeated this with the remaining seawater Set 1 and Set 2 secondary standards with a range of k = 5 to 15 days. This yielded sd_{pooled} ranging between ±0.011‰ and ±0.029‰ for $\delta^{13}C$ and ranging between ±0.011‰ and ±0.061‰ for $\delta^{18}O$. These values are summarized in Table 2.5. We view this as a measure of σ_1.

We also investigated a measure of uncertainty that accounts for day-to-day variations based on the early performance of the Set 2 secondaries while they were being groomed but not yet used as secondaries. For each of these we compute the standard deviation of the $\delta^{13}C_{termcorr}$ and $\delta^{18}O_{termcorr}$ values over grooming period, as summarize in Table 2.5. This yielded standard deviations for GES2, DCS1, and 2342 ranging from ±0.021‰ to ±0.030‰ for $\delta^{13}C$ and ±0.064‰ to ±0.093‰ for $\delta^{18}O$. We view this as a measure of the combined errors from $\sigma_1 + \sigma_2$. The comparison with the errors above for σ_1 suggests that the contribution from σ_2 is as small as ±0.001‰ and no greater than ±0.019‰ for $\delta^{13}C$ and between ±0.003‰ and ±0.082‰ for $\delta^{18}O$. This suggests that the daily term correction scheme works relatively well does not introduce excessive additional uncertainty.

We also estimated a measure of overall external uncertainty based on replicate seawater samples that were run on different days, where the replicates typically came from different

depths (e.g. 1m and 10m or 5m and 25m). With the combined total of 767 replicate seawater samples collected on k = 382 separate samples dates that were analyzed from all three of our sample stations in the North Pacific and North Atlantic subtropical gyres (BATS, Station S, and HOT) over the past 30 years, the pooled standard deviation computed via Eqn (2.22) was ±0.025‰ for $\delta^{13}C$. We take these as a measure of σ_{tot}, which when combined with the above estimates suggest that the combined sampling, storage, and extractions errors (σ_3) are between zero and ±0.014‰ for $\delta^{13}C$. This analysis demonstrates that a significant fraction of the overall uncertainty comes from machine imprecision and other same-day uncertainties with an additional possibly significant contribution from day-to-day calibration uncertainties, with a smaller contribution from sample handling and extractions.

2.3.7 Extended Seawater Isotope Time-series

We have updated the seawater $\delta^{13}C$ isotope time-series measurements through 2016 and 2017 for all three stations using the secondary standards described here. These updated records now include an additional ~15 years of data relative to the previously published record and are shown in Figure 2.6. The new time-series data from 10m sample measurements shown in green highlight the continuity between the isotope record before and after the measurement hiatus. In addition, the purple filled circles show where the 1m (Station S and BATS) and 25m (HOT) overlapping duplicate samples agree well with the previous measurements. The gap evident at Station S and BATS between 2005 and 2006 is due to the failure of a sample storage refrigerator at SIO. This figure includes the dissolved inorganic carbon (DIC) and alkalinity (ALK) time-series records as well, all of which are discussed in further detail in Chapter 3.

2.4 DISCUSSION AND SUMMARY

This chapter has detailed the methods used to ensure continuity in the calibration of seawater $\delta^{13}C$ measurements at Scripps. This work applies to measurements made over years 2015-2018. Prior to 2015, seawater $\delta^{13}C$ measurements were calibrated using pure CO_2 standards. With this work, we introduced two additional pure CO_2 seawater secondary standards as well as a third standard based on pure CO_2 blended with ultra-high-purity (UHP) N_2 and stored in a high-pressure cylinder.

This chapter also details a new method for assessing drift in CO_2 isotopic secondary standards through the use of so-called "archive studies". An archive study involves analyzing multiple break-seal glass tubes derived from different extraction dates, which allows us to estimate drift in the secondary standards that is independent from day-to-day variations in instrument performance. Using this method, we are also able to conduct stability checks on the same secondary standard flask or cylinder. Under the seemingly reasonable assumption that the CO_2 isotopes are stable in the break-seal glass tubes, these archive studies provide a measure of the stability of a secondary standard in its original source flask or cylinder.

Through the use of these archive studies we were able to show that the seawater secondary standards have been stable and have shown no need for a drift correction to be applied. This is in contrast to the experience with air standards (containing N_2O) some of which required drift correction as detailed in (Lueker et al., 2020). The archive studies demonstrated stability of both the pure CO_2 secondary standards as well as the CO_2 in N_2 standard in tank 2342, which was assessed with four archive studies. Going forward, the use of CO_2 in N_2 may prove advantageous, because the method provides a larger reservoir material thus extending

lifetime and allows for a more streamlined preparation process which parallels the air standard preparation.

We have also quantified the methodological uncertainties in the seawater $\delta^{13}C$ measurements, combining contributions from calibration, sample handling and analysis. No single step in the measurement process stood out as the dominant source of uncertainty. We find that the calibration contribution to uncertainty in the seawater $\delta^{13}C$ data is ±0.025‰. The overall external precision, i.e. the repeatability of seawater samples measured different dates and different standards, is between 0.011 to 0.030‰. This precision is an order of magnitude smaller than seasonal amplitudes and two order of magnitude smaller than measured secular changes in $\delta^{13}C$ over the 30-year time frame of the time-series.

Finally, we were able to demonstrate continuity between measurements with the transition from making measurements on a Prism MS (before August 2000) to an Optima MS (after August 2000) as evidenced by the lack of significant offset between the secondary standards that overlap this transition period in August 2000. As a component of this analysis, we analyzed archived samples from bottles that were collected on the same day as samples that had been previously run before the hiatus and should therefore be nominally identical. We found that measurements of $\delta^{13}C$ made before and after the seawater isotope measurement hiatus with these overlapping sample dates do not show significant offsets. In sum, these achievements give us confidence for reasonable continuity in the extended seawater stable isotope records, which are discussed in more detail in Chapter 3.

2.5 ACKNOWLEDGEMENTS

We would like to acknowledge Andrew Dickson, Guy Emanuele, and the Dickson Lab for all of the work they have contributed to maintaining this time-series record. In addition, we

would like to thank the Bermuda Institute for Ocean Science (BIOS) and Hawaii Ocean Time-series (HOT) station personnel without whom these samples could not have been collected and this dataset would not be possible. This work has been supported by funding from the Schmidt Foundation and NSF.

Chapter 2 in part is currently being prepared for submission for publication of the material. Brooks, Mariela K; Lueker, Timothy J; Bollenbacher, Alane F; Walker, Stephen J; Dickson, Andrew G; Emanuele III, Guy; Keeling, Ralph F. The dissertation author was the primary investigator and author of this material.

2.6 REFERENCES

Bates, N.R., Michaels, A.F., Knap, A.H., 1996. Seasonal and interannual variability of oceanic carbon dioxide species at the US JGOFS Bermuda Atlantic Time-series Study (BATS) site. Deep Sea Research Part II: Topical Studies in Oceanography 43, 347–383.

Bollenbacher, A.F., Guenther, P.R., Keeling, C.D., Stewart, E.F., Wahlen, M., Whorf, T.P., 2000. Calibration Methodology for the Scripps $^{13}C/^{12}C$ and $^{18}O/^{16}O$ Stable Isotope Program.

Brix, H., Gruber, N., Keeling, C.D., 2004. Interannual variability of the upper ocean carbon cycle at station ALOHA near Hawaii. Global Biogeochemical Cycles 18. https://doi.org/10.1029/2004GB002245.

Craig, H., 1957. Isotopic standards for carbon and oxygen and correction factors for the mass-spectrometric analysis of carbon dioxide. Geochimica et Cosmochimica Acta 12, 133–149.

Gruber, N., Keeling, C.D., Bates, N.R., 2002. Interannual Variability in the North Atlantic Ocean Carbon Sink. Science 298.

Gruber, N., Keeling, C.D., Stocker, T.F., 1998. Carbon-13 constraints on the seasonal inorganic carbon budget at the BATS site in the northwestern Sargasso Sea. Deep-Sea Research I 45, 673–717.

Guenther, P.R., Bollenbacher, A.F., Keeling, C.D., Stewart, E.F., Wahlen, M., 2001. Calibration methodology for the Scripps 13C/12C and 18O/16O stable isotope program, 1996-2000. A Report Prepared for the Global Environmental Monitoring Program of the World Meteorological Organization.

Karl, D.M., Lukas, R., 1996. The Hawaii Ocean Time-series (HOT) program: Background, rationale and field implementation. Deep Sea Research Part II: Topical Studies in Oceanography 43, 129–156.

Keeling, C.D., Brix, H., Gruber, N., 2004. Seasonal and long-term dynamics of the upper ocean carbon cycle at Station ALOHA near Hawaii. Global Biogeochemical Cycles 18. https://doi.org/10.1029/2004GB002227.

Lueker, T.J., Keeling, R.F., Bollenbacher, A.F., Walker, S., Morgan, E., Brooks, M., 2020. Calibration methodology for the Scripps $^{13}C/^{12}C$ and $^{18}O/^{16}O$ stable isotope program 1992-2018. UC San Diego: Scripps Institution of Oceanography.

Table 2.1: summary of storage and preparation of seawater isotope secondary standards

Standard	Storage	Contents	Prepped by	Extractions
GS19	Small metal flask/can	CO_2 (source unknown)	CIO – Dr. Mook Lab	*
GS20	Small metal flask/can	CO_2 (source unknown)	CIO – Dr. Mook Lab	*
GEA4	5 L glass flask & FOTs	CO_2 from $NaHCO_3$	G. Emanuele	Manual
GES1	5 L glass flask & FOTs	Pure CO_2 from Dover Chalk	G. Emanuele	Manual
GES2	5 L glass flask & FOTs	Pure CO_2 from Dover Chalk	**	Manual
2342	50 L Aluminum Tank & FOTs	CO_2 from Palmyra Coral with pure N_2	M. Brooks & Dr. T. Lueker	Automatic
DCS1	5 L glass flask & FOTs	Pure CO_2 from Dover Chalk	M. Brooks & Dr. T. Lueker	Manual

*GS19 and GS20 have only been run when directly connected to the Optima inlet system, as opposed to having aliquots extracted and preserved in flame-off-tubes for subsequent analysis.
**GES2 content was GES1 gas that was stored and determined to have drifted sufficiently in the interim to require a new value assignment.

Table 2.2: Summary of seawater isotope secondary standards.

Standard	Assigned $\delta^{13}C$	SD	Assigned $\delta^{18}O$	SD	Archive Study
GS19	-7.464	±0.010	-0.125	±0.018	*
GS20	-8.573	±0.009	-0.915	±0.023	*
GEA4	-7.499	±0.008	+1.756	±0.025	Jul 8, 2002
GES1	+1.944	±0.012	-1.759	±0.036	Dec 1, 1997
GES2	+1.982	±0.024	-1.598	±0.044	Nov 10, 2015
2342	-0.845	±0.015	-3.621	±0.047	Dec 9, 2016
DCS1	+1.900	±0.015	-2.571	±0.054	Oct 13, 2016

*Archive studies were not performed on GS19 and GS20 because these have only been run when directly connected to the Optima inlet system, as opposed to having aliquots extracted and preserved in flame-off-tubes for subsequent analysis.

Table 2.3: Summary of drift rates and associated standard deviation (SD) values in ‰ yr^{-1}.

Standard	$\delta^{13}C$ Drift (‰ yr^{-1})	SD	$\delta^{18}O$ Drift (‰ yr^{-1})	SD	Archive Study
GEA4	+0.0081	±0.0064	-0.0091	±0.0115	Jul 8, 2002
GES1*	-	-	-	-	Dec 1, 1997
GES2*	-	-	-	-	Nov 10, 2015
2342**	+0.0012	±0.0044	-0.0016	±0.0118	Dec 9, 2016
DCS1	-0.0059	±0.0155	+0.0681	±0.0970	Oct 13, 2016

*Span of transfer dates do not encompass sufficient time for long-term drift to be calculated (or be of concern).

** Based on mean drift rate determined by four separate archive studies.

Table 2.4.1: Archive study for GEA4. The number of samples used relates to how many extractions were available at the time of analysis. 'Prep Date' refers to the date the standard itself was prepared/cooked up, 'Transfer Date' refers to the day that the aliquot was transferred into its respective break-seal glass tube. All $\delta^{13}C$ and $\delta^{18}O$ values are reported using units of ‰.

Standard	Transfer ID	Prep Date	Transfer Date	Analysis Date	$\delta^{13}C$	$\delta^{18}O$
GEA4	017	26 Oct 1995	27 Oct 1995	08 Jul 2002	-7.497	+1.717
GEA4	163	26 Oct 1995	15 Dec 1995	08 Jul 2002	-7.500	+1.741
GEA4	289	26 Oct 1995	27 Mar 1996	08 Jul 2002	-7.489	+1.725
GEA4	478	26 Oct 1995	29 Apr 1996	08 Jul 2002	-7.505	+1.727
GEA4	637	26 Oct 1995	26 Jun 1996	08 Jul 2002	-7.504	+1.737
GEA4	726	26 Oct 1995	16 Jul 1996	08 Jul 2002	-7.492	+1.734
GEA4	838	26 Oct 1995	26 Jul 1996	08 Jul 2002	-7.497	+1.706
GEA4	933	26 Oct 1995	06 Aug 1996	08 Jul 2002	-7.501	+1.718
GEA4	1087	26 Oct 1995	16 Sep 1996	08 Jul 2002	-7.478	+1.744
GEA4	1261	26 Oct 1995	27 Sep 1996	08 Jul 2002	-7.496	+1.710
GEA4	1420	26 Oct 1995	08 Nov 1996	08 Jul 2002	-7.489	+1.709
GEA4	1500	26 Oct 1995	09 Dec 1996	08 Jul 2002	-7.492	+1.723
Archive Study Average					-7.495	+1.724
Archive Study Standard Deviation					±0.008	±0.013
GEA4 Assigned Value					-7.499	+1.756

GES1, GS19, GS20 run same day as standards

Table 2.4.2: Archive study for GES1. The number of samples used relates to how many extractions were available at the time of analysis. 'Prep Date' refers to the date the standard itself was prepared/cooked up, 'Transfer Date' refers to the day that the aliquot was transferred into its respective break-seal glass tube. All $\delta^{13}C$ and $\delta^{18}O$ values are reported using units of ‰.

Standard	Transfer ID	Prep Date	Transfer Date	Analysis Date	$\delta^{13}C$	$\delta^{18}O$
GES1	001	24 Nov 1997	24 Nov 1997	01 Dec 1997	+1.927	-1.770
GES1	002	24 Nov 1997	24 Nov 1997	01 Dec 1997	+1.946	-1.792
GES1	003	24 Nov 1997	25 Nov 1997	01 Dec 1997	+1.966	-1.709
GES1	004	24 Nov 1997	25 Nov 1997	01 Dec 1997	+1.930	-1.758
GES1	005	24 Nov 1997	25 Nov 1997	01 Dec 1997	+1.935	-1.753
GES1	006	24 Nov 1997	25 Nov 1997	01 Dec 1997	+1.955	-1.742
Archive Study Average					+1.943	-1.754
Archive Study Standard Deviation					±0.015	±0.028
GES1 Assigned Value					+1.944	-1.759

GEA4 run same day as standard

Table 2.4.3: Archive study for GES2. The number of samples used relates to how many extractions were available at the time of analysis. 'Prep Date' refers to the date the standard itself was prepared/cooked up, 'Transfer Date' refers to the day that the aliquot was transferred into its respective break-seal glass tube. All $\delta^{13}C$ and $\delta^{18}O$ values are reported using units of ‰.

Standard	Transfer ID	Prep Date	Transfer Date	Analysis Date	$\delta^{13}C$	$\delta^{18}O$
GES2	105	24 Nov 1997	11 Aug 2015	10 Nov 2015	+1.947	-1.697
GES2	108	24 Nov 1997	11 Aug 2015	10 Nov 2015	+2.040	-1.661
GES2	117	24 Nov 1997	24 Aug 2015	10 Nov 2015	+2.001	-1.683
GES2	128	24 Nov 1997	24 Aug 2015	10 Nov 2015	+1.993	-1.692
GES2	132	24 Nov 1997	27 Aug 2015	10 Nov 2015	+2.005	-1.685
GES2	138	24 Nov 1997	27 Aug 2015	10 Nov 2015	+1.977	-1.666
GES2	142	24 Nov 1997	28 Aug 2015	10 Nov 2015	+1.921	-1.631
Archive Study Average					+1.983	-1.673
Archive Study Standard Deviation					±0.039	±0.023
GES2 Assigned Value					+1.944	-1.759

GEA4 and GES1 run same day as standards

Table 2.4.4.1: Archive study for 2342 (1 of 4). The number of samples used relates to how many extractions were available at the time of analysis. 'Prep Date' refers to the date the standard itself was prepared/cooked up, 'Transfer Date' refers to the day that the aliquot was transferred into its respective break-seal glass tube. All $\delta^{13}C$ and $\delta^{18}O$ values are reported using units of ‰.

Standard	Transfer ID	Prep Date	Transfer Date	Analysis Date	$\delta^{13}C$	$\delta^{18}O$
2342	B16-1202	06 Apr 2016	10 Nov 2016	9 Dec 2016	-0.825	-3.603
2342	B16-1091	06 Apr 2016	18 Oct 2016	9 Dec 2016	-0.836	-3.565
2342	B16-906	06 Apr 2016	22 Aug 2016	9 Dec 2016	-0.832	-3.570
2342	B16-590	06 Apr 2016	17 Jun 2016	9 Dec 2016	-0.840	-3.591
2342	B16-436	06 Apr 2016	09 May 2016	9 Dec 2016	-0.813	-3.511
2342	B16-492	06 Apr 2016	27 May 2016	9 Dec 2016	-0.835	-3.579
2342	B16-677	06 Apr 2016	06 Jul 2016	9 Dec 2016	-0.839	-3.595
2342	B16-981	06 Apr 2016	16 Sep 2016	9 Dec 2016	-0.837	-3.566
2342	B16-1123	06 Apr 2016	24 Oct 2016	9 Dec 2016	-0.856	-3.631
2342	B16-1206	06 Apr 2016	10 Nov 2016	9 Dec 2016	-0.831	-3.597
Archive Study Average					-0.834	-3.581
Archive Study Standard Deviation					±0.011	±0.032
2342 Assigned Value					-0.845	-3.621

GEA4, GES2, DCS1 run same day as standards

Table 2.4.4.2: Archive study for 2342 (2 of 4). The number of samples used relates to how many extractions were available at the time of analysis. 'Prep Date' refers to the date the standard itself was prepared/cooked up, 'Transfer Date' refers to the day that the aliquot was transferred into its respective break-seal glass tube. All $\delta^{13}C$ and $\delta^{18}O$ values are reported using units of ‰.

Standard	Transfer ID	Prep Date	Transfer Date	Analysis Date	$\delta^{13}C$	$\delta^{18}O$
2342	B16-1201	06 Apr 2016	10 Nov 2016	13 Jan 2017	-0.825	-3.671
2342	B16-1119	06 Apr 2016	24 Oct 2016	13 Jan 2017	-0.834	-3.640
2342	B16-982	06 Apr 2016	16 Sep 2016	13 Jan 2017	-0.827	-3.641
2342	B16-676	06 Apr 2016	06 Jul 2016	13 Jan 2017	-0.860	-3.709
Archive Study Average					-0.837	-3.665
Archive Study Standard Deviation					±0.016	±0.032
2342 Assigned Value					-0.845	-3.621

GEA4 run same day as standard

Table 2.4.4.3: Archive study for 2342 (3 of 4). The number of samples used relates to how many extractions were available at the time of analysis. 'Prep Date' refers to the date the standard itself was prepared/cooked up, 'Transfer Date' refers to the day that the aliquot was transferred into its respective break-seal glass tube. All $\delta^{13}C$ and $\delta^{18}O$ values are reported using units of ‰.

Standard	Transfer ID	Prep Date	Transfer Date	Analysis Date	$\delta^{13}C$	$\delta^{18}O$
2342	B16-594	06 Apr 2016	20 Jun 2016	7 Dec 2017	-0.845	-3.718
2342	B17-666	06 Apr 2016	11 Aug 2017	7 Dec 2017	-0.824	-3.666
2342	B16-904	06 Apr 2016	22 Aug 2016	7 Dec 2017	-0.824	-3.679
2342	B17-438	06 Apr 2016	09 Jun 2017	7 Dec 2017	-0.845	-3.647
2342	B16-1088	06 Apr 2016	18 Oct 2016	7 Dec 2017	-0.829	-3.657
2342	B17-281	06 Apr 2016	03 Apr 2017	7 Dec 2017	-0.843	-3.691
2342	B17-168	06 Apr 2016	24 Feb 2017	7 Dec 2017	-0.830	-3.698
2342	B16-1205	06 Apr 2016	10 Nov 2016	7 Dec 2017	-0.832	-3.654
2342	B17-613	06 Apr 2016	02 Aug 2017	7 Dec 2017	-0.839	-3.675
Archive Study Average					-0.835	-3.676
Archive Study Standard Deviation					±0.008	±0.023
2342 Assigned Value					-0.845	-3.621

GEA4 run same day as standards

Table 2.4.4.4: Archive study for 2342 (4 of 4). The number of samples used relates to how many extractions were available at the time of analysis. 'Prep Date' refers to the date the standard itself was prepared/cooked up, 'Transfer Date' refers to the day that the aliquot was transferred into its respective break-seal glass tube. All $\delta^{13}C$ and $\delta^{18}O$ values are reported using units of ‰.

Standard	Transfer ID	Prep Date	Transfer Date	Analysis Date	$\delta^{13}C$	$\delta^{18}O$
2342	B17-167	06 Apr 2016	24 Feb 2017	10 May 2018	-0.826	-3.743
2342	B17-669	06 Apr 2016	11 Aug 2017	10 May 2018	-0.814	-3.741
2342	B16-593	06 Apr 2016	20 Jun 2016	10 May 2018	-0.838	-3.772
2342	B16-978	06 Apr 2016	16 Sep 2016	10 May 2018	-0.824	-3.715
2342	B18-466	06 Apr 2016	18 Apr 2018	10 May 2018	-0.829	-3.754
2342	B16-1200	06 Apr 2016	10 Nov 2016	10 May 2018	-0.835	-3.755
2342	B17-272	06 Apr 2016	03 Apr 2017	10 May 2018	-0.828	-3.759
2342	B16-915	06 Apr 2016	24 Aug 2016	10 May 2018	-0.834	-3.739
2342	B17-432	06 Apr 2016	09 Jun 2017	10 May 2018	-0.836	-3.744
2342	B16-1120	06 Apr 2016	24 Oct 2016	10 May 2018	-0.829	-3.743
Archive Study Average					-0.829	-3.747
Archive Study Standard Deviation					±0.007	±0.015
2342 Assigned Value					-0.845	-3.621

GEA4, DCS1 run same day as standards

Table 2.4.5: Archive study for DCS1. The number of samples used relates to how many extractions were available at the time of analysis. 'Prep Date' refers to the date the standard itself was prepared/cooked up, 'Transfer Date' refers to the day that the aliquot was transferred into its respective break-seal glass tube. All $\delta^{13}C$ and $\delta^{18}O$ values are reported using units of ‰.

Standard	Transfer ID	Prep Date	Transfer Date	Analysis Date	$\delta^{13}C$	$\delta^{18}O$
DCS1	088	22 Apr 2016	31 May 2016	13 Oct 2016	+1.896	-2.568
DCS1	109	22 Apr 2016	06 Jun 2016	13 Oct 2016	+1.912	-2.554
DCS1	157	22 Apr 2016	02 Sep 2016	13 Oct 2016	+1.906	-2.563
DCS1	007	22 Apr 2016	02 May 2016	13 Oct 2016	+1.905	-2.567
DCS1	039	22 Apr 2016	10 May 2016	13 Oct 2016	+1.909	-2.677
DCS1	058	22 Apr 2016	25 May 2016	13 Oct 2016	+1.892	-2.553
DCS1	091	22 Apr 2016	03 Jun 2016	13 Oct 2016	+1.904	-2.527
DCS1	145	22 Apr 2016	09 Aug 2016	13 Oct 2016	+1.896	-2.524
DCS1	178	22 Apr 2016	07 Sep 2016	13 Oct 2016	+1.905	-2.555
DCS1	021	22 Apr 2016	03 May 2016	13 Oct 2016	+1.905	-2.531
DCS1	052	22 Apr 2016	17 May 2016	13 Oct 2016	+1.912	-2.542
DCS1	075	22 Apr 2016	26 May 2016	13 Oct 2016	+1.903	-2.558
Archive Study Average					+1.904	-2.560
Archive Study Standard Deviation					±0.006	±0.040
DCS1 Assigned Value					+1.900	-2.571

GEA4, GES1, GES2 run same day as standards

Table 2.5: Calibration contribution to measurement uncertainty.

Pooled standard deviation for secondary standards run on the same day.			
Standard	k	$\delta^{13}C$ sd_{pooled}	$\delta^{18}O$ sd_{pooled}
GS19	15	±0.018 ‰	±0.024 ‰
GS20	10	±0.011 ‰	±0.011 ‰
GEA4	167	±0.011 ‰	±0.026 ‰
GES1	15	±0.014 ‰	±0.027 ‰
GES2	5	±0.029 ‰	±0.030 ‰
2342	5	±0.027 ‰	±0.056 ‰
DCS1	15	±0.020 ‰	±0.061 ‰
Standard deviation for Set 2 secondary standards run on different days as unknowns.			
Standard	Count	$\delta^{13}C$ sd	$\delta^{18}O$ sd
GES2	35	±0.030 ‰	±0.063 ‰
2342	82	±0.024 ‰	±0.093 ‰
DCS1	40	±0.021 ‰	±0.086 ‰
Seawater duplicate samples from different depths (1m and 10m or 5m and 25m).			
	Count	$\delta^{13}C$ sd	$\delta^{18}O$ sd
All three stations	382	±0.025 ‰	-

2.8 FIGURES

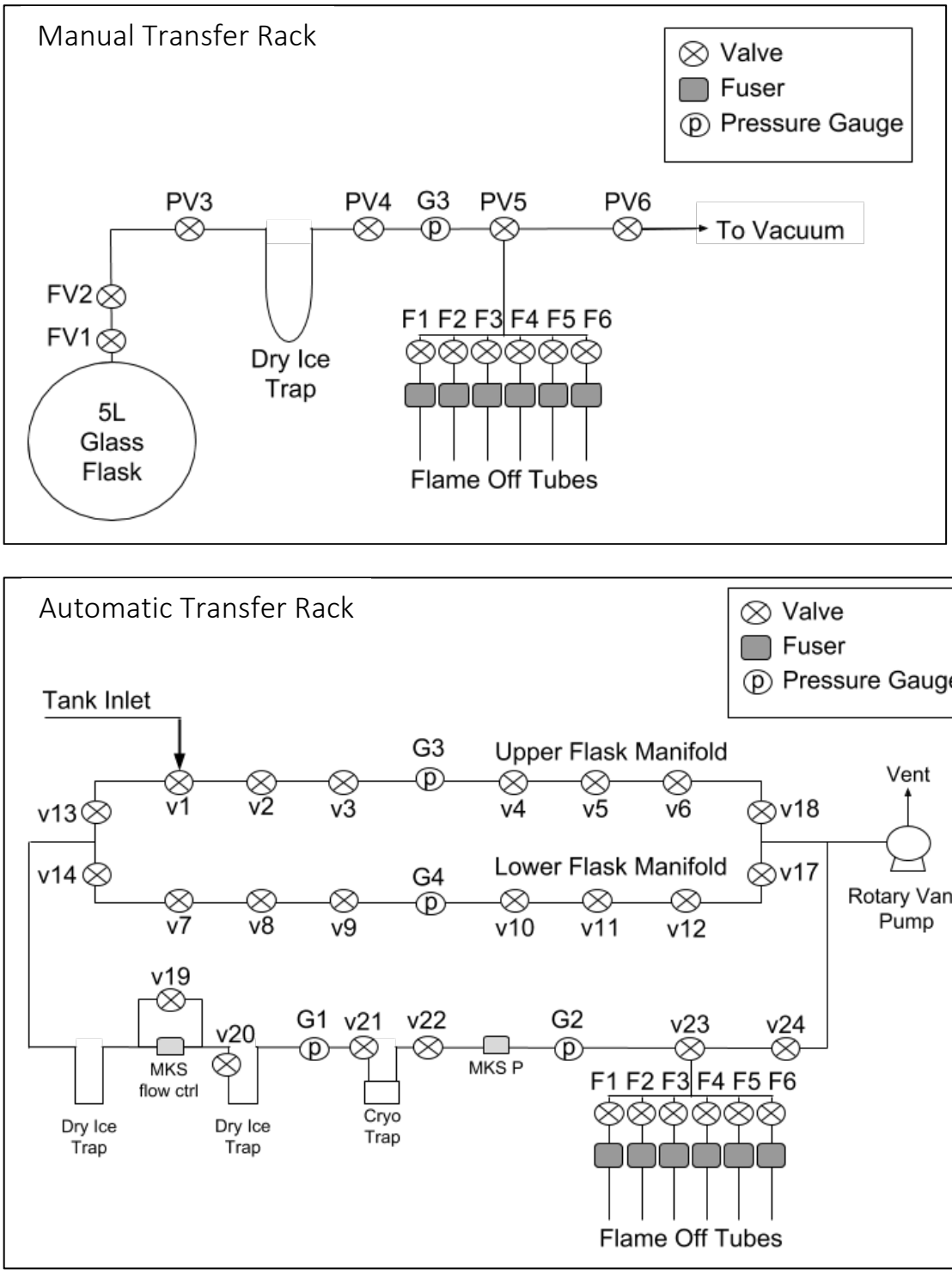

Figure 2.1 Schematic of the manual (top) and automatic (bottom) transfer racks.

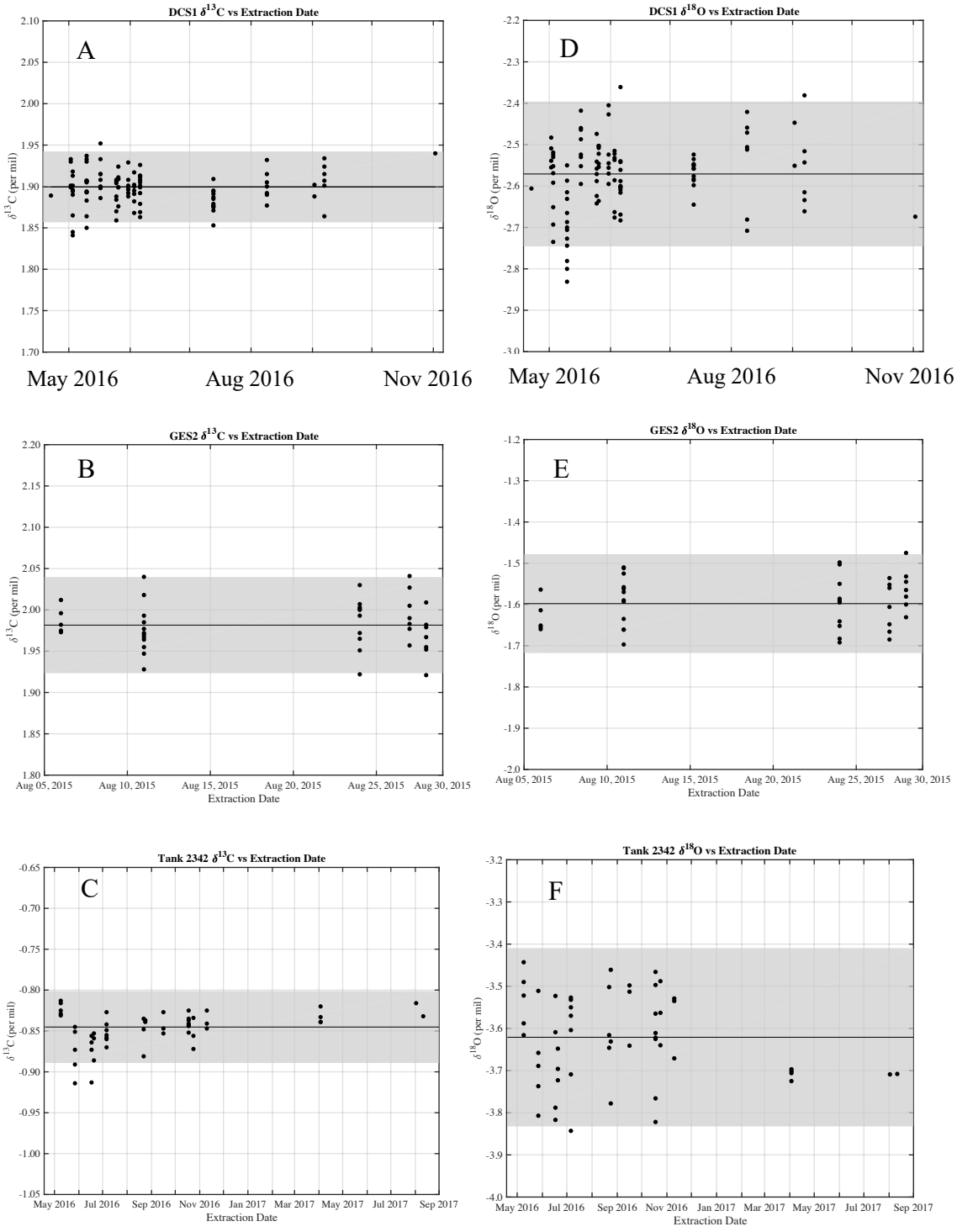

Figure 2.2: Assignment of secondary standard values. The black points represent the measured values for a given day. The shaded gray area encompasses the 2-sigma range of a given secondary standard. The solid black line shows the average values of the data contained within the shaded 2-sigma region. Figure 2-A, 2-B, and 2-C correspond to $\delta^{13}C$ for DCS1, GES2, and 2342, respectively and Figure 2-D, 2-E, and 2-F shows $\delta^{18}O$ for DCS1, GES2, and 2342 respectively.

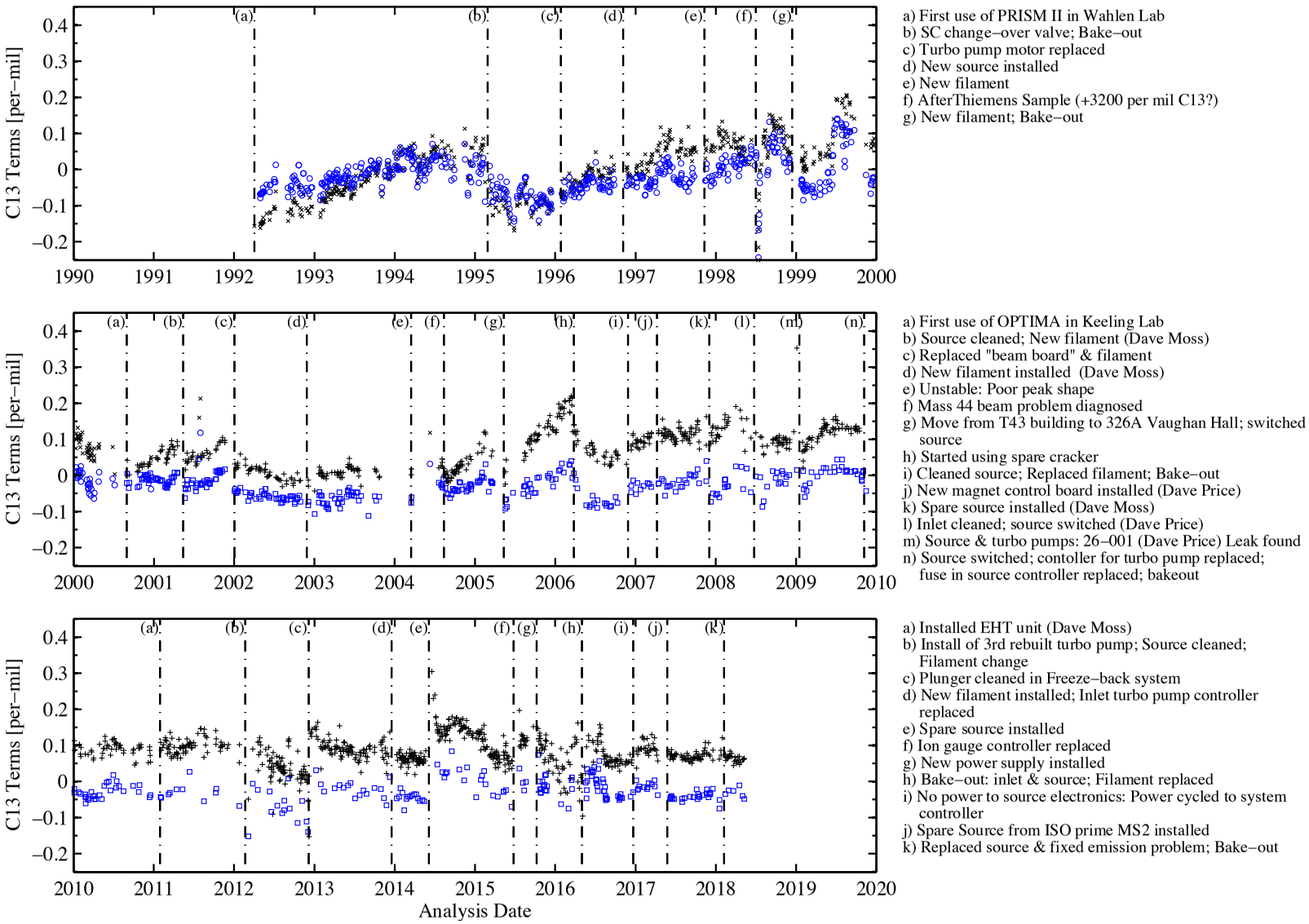

Figure 2.3.1: Daily terms for $\delta^{13}C$ based on seawater standards (blue) and air standards (black) plotted against the analysis date. Vertical dashed lines represent significant maintenance events (etc) that have occurred since 1992.

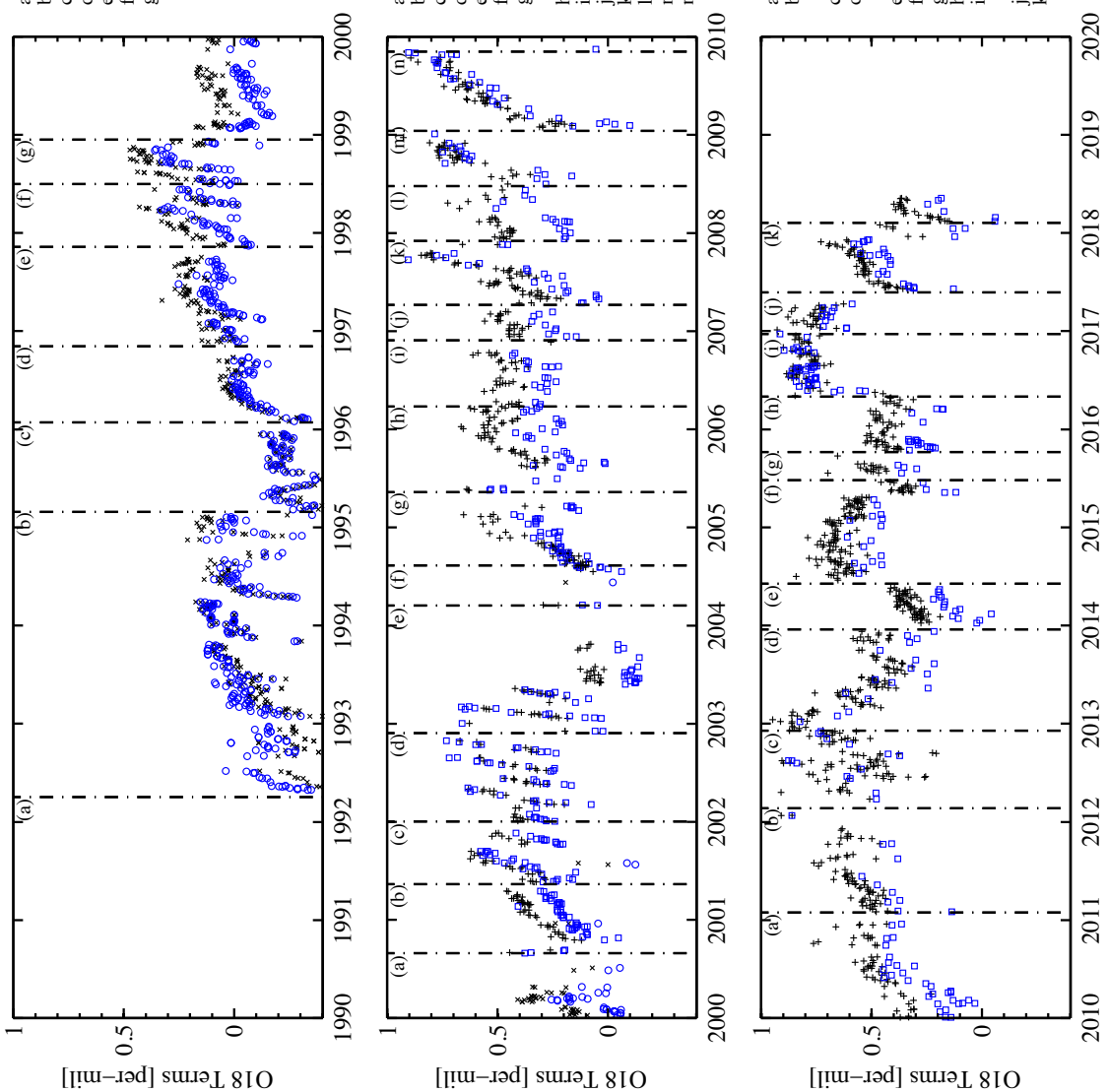

Figure 2.3.2: Daily terms for $\delta^{18}O$ for seawater standards (blue) and air standards (black) plotted against analysis date. Vertical dashed lines represent significant maintenance events (etc) that have occurred since 1992.

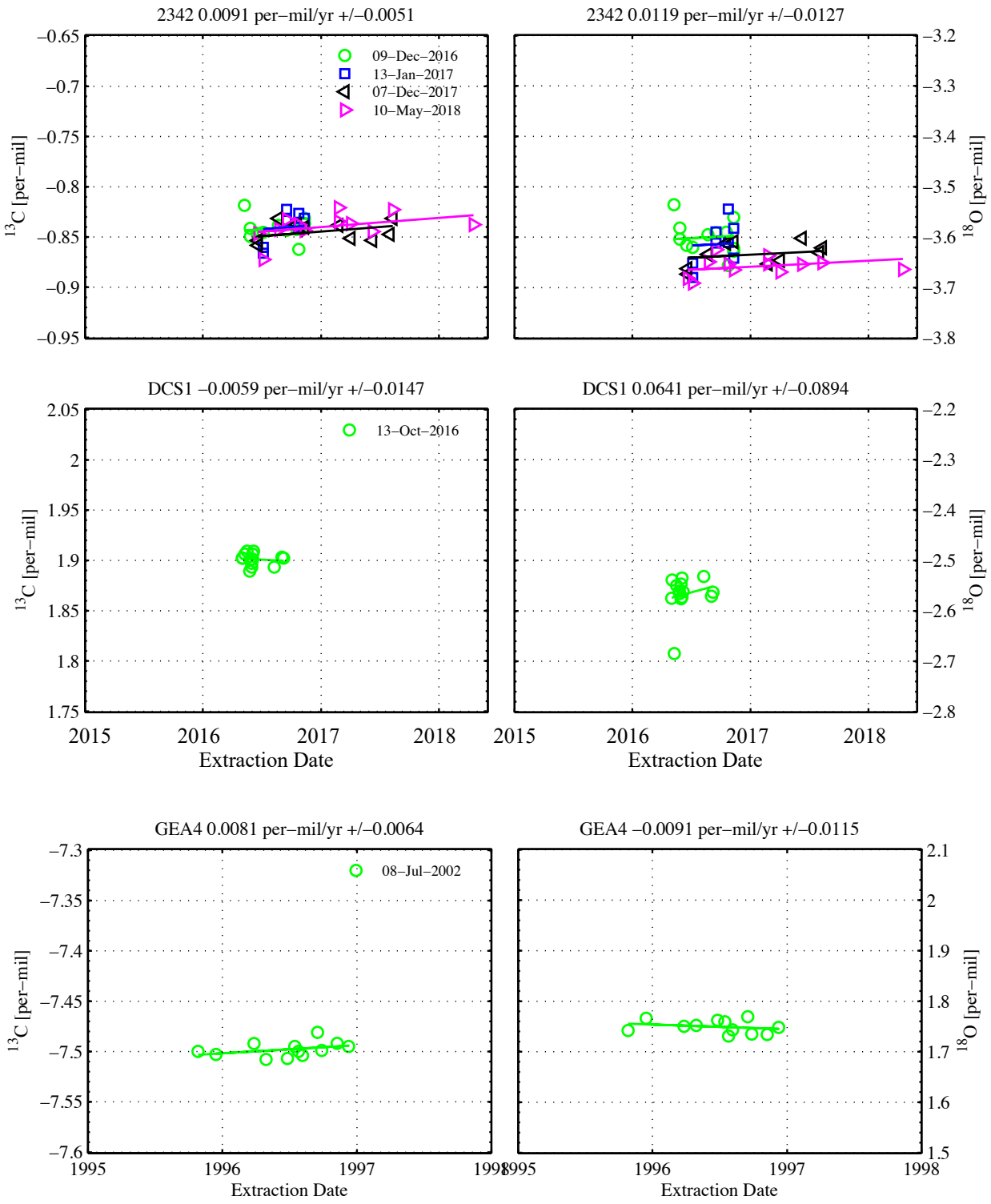

Figure 2.4: Archive studies for secondary seawater standards showing $\delta^{13}C_{termcorr}$ (left panels) and $\delta^{18}O_{termcorr}$ (right panels) plotted against transfer dates. The slope of the linear regression and standard error are reported in the title of each plot. Analysis dates are distinguished by symbol type/color (see legends). The slope is calculated using a linear least squares fit that includes a separate additive constant for each analysis date but a common slope vs transfer date.

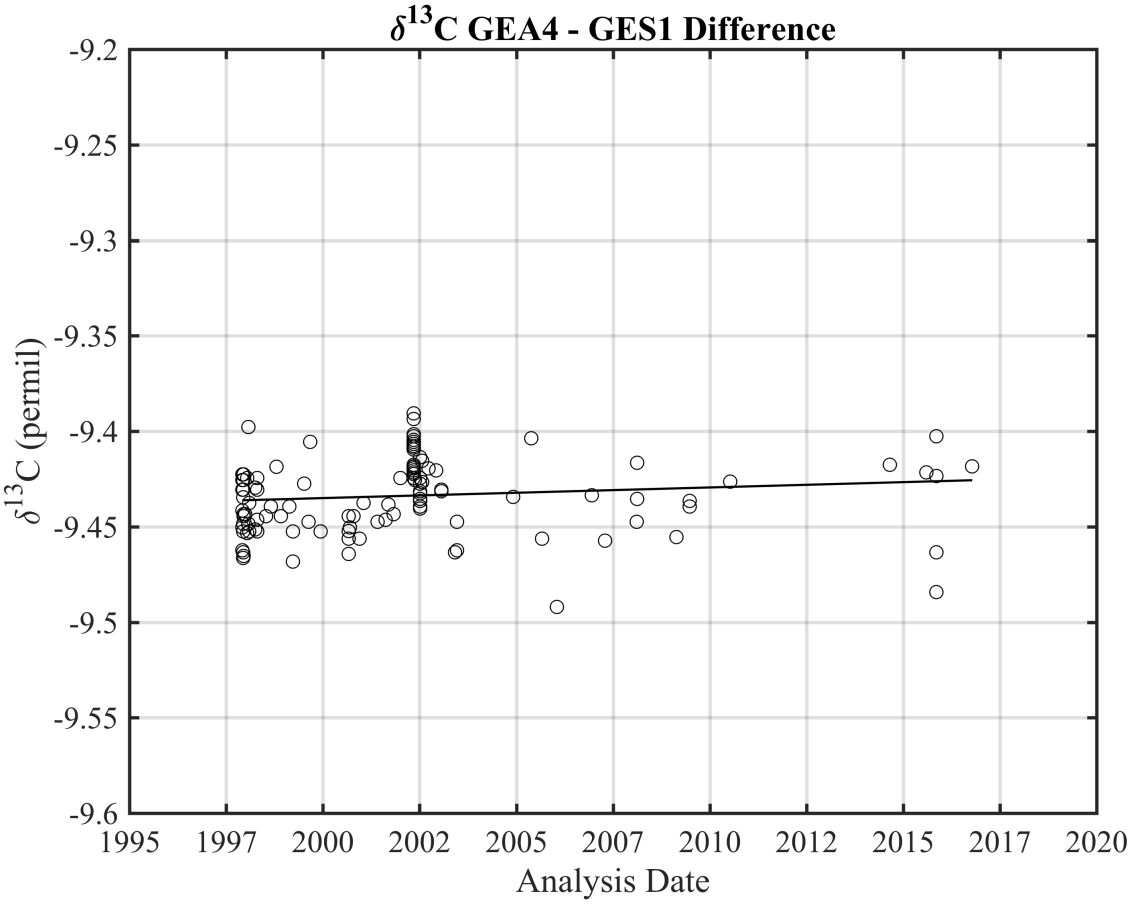

Figure 2.5: Scale contraction stability. The black open circles are the difference between the $\delta^{13}C_{termcorr}$ values of GEA4 and GES1 ($\delta^{13}C_{termcorr\ GEA4}$ - $\delta^{13}C_{termcorr\ GES1}$) plotted with the analysis date on the x-axis. This calculation was done for each individual value for GEA4 and GES1 on any day they both were run. The straight line is the linear regression ($p = 0.109$).

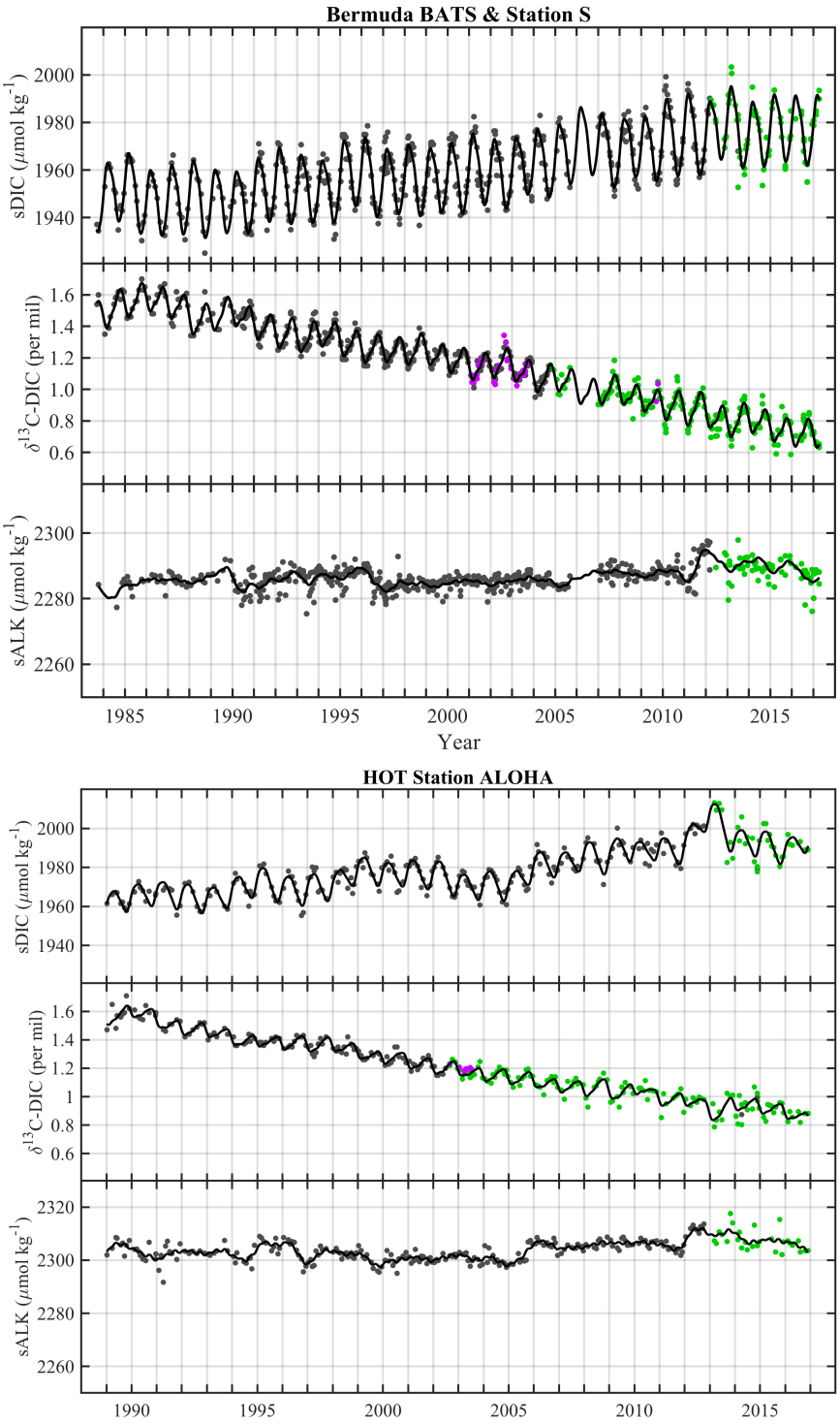

Figure 2.6: Seawater time-series data (gray filled circles) are shown with a quadratic fit in combination with 4-, 6-, and 12-month harmonics plus a cubic spline represented by the solid line. The green dots are the new measurements at 5m (HOT) and 10m (BATS and Stations S). New overlap samples from 1m (Bermuda) and 25m (HOT) are shown in purple. The gap evident at Station S and BATS between 2005 and 2006 is due to the failure of a sample storage refrigerator at SIO.

CHAPTER 3: CHANGES IN THE $^{13}C/^{12}C$ RATIO OF DISSOLVED INORGANIC CARBON NEAR BERMUDA AND HAWAII OVER THREE DECADES

ABSTRACT

The $^{13}C/^{12}C$ ratio of dissolved inorganic carbon ($\delta^{13}C$-DIC) in seawater is a powerful tool for quantifying various aspects of the marine carbon cycle, especially when combined with measurements of total DIC and alkalinity (ALK). We report on approximately three decades of stable isotope measurements of $\delta^{13}C$-DIC along with measured DIC and ALK as well as computed *p*CO2 from the subtropical North Pacific Hawaii Ocean Time-series (HOT) Station ALOHA and subtropical North Atlantic Bermuda Atlantic Time-series Study (BATS) and Station S (combined as S-BATS). The $\delta^{13}C$-DIC time-series records now include an additional ~15 years beyond the previously published record (Gruber et al., 2002; Brix et al., 2004; Keeling et al., 2004). We observe distinct long-term trends in $\delta^{13}C$-DIC, sDIC, and pCO2 in the HOT and S-BATS records in keeping with previously observed trends reported by Gruber et al. (2002) and Keeling et al. (2004). sDIC increased at a rate of +1.07 μmol kg^{-1} yr^{-1} from September 1983 to April 2017 at S-BATS and increased at a rate of +1.21 μmol kg^{-1} yr^{-1} from January 1989 to November 2016 at HOT. Over the same time periods $\delta^{13}C$-DIC decreased at essentially the same rate at each of the time-series station, -0.0264‰ yr^{-1} at S-BATS and -0.0259‰ yr^{-1} at HOT. We also show that the seasonal cycle amplitude of sDIC, $\delta^{13}C$-DIC, and computed pCO_2 exhibit interannual variability up to 40-50% of the mean amplitude, but we do not observe systematic change in onset or phase over the time-series record. At S-BATS, interannual variability in sDIC, SST, and mixed layer depth are significantly correlated with the NAO, consistent with previous findings. Also consistent with previous findings, HOT interannual variability in sDIC, pCO_2,

SST, and mixed layer depth are significantly correlated with the PDO. We also observe additional correlations which were not previously observed with the shorter record, including significant correlation between the PDO and SST and MLD at HOT as well as NINO3.4 and sDIC and mixed layer depth at HOT with correlation coefficients of similar magnitude as correlations with the PDO. Consistent with earlier publications, δ^{13}C-DIC interannual variability was not significantly correlated with any other variables or climate modes at S-BATS or HOT. The only exception to this, is significant correlation of δ^{13}C-DIC with both sDIC and SST at S-BATS.

3.1 INTRODUCTION

Time-series measurements of the variation of carbon composition in the atmosphere, oceans, and terrestrial biosphere are essential for understanding the links between climate and the global carbon cycle (Keeling et al., 1989; Tans et al., 1990; Keeling, 1993; Tans et al., 1993). Improved understanding of the ocean carbon cycle is particularly important for estimating the net flux of CO_2 into the oceans resulting from increasing atmospheric anthropogenic carbon (e.g. fossil fuels, cement production, and land-use changes), and to understand the potential for future changes in the natural cycles and forcing of air-sea exchange of CO_2 (Siegenthaler and Sarmiento, 1993; Sarmiento and Le Quéré, 1996; Quay and Stutsman, 2003; Sabine and Tanhua, 2010).

The $^{13}C/^{12}C$ ratio of dissolved inorganic carbon (δ^{13}C-DIC) in seawater is a powerful tool for quantifying various aspects of the marine carbon cycle, especially when combined with measurements of total DIC and alkalinity (ALK). The value of time-series measurements of ocean carbon chemistry has been demonstrated in studies of the perturbation of the oceanic carbon cycle resulting from increasing atmospheric CO_2 (Keeling, 1993; Winn et al., 1994;

Bacastow et al., 1996; Bates et al., 1996; Gruber et al., 1996; Winn et al., 1998; Gruber et al., 1998; Gruber and Keeling, 2001; Gruber et al., 2002; Quay and Stutsman, 2003; Keeling et al., 2004; Brix et al., 2004). These records gain value as they grow longer because this improves our ability to quantify long-term trends, seasonality, and natural variability, and also improves our confidence in long-term changes to observed carbon cycle dynamics. Additionally, their value for validating ocean carbon cycle models increases as record lengths increase.

The observed long-term trends of increasing DIC and decreasing δ^{13}C-DIC in the surface ocean primarily reflect the uptake of anthropogenic carbon and transfer of the atmospheric isotopic trend of decreasing $\delta^{13}C_{atm}$ into the surface ocean (Bacastow et al., 1996; Gruber et al., 1999; Heimann and Maier-Reimer, 1996; McNeil et al., 2001; Quay et al., 2003; Sonnerup et al., 1999; Tanaka et al., 2003; Watanabe et al., 2011). The surface ocean values of δ^{13}C-DIC are mainly controlled by the atmospheric δ^{13}C trend and air-sea gas exchange, the entrainment of deeper water into the surface mixed layer, and the impacts of photosynthetic fractionation which leaves an enriched (more positive) δ^{13}C-DIC signal. Any (or all) of these factors might alter the balance between air-sea gas exchange and biological cycling that results in the linear trend in the past δ^{13}C records at S-BATS and ALOHA.

Tagliabue and Bopp (2008) used the PISCES-A global ocean ecosystem model to investigate spatiotemporal variability in δ^{13}C-DIC and the Suess effect. They report large regional variability in the long-term trends of δ^{13}C-DIC (Tagliabue and Bopp, 2008; see Figure 7A), and a range of values for the Suess effect (or long-term trend resulting from the fossil-fuel driven dilution of atmospheric ^{13}C) in the subtropical gyres between approximately -0.016 and -0.024 ‰ yr^{-1}. Previous publications of observed trends in δ^{13}C-DIC at HOT and BATS yield a range of computed trends from -0.024 to -0.027 ‰ yr^{-1} (Keeling et al., 2004; Quay et al., 2017,

2003). sDIC computed trends at BATS and HOT have ranged between 0.64 ± 0.05 μmol kg^{-1} yr^{-1} and 1.2 ± 0.1 μmol kg^{-1} yr^{-1} (Bates et al., 2014; Gruber et al., 2002; Keeling et al., 2004; Quay et al., 2017, 2003).

The seasonal cycle of DIC, δ^{13}C-DIC, and other upper ocean parameters are also of interest, as they may be diagnostic of changes in productivity patterns as a result of possible climate change impacts. The amplitudes of both sDIC and δ^{13}C-DIC are twice as large at BATS as at HOT (Keeling et al., 2004), and illustrate distinct regional processes that impact the carbon cycle at the locations. Recent studies have shown that the seasonal cycle of pCO_2 in the ocean has increased (Kwiatkowski and Orr, 2018; Landschützer et al., 2018) as a consequence of the rise in CO_2 and weaker ocean buffering. This increase is expected even without any change in either the amplitude of DIC or SST. Using an observation-based interpolation map between 1985 and 2014, Landschützer et al. (2018) report an increase in the surface ocean pCO_2 seasonal amplitude of 2.2 ± 0.4 μatm $decade^{-1}$ between 10°N and 40°N.

In addition to the long-term trends and seasonal cycles in the time-series record, there is also interannual and decadal variability observed in the North Atlantic and North Pacific (Bates, 2001, 2012, 2007; Bates et al., 1996; Brix et al., 2004; Conway et al., 1994; Gruber et al., 2002). These ocean basins exhibit distinct physical forcing, which is reflected in the observed contrasting relationships of variability between the two stations. Aside from improving our understanding of carbon cycle dynamic in general, understanding the controls of interannual variability in these regions can help to improve our ability to predict how the surface ocean carbon cycle may respond to future climate change. At S-BATS, interannual variations in SST and resulting mixed layer depth maxima seem strongly connected to interannual variability in DIC and δ^{13}C-DIC (Gruber et al., 2002), while at ALOHA, variations in SST and gyre

circulation (lateral transport) seem to be the dominant forces (Brix et al., 2004). These different mechanisms were determined from a box model analysis making use of the simultaneous records of δ^{13}C-DIC and DIC (Gruber et al., 1998).

Previous studies have also suggested that the observed interannual variability in sDIC are related to the dominant climate modes of variability in these regions (Dore et al., 2003; Gruber et al., 2002; Keeling et al., 2004; McKinley et al., 2006). For example in the North Atlantic, (Gruber et al., 2002) reported that there was significant correlation between the North Atlantic Oscillation (NAO) and sDIC ($r = -0.67$), SST ($r = 0.63$), and MLD ($r = -0.49$) within the 95% confidence interval during the winter months (DJFM). However, they did not find significant correlations between the NAO and δ^{13}C-DIC variability in the 18-year record.

In the North Pacific, (Brix et al., 2004) reported that less than 20% of the variability in HOT Station ALOHA measurements of sDIC could be attributed to the Pacific Decadal Oscillation (PDO), and less than 5% of the observed variability could be attributed to the El Nino Southern Oscillation (ENSO). Brix et al., (2004) also did not find significant correlations of these climate modes or any of the other time-series variables with HOT δ^{13}C-DIC variability. However, more recent studies suggest that there may be broader regional connections between the PDO and ENSO (Newman et al., 2016), and it is possible that there may be patterns of variability that may be detectable now with ~3 decades of data available that were not present in the shorter record. Additionally, signals of tropical salinity anomalies resulting from the 2015/2016 extreme ENSO event were advected northward as far as Hawaii (Hasson et al., 2018). This suggests that it may in fact be possible to detect the influence of certain anomalies from ENSO near Hawaii, depending on the strength of the event.

Here, we report ~34 year time-series of dissolved inorganic carbon (DIC), alkalinity (ALK), and stable carbon isotopes of DIC (δ^{13}C-DIC) in the surface ocean from samples collected between 1983 and 2017 in the North Atlantic (Hydrostation 'S' and BATS) and between 1989 and 2016 in the North Pacific (HOT) analyzed at Scripps. Earlier portions of these time-series (through 2002) have been reported in investigations of the carbon cycle in the North Atlantic (Keeling, 1993; Marchal et al., 1996; Bacastow et al., 1996; Gruber et al., 1998; Gruber and Keeling, 1999; Gruber et al., 2002; Brix et al., 2004) and North Pacific (Winn et al., 1994; Karl and Lukas, 1996; Michaels and Knap, 1996; Bates et al., 1996, 1998; Winn et al., 1998; Brix et al., 2004; Keeling et al., 2004). The extended records include an additional 14 to 15 years of combined DIC, ALK, and δ^{13}C-DIC data not discussed in previous publications. This dataset represents the longest time-series of δ^{13}C-DIC available anywhere.

We describe trends and characteristics observed in the data that are better resolved due to the longer records focusing on three primary questions:

(1) What are the long-term trends in the time-series records, do they change over time, and how do they compare to earlier studies?

(2) Do we see any long-term changes in the seasonal cycle of δ^{13}C-DIC, sDIC, or pCO_2?

(3) How is interannual variability related to basin-scale drivers of variability, and how do these compare with earlier findings?

3.2 METHODS

3.2.1 Stations

The two stations in the North Atlantic are Station S, located ~26 km southeast of the island of Bermuda (32°10'N, 64°30'W), and the JGOFS Bermuda Atlantic Time-series Study (BATS) site located ~80 km southeast of Bermuda (31°50'N, 64°10'W) (Bates et al., 1996). The

third sampling site is the Hawaii Ocean Time-series (HOT) station ALOHA, located ~100 km north of the island of ‘Oahu (22°45’N, 158°00’W) (Karl and Lukas, 1996). Figure 1 shows mapped locations of each of the time-series stations.

BATS and Station S show comparable long-term trends and seasonal cycles and have been combined in earlier studies into one representative dataset for the region (Gruber et al., 2002; Brix et al., 2004). The extended record shows similar agreement between Station S and BATS; for the remainder of this paper Station S and BATS is treated as one continuous record in the North Atlantic subtropical gyre and will be referred to as ‘S-BATS’. In the North Pacific subtropical gyre, we refer to HOT Station ALOHA as ‘HOT’.

3.2.2 Sampling

Seawater samples are collected approximately monthly at each of the three time-series stations following established protocols for gas sampling (DOE, 1994). Sampling depths for DIC, ALK, and δ^{13}C-DIC are 10 m for S-BATS and 5 m for HOT. Samples are drawn in duplicates for shore-based analyses from Niskin bottles into 580 ml glass reagent bottles and poisoned with ~100-200 µl of mercuric chloride solution to prevent biological activity and preserve the samples (DOE, 1994). Sample bottles are sealed shut with ground-glass stoppers greased with Apiezon L vacuum grease and secured in place to be shipped back to Scripps Institution of Oceanography. Once received, sample bottle seals are inspected for leaks then stored until analysis.

3.2.3 Sample Analysis

DIC measurements are made using a CO_2 vacuum extraction technique and manometric analysis. Dilute phosphoric acid is added to an aliquot of seawater subsampled from a sample bottle to convert all of the DIC to CO_2(g). Cryogenic traps are used to isolate the CO_2(g), which

is then transferred into a constant volume manometer, or sealed into a "break seal" glass tube and saved for subsequent manometric analysis (Guenther et al., 2001; Lueker et al., 1998). ALK measurements employ an open-cell potentiometric titration method using dilute hydrochloric acid (Dickson et al., 2003). Both ALK and salinity measurements on bottle samples are done in Prof. Andrew Dickson's lab. We removed the variations in DIC and ALK attributable to the effects of variability in salinity due to precipitation and evaporation by normalizing these data to a constant salinity of 35.0 (Bates et al., 1996; Keeling, 1993), and refer to these salinity normalized values as sDIC and sALK respectively. The normalization value of 35.0 is used to be consistent with the normalization applied to previously published versions of this record (Brix et al., 2004; Gruber et al., 2002, 1998; Keeling et al., 2004).

We use the DIC and ALK along with SST, salinity, and pressure data to calculate the CO_2 partial pressure in the surface ocean (pCO_2). Pressure was determined from sample depth for each sample using the MATLAB Gibbs Seawater (GSW) Oceanographic Toolbox (McDougall and Barker, 2011, v3.05.5). *p*CO2 was computed using the CO2SYS MATLAB package (Lewis and Wallace, 1998; van Heuven et al., 2011) with the recommended formulations (Dickson et al., 2007) of the carbonic acid dissociation constants K_1 and K_2 from (Lueker et al., 2000), KSO_4 dissociation constants from (Dickson, 1990), and borate to silicate ratio formulation from (Uppström, 1974).

Measurements of δ^{13}C-DIC in seawater are made after the manometric DIC analysis is complete as described above. The CO_2 gas is re-sealed into a "break-seal" glass tube, then the isotopic composition of the sample is measured on a dual-inlet stable isotope ratio mass spectrometer (IRMS). Details on the instruments used and calibration for measurements of δ^{13}C-DIC are described in Chapter 2.

3.2.4 Additional Data Sources

Sea surface temperature (SST) measurements are made using a calibrated Seabird CTD at the time of sampling, this meta data is provided with the corresponding sample bottles from each sampling program. CTD profiles for the time-series locations were obtained from the Bermuda Institute of Ocean Science (BIOS) S-BATS program (http://bats.bios.edu/data). Mixed Layer Depths (MLD) for HOT were obtained from the HOT program (http://hahana.soest.hawaii.edu/hot/hot-dogs/mldepth.html). We computed MLD values for S-BATS from CTD profile data. We use a potential density difference of 0.125 kg m^{-3} between the surface and the base of the mixed layer for each of the time-series stations (Levitus, 1982). The MLD data from S-BATS and HOT are monthly, typically coinciding with the cruises that the Scripps seawater samples were also obtained on.

Atmospheric monthly data of $\delta^{13}C_{atm}$ and $CO_{2\text{-}atm}$ were obtained from the Scripps CO_2 Program (Keeling et al., 2001). We use the Cape Kumukahi, Hawaii (KUM; 19.5°N 154.8°W) station data (scrippsco2.ucsd.edu/data/atmospheric_co2/kum.html) for comparison with the HOT data which is at sea level and in close proximity to HOT. We selected the La Jolla, California (LJO; 32.9°N 117.3°W) station data (scrippsco2.ucsd.edu/data/atmospheric_co2/ljo.html) for comparison with S-BATS. LJO was selected to be representative of the atmospheric CO_2 values for S-BATS because they are located at a similar latitude, LJO agrees well with local measurements, and LJO provides atmospheric data prior to 1989 (Bates et al., 1998; Conway et al., 1994; Lueker et al., 1998).

To compare with seawater pCO_2, we convert the atmospheric volume fraction of dry air, $CO_{2\text{-}atm}$ (ppm), to the atmospheric partial pressure of CO_2 ($pCO_{2\text{-}atm}$(μatm)) adjusting to the saturated water vapor pressure using the following approximation:

$$pCO_{2\text{-}atm} = xCO_{2\text{-}atm} * (p_{air} - p_{H2O}) \quad (3.1)$$

where $xCO_{2\text{-}atm}$ is the atmospheric mole fraction, p_{air} is one standard atmosphere (1.01325 bar), (Keeling et al., 1989; Lueker et al., 1998), and p_{H2O} is the saturated vapor pressure at the observed SSTcomputed using best practices (Dickson et al., 2007).

We obtained North Atlantic Oscillation (NAO) monthly index data from the National Oceanic and Atmospheric Administration (NOAA) National Weather Service (NWS) Climate Prediction Center website for the NAO (https://cpc.ncep.noaa.gov/data/teledoc/nao.shtml). The strength of the NAO forcing experienced at S-BATS is typically greatest in the winter months, so we use the winter mean value of the NAO index during December, January, February and March (DJFM).

The Pacific Decadal Oscillation (PDO) monthly index is based on the leading principal component of the monthly SST anomalies in the Pacific Ocean, north of 20°N (Mantua et al., 1997). We obtained PDO index standardized data from Joint Institute for the Study of the Atmosphere and Ocean (JISAO), University of Washington website (http://research.jisao.washington.edu/pdo/).

We use the NINO3.4 index to represent the El Niño Southern Oscillation (ENSO) climate variability which is based on monthly SST anomalies over the Pacific Ocean region within 5°N to 5°S and 170°W to 120°W. Monthly NINO3.4 data was obtained from the NOAA National Weather Service Climate Prediction Center website (https://www.cpc.ncep.noaa.gov/data/indices).

The data for the North Pacific Gyre Oscillation (NPGO) – based on the second Empirical Orthogonal Function (EOF) of sea surface height variability in the Northeast Pacific (Di Lorenzo et al., 2008) – was obtained from Di Lorenzo's NPGO website (www.o3d.org/npgo).

3.2.5 Curve Fitting and Trend Analysis

The observed variability in the time-series records was divided into three components:

$$X = Xseas + Xtrend + Xresid \quad (3.2)$$

where X is the measured time-series record of a given variable, *Xtrend* is the long-term trend based on a quadratic fit. *Xseas* represents the seasonal cycle and is calculated using 4-, 6-, and 12-month harmonics. The quadratic and harmonic fit were obtained in a single computational step. *Xresid* is the residual variability or residual anomalies after *Xseas* and *Xtrend* have been removed. We obtained the mean seasonal cycle from the 3-harmonic fit of *Xseas* and computed the mean seasonal amplitude for each variable using the difference between the max and min values of the mean seasonal cycle. We fit *Xresid* with a cubic spline (*Xspline)* to smooth these anomalies and emphasize interannual variability. We fit the de-seasonalized data (X - *Xseas*) with a least-squares linear regression fit to obtain the long-term linear trend, along with 95% confidence intervals.

In order to track year-to-year changes in seasonal amplitude, we used a metric derived by taking the mean value of the three months centered around the peak and trough of the mean seasonal cycle for each variable each year. A difference of these averaged minimum and maximum values was then calculated to yield estimate of the amplitude for the seasonal cycle each year. We used the mean value of multiple sample bottles to avoid biasing the seasonal amplitude due to a single anomalous value. Due to sparse or missing data, we were unable to compute an amplitude for all years. As a result of the failure of a sample storage refrigerator at SIO, 2006 seasonal amplitude data is not available at S-BATS. Additionally, S-BATS is missing seasonal amplitude data for pCO_2 from 1983 to 1985 and 2012 as well as for MLD in 1984 due

to a lack of either the maximum or minimum months in available samples. At HOT, seasonal amplitude values are not available for δ^{13}C-DIC, SST, and pCO_2 in 2015.

We used a jack-knife method to examine whether the timing of the seasonal cycle phase has shifted (Graven et al., 2013). This was done by binning the data by decade an carrying out the harmonic/quadratic fits for each decade. We repeated this fit for each decade over 1000 iterations, each time throwing out 30% of the data points selected at random. We then determined the time at which the max, min, and zero crossing occurred in each decade and evaluated whether these were significantly different from one another within a 95% confidence interval.

To explore the controls and characteristics of the interannual variability, we computed correlations between the time-series variables themselves as well as between the time-series data and various climate modes of variability. To do this, we computed monthly values of the time-series data obtained by subsampling *Xspline* (the cubic spline fit of *Xresid)* at monthly intervals, selecting for the 15th of each month. When evaluating the significance of correlations of time-series datasets, it is important to account for autocorrelation, or the fact that each datapoint is, to some extent, dependent on datapoints before it. We used a random phase test (Ebisuzaki, 1997) to determine the statistical significance of correlation coefficients and avoid over-confidence due to autocorrelation. This method involves simulating time-series with the same power spectrum as the observed time-series. We used 1000 iterations and compute the correlation coefficients of these simulated pairs of time-series. We report the likelihood that the correlation is not random by calculating the percentage of coefficients from the simulated data that are weaker than those from the observations.

To minimize the effects of localized variability in our analysis of secular trends and the role of SST in observed surface ocean carbon variability, we considered only the data collected at times of observed SST minima. These values are obtained by identifying the minimum SST value in a given year within the three months nearest the mean seasonal cycle minimum. The sDIC and δ^{13}C-DIC corresponding to this SST minimum are then isolated and compared with the minimum SST values.

3.3 RESULTS

3.3.1 Overall trends

Figure 3.2 (S-BATS) and Figure 3.3 (HOT) show the time-series data of δ^{13}C-DIC, salinity normalized DIC (sDIC), salinity normalized ALK (sALK), and both seawater and atmospheric pCO_2 along with measurements of SST, salinity, and mixed layer depth (MLD) through 2017. This update adds ~15 years of δ^{13}C-DIC relative to previously published data. These plots include a solid line fit of combined *Xtrend* + *Xseas* + *Xspline*.

Figure 3.4 shows deseasonalized data for sDIC, δ^{13}C-DIC, pCO_2, and sALK with long-term trends–determined using a least-squares linear regression fit on the seasonally detrended data–reported with 95% confidence intervals in parentheses. We summarize the long-term trends in Table 3.1, and include trends calculated over the approximate first and second half of the records at each station–centered around the year 2000.

We see higher trends in sDIC (outside of 95% confidence intervals) at both S-BATS and HOT after 2000. At S-BATS, the long-term trend in sDIC is+0.62 μmol kg^{-1} yr^{-1} for the time period of 1983-2000 and increases to +1.34 μmol kg^{-1} yr^{-1} for the subsequent period of 2001-2017. At HOT, sDIC trend increases from +1.30 μmol kg^{-1} yr^{-1} in the 1989-2000 period to +1.72 μmol kg^{-1} yr^{-1} in the 2001-2016 period. The δ^{13}C-DIC trend at S-BATS also accelerates (outside

of 95% confidence intervals), changing from -0.0238‰ yr^{-1} during 1983-2000 to -0.0296‰ yr^{-1} during 2001-2017. In contrast, at HOT the δ^{13}C-DIC trend slows (outside of 95% confidence intervals) from -0.0274‰ yr^{-1} for the time period of 1989-2000 to -0.0231‰ yr^{-1} for 2001-2016. The pCO_2 trends, along with the remaining time-series variables, have overlapping confidence intervals for all time-periods where the trends are computed.

3.3.2 Seasonal Cycles

Figure 3.5 and Figure 3.6 show the climatological seasonal cycles of the same datasets (computed from *X – Xtrend* collapsed into a single year) along with a 3-harmonic fit of the mean seasonal cycle. Seasonal peak-to-peak amplitude and timing for maximum and minimum values are summarized in Table 3.2. The mean seasonal amplitude for δ^{13}C-DIC is 0.159 ± 0.039‰ and 0.083 ± 0.051‰ at HOT. The mean seasonal amplitude for sDIC is 25.09 ± 4.8 μmol kg^{-1} at S-BATS and 11.74 ± 6.2 μmol kg^{-1} at HOT.

Figure 3.8 and Figure 3.9 show the time-series of annually resolved seasonal amplitude of sDIC, δ^{13}C-DIC, SST, MLD, and pCO_2 computed from the average of three monthly values centered around the mean seasonal cycle maximum and minimum for each variable. To assess whether there were long-term trends in the amplitude, we fit these points to a linear regression model. This yielded trends which were not statistically significant (within the 95% confidence interval) for all the variables in Figure 3.8 and Figure 3.9.

3.3.3 Interannual variability

Figure 3.10 and Figure 3.11 show the residual anomalies (*Xresid = X – Xtrend – Xseas;* data points*)* at each station along with a cubic spline (*Xspline;* solid line*)* fit to these residuals. For both sDIC and δ^{13}C-DIC, the range of interannual variability is close to the magnitude of the seasonal amplitude at both S-BATS and HOT. At S-BATS anomalies for sDIC vary around

± 6 μmol kg^{-1} and δ^{13}C-DIC anomalies vary around ± 0.07‰, with a strong negative anomaly at the onset of the record of 0.11‰ in 1983. We observe SST anomalies at S-BATS of ± 0.85 °C. AT S-BATS, MLD anomalies exist over a wide range of values with winter MLD regularly reaching depths of ~125m and varying down to depths of nearly 400m. Salinity variability is relatively small (± 0.2) and sALK anomalies vary around ± 0.2 μmol kg^{-1}.

At HOT, the residual anomalies for sDIC vary around ± 5 μmol kg^{-1} except for 2012/2013 in which the positive anomalies exceed ± 10 μmol kg^{-1} at HOT; δ^{13}C-DIC anomalies reach between ± 0.05‰. We also see positive SST anomalies up to 1 °C in the spline fits and negative SST anomalies down to 0.9 °C. The pronounced negative SST anomaly in 2012/2013 coincides with the largest positive sDIC anomaly, a negative δ^{13}C-DIC anomaly, a positive pCO_2 anomaly, and a positive (deeper) MLD anomaly. Salinity anomalies at HOT have a lower frequency and nearly twice the peak-to-peak amplitude of those observed at S-BATS. We see systematic shifts in sALK up to 4-5 μmol/kg. MLD anomalies at HOT are also relatively small, on the order of ± 20 m.

Correlation coefficients between *Xspline* subsampled at monthly intervals for each variable along with significance are summarized in Table 3.4. At S-BATS we find significant negative correlation between the monthly anomalies of sDIC and SST (r = -0.79), and between sDIC and MLD (r = -0.28). We see a positive correlation between δ^{13}C-DIC and SST anomalies (r = +0.37), as well as a strong correlation between sDIC and δ^{13}C-DIC (r = -0.59). SST and pCO_2 also exhibit a positive correlation (r = +0.36). Figure 3.12 shows the relationship between observations at S-BATS and the NAO, focusing averages over winter months (DJFM). We find significant correlation between the NAO_{DJFM} and the following variables: $sDIC_{DJFM}$ (r = -0.57), SST_{DJFM} (r = +0.52), and MLD_{DJFM} (r = -0.29).

At HOT we find significant correlation between *Xspline* subsampled at monthly intervals of sDIC and the following variables: SST (r = -0.64), MLD (r = -0.52), pCO_2 (r = +0.54), and sALK (r = +0.49). Figure 3.13 explores the relationship at HOT with the monthly PDO, NINO3.4, and NPGO indices. We find significant negative correlation between monthly sDIC and the PDO (r = -0.49) and NINO3.4 (r = -0.33). The PDO was also significantly correlated with pCO_2 (r = -0.27), SST (r = +0.39), and MLD (-0.30); and NINO3.4 was also significantly correlated with MLD (r = +0.32). The NPGO was only significantly correlated with MLD (r = +0.41). δ^{13}C-DIC does not correlate with any of the remaining time-series variables we looked at, including a broad lack of significant correlation with the climate indices we explored.

3.4 DISCUSSION

3.4.1 Overall trends

The long-term trends of increasing sDIC and decreasing δ^{13}C-DIC primarily reflect the observed changes in CO_2 concentrations and isotopic values in the atmosphere (Bacastow et al., 1996; Bates, 2001) which are primarily driven by anthropogenic burning of fossil fuels (Le Quéré et al., 2018). Burning fossil fuels increases the concentration of CO_2 in the atmosphere, and this results in a net oceanic uptake over time of anthropogenic CO_2 and contributes to the observed increase in surface seawater DIC. Additionally, fossil fuel combustion dilutes the atmospheric $\delta^{13}C_{atm}$ signal (termed the Suess effect), and this signal of decreasing $\delta^{13}C_{atm}$ is also transferred into the surface ocean via air-sea gas exchange and disequilibrium flux (or direct atom-swapping, even in the absence of net uptake of anthropogenic CO_2). This combination of factors leads to the observed trend of decreasing δ^{13}C-DIC in surface seawater.

At both S-BATS and HOT the observed trend in sDIC is similar to the previous publication of Bates et al. (2014), who used completely independent records. At S-BATS, we

find +1.07 μmol kg^{-1} yr^{-1} (+1.02, +1.12) between 1983 and 2017 while Bates et al. (2014) report 1.12 ± 0.04 μmol kg^{-1} yr^{-1} from 1983 to 2013. At HOT we find +1.21 μmol kg^{-1} yr^{-1} (+1.12, 1.30) between 1989 and 2016 while Bates et al. (2014) report +1.05 ± 0.05 μmol kg^{-1} yr^{-1} between 1988 to 2014.

The observed sDIC trends are quite close to the theoretical trend of +1.06 μmol kg^{-1} yr^{-1} expected assuming the mixed layer is in equilibrium with rising atmospheric CO_2. This estimate was based on equilibrium carbon system chemistry (CO2SYS, see Methods) using atmospheric records from nearby latitudes of La Jolla, CA and Kumukahi, HI and neglects any changes in water temperature or alkalinity. This theoretical sDIC trend is the same at both stations.

The overall trends that we find for δ^{13}C-DIC are also similar to previously published estimates for both stations. At S-BATS we find at trend of -0.0264‰ yr^{-1} (-0.0268, -0.0260 ‰ yr^{-1}) from 1983 to 2017 while Gruber et al. (2002) reported -0.024 ± 0.001‰ yr^{-1} from 1983 to 2001. At HOT we find -0.0259 ‰ yr^{-1} (-0.0265, -0.0252) from 1989 to 2016, while Keeling et al. (2004) report -0.027 ± 0.001‰ yr^{-1} between 1988 to 2002, Quay et al. (2017) report -0.024 ± 0.001‰ yr^{-1} between 1988 to 2012. We note that Gruber et al. (2002) and Keeling et al. (2004) used shorter records of the time-series in this study, while Quay et al. (2017) used a completely independent dataset.

The observed δ^{13}C-DIC trend is also close but slightly higher than the trend in atmospheric δ^{13}C. Although a slower trend in δ^{13}C-DIC might be expected based on the slower equilibration rate of carbon isotopes compared to CO_2, the trend in δ^{13}C in the water is also strongly dependent on the past history of the δ^{13}C atmospheric trend, as discussed in Keeling et al (2004). As such, the faster rate of decrease observed in δ^{13}C-DIC relative to $\delta^{13}C_{atm}$ appears to reflect higher growth rates in atmospheric CO_2 in the early 1970s because there is a lag between

when the atmosphere reflects that change and when the signal would be transferred to the surface ocean δ^{13}C-DIC values.

One notable feature in our results is the similarity of the δ^{13}C-DIC trends both between the two stations and between the two timeframes (1984-2000 and 2001-2017). δ^{13}C-DIC trends estimated over these two separate time-frames range from -0.0231‰ yr^{-1} and -0296‰ yr^{-1}. And after nearly three decades, the trends in δ^{13}C-DIC show essentially the same nearly linear increase (within 95% confidence intervals) at both S-BATS and HOT stations of -0.0264‰ yr^{-1} and -0.0259‰ yr^{-1} respectively. This similarity between the stations is found despite the different cycles of productivity and physical forcing mechanisms found at the two locations. This also contrasts with some ocean biogeochemistry model results (Tagliabue and Bopp, 2008) which suggest that there are distinct rates of change at each of these locations in the subtropical gyres. Using the PISCES-A ocean-ecosystem model with the $^{13}C/^{12}C$ ratio included in seawater carbon pools, Tagliabue and Bopp (2008) report global trends of δ^{13}C-DIC between 1970 and 2000. These model results may underestimate these trends in subtropical gyre δ^{13}C-DIC, ranging between between -0.016‰ yr^{-1} and -0.024‰ yr^{-1}. The model also shows spatial variability across the gyres and between the North Atlantic and North Pacific. However, our time-series trends suggest that the rates of change are higher than these model estimates and are actually fairly consistent over time between the North Atlantic and North Pacific subtropical gyres.

3.4.2 Seasonal Cycle

The seasonal amplitudes for δ^{13}C-DIC, sDIC, pCO_2, SST, and MLD are all larger at S-BATS relative to HOT. The ~50% amplitude difference in δ^{13}C-DIC, sDIC, and pCO_2 between S-BATS and HOT can be explained in part by the difference in seasonal SST which in turn causes large differences in the maximum winter MLD and pCO_2, and varies over a wider range

of values at S-BATS. Another significant difference between the two stations is the timing of peak NCP and air sea gas exchange (Keeling et al., 2004). At S-BATS, air-sea gas exchange is seasonally impacted by the relative values of atmospheric and seawater pCO_2. The seawater pCO_2 near Bermuda is undersaturated (net uptake) in the winter and supersaturated (net outgassing) in the summer, while peak NCP occurs in spring and is thus not strongly opposing the gas exchange signal. In contrast, at HOT the seasonality in NCP more fully opposes the gas exchange component leading to smaller seasonal amplitudes. See further discussion in Sarmiento and Gruber (2006).

Seasonal and interannual variability occur as a result of natural processes that include air-sea gas exchange, physical water mass transport processes, and photosynthesis and respiration. Previous studies at both S-BATS and HOT have shown that sDIC exhibits a regular seasonal cycle, with the highest values occurring in late winter or early spring, and the lowest values occurring in late summer or early autumn (Bates et al., 1998, 1996; Brix et al., 2004; Gruber et al., 1998; Winn et al., 1998). This is in agreement with what we see (Figure 3.5 and Figure 3.6). The seasonal cycle for δ^{13}C-DIC is inversely correlated with that of sDIC with the minimum in late winter or early spring, and the maximum occurring in late summer or early autumn. The δ^{13}C-DIC seasonal cycle peaks due to photosynthetic fractionation which enriches mixed layer δ^{13}C-DIC during spring and summer and reaches a minimum due to vertical entrainment of remineralized organic matter, which is depleted in δ^{13}C, from below the mixed layer in the late winter (Gruber et al., 1998, 2002; Keeling et al., 2004).

The seasonal cycle in sDIC is nearly opposite in phase to the seasonal cycle in SST at both S-BATS and HOT, due in part to sDIC temperature dependency of air-sea gas exchange as well as the impact of MLD and vertical entrainment variability. The maxima and minima in the

seasonal cycle of sDIC and δ^{13}C-DIC vary interannually both in magnitude and in seasonal timing. This variability results primarily from natural variability of SST from year to year which directly impacts how deep the maximum MLD. The MLD in a given year also determines the degree of entrainment of nutrients from below the mixed layer and can impact the strength of biological productivity in a given year (Gruber et al., 1998, 2002).

This vertical control of DIC and δ^{13}C-DIC variability is especially dominant at S-BATS which shows large SST seasonality and variability, and experiences MLD reaching as deep as 400 m during especially cold and stormy years. The colder the SSTs, the deeper the mixed layer, and the higher the corresponding sDIC observed at the surface due to entrainment of deep, cold water with high amounts of remineralized sDIC (Gruber et al., 1998, 2002; Lueker et al., 1998). With colder SST, air-sea gas exchange is also enhanced and contributes to increasing sDIC as well. In contrast, HOT has been shown to be dominated by lateral advection in the North Pacific subtropical gyre with shallow mixed layer depths relative to those in the North Atlantic resulting in relatively less vertical mixing (Brix et al., 2004; Dore et al., 2009; Letscher et al., 2016).

As discussed previously e.g. (Sarmiento and Gruber, 2006) the seasonal cycle in pCO2 at both HOT and S-BATS is dominated by the seasonal cycle in temperature which is partially but not fully opposed by the variation in DIC. In Figure 3.7 we illustrate this point using an annual climatology formed from the full records at both stations. The thermal component shows what we might expect to see in pCO_2 from SST changes when DIC is held constant at a mean of 1962 μmol kg^{-1} (S-BATS) and 1978 μmol kg^{-1} (HOT)). The sDIC contribution shows expected pCO_2 changes from DIC when SST is held constant at a mean value of 23.5ºC (BATS) and 24.8ºC (HOT).

Using a linear regression analysis, we do not find significant trends in the seasonal amplitude of any of the variables DIC, (δ^{13}C-DIC, pCO_2, SST, and MLD) at either BATS or HOT (see Figure 3.8 and Figure 3.9. The lack of an amplitude trend in pCO_2 is in contrast to several recent studies that report changes in the pCO_2 seasonal cycle amplitude (Kwiatkowski and Orr, 2018; Landschützer et al., 2018), as well as what we might expect as a consequence of increasing DIC in the surface mixed layer and weaker ocean buffering. A potential reason for this discrepancy may be that the gridded product in Landschutzer et al (2018) is an average of their observation-based interpolation of pCO_2 values for the large region contained within 10°N to 40°N across the northern ocean basins. It is possible that regional variability is such that these trends do not show up in our time-series datasets.

3.4.3 Interannual Variability

At S-BATS, our results show a strong correlation between interannual anomalies in δ^{13}C-DIC and sDIC. This result is consistent with earlier findings showing that forcing from SST and MLD fluctuations, and resultant vertical mixing, is the dominant driver of observed variability of δ^{13}C-DIC and sDIC on interannual timescales of ~2-10 years (Bates, 2001; Gruber et al., 2002). During anomalously cold years, maximum MLD extends deeper and entrains water from below the mixed layer that is DIC rich and contains a much more negative δ^{13}C-DIC signal. During anomalously warm years, we observe shallower maximum MLD with lower sDIC and more positive δ^{13}C-DIC. As shown in previous studies (Bates, 2001; Gruber et al., 2002; Keller et al., 2012), we find that the interannual variability in SST, MLD, sDIC and δ^{13}C-DIC at S-BATS is significantly correlated with the NAO, which impacts the intensity and frequency of storms near Bermuda.

At HOT, we find no significant correlation between the interannual anomalies of δ^{13}C-DIC and sDIC. This suggests that interannual variability in vertical mixing is less important at HOT than at S-BATS, as both stations have strong vertical gradients in both variables (higher sDIC and lower δ^{13}C-DIC at depth). Previous studies have suggested that horizontal advection and/or air-sea gas exchange, along with associated horizontal variations in nutrient supply and water mass shifts in the gyre circulation near Hawaii are more important drivers of interannual variations in sDIC (Brix et al., 2004; Dore et al., 2009; Letscher et al., 2016).

At HOT, part of the decoupling of sDIC and δ^{13}C-DIC variability may be attributable to the difference in equilibration timescales between these two variables. The equilibration timescales are approximately one year for sDIC and roughly ten years for δ^{13}C-DIC (Broecker and Peng, 1974; Jones et al., 2014). This is part of why sDIC shows more sensitivity to interannual variability in SST, while the δ^{13}C-DIC trend essentially has an inherent ~10-year smoothing function applied to it. This also means that, as a result, the δ^{13}C-DIC signal is more sensitive to the amount of physical mixing and fractionation due to photosynthesis and respiration in the surface mixed layer, and less sensitive to atmospheric control on an interannual basis.

Consistent with Brix et al (2004), we find that sDIC and pCO_2 at HOT are both significantly correlated with the PDO. With the extended HOT records, we now also find that SST and MLD are correlated with the PDO, and we find that sDIC and MLD are significantly correlated with NINO3.4. These correlations were not evident with the shorter record. This correlation with NINO3.4 supports some recent publications showing connections between the NINO3.4 signal and the carbon cycle in the tropical and subtropical North Pacific (Chatterjee et

al., 2017). We also find no significant correlation between any of the measured variables and the NPGO except for MLD.

At HOT, it is interesting that δ^{13}C-DIC interannual variability is not significantly correlated with any other variables or climate modes, even while sDIC and MLD are correlated. We hypothesize that both sDIC and MLD are both controlled mainly by SST variability, with sDIC mostly influenced by air-sea exchange via the temperature-dependence of equilibrium chemistry, and MLD influenced by changes in vertical stability but rarely extending deep enough to have a dominating influence on carbon. In contrast to sDIC, δ^{13}C-DIC is less controlled by SST variability on interannual timescales because of its slower equilibration rate. This hypothesis is consistent with relevant timescales. The variability observed in climate modes like the PDO and NINO3.4 occur on interannual to decadal timescales, and the distinct equilibration timescales for δ^{13}C-DIC and sDIC, as mentioned previously, are on the order of ~10 years and ~1 year respectively (Broecker and Peng, 1974; Jones et al., 2014). It is therefore understandable that δ^{13}C-DIC signal might not respond to the short-term forcing driven by these patterns of variability, due to its much longer equilibration timescale even while DIC does respond.

We suggest that δ^{13}C-DIC variability at HOT is likely connected to horizontal advection and biological productivity within the mixed layer as discussed by Brix et al. (2004) but evidently via processes that are not strongly connected with the dominant climate modes. It is also important to note that recent studies suggest that the PDO is not an independent phenomenon, but is instead the sum of relative contributions from fluctuations in the Aleutian Low in the North Pacific and El Niño Southern Oscillation (ENSO) in the Tropical Pacific, as well as stochastic forcing and gyre circulation variability depending on the timescale (Newman et al., 2016). As such, correlation between the PDO and some of these variables at HOT suggests

mechanisms driving variability from a variety of sources that impact the subtropical gyre region near HOT. Additionally, the location of HOT is on the node of variability for the east-west bimodal pattern observed in the PDO (e.g. Chapter 4, see Figure 4.11; Newman et al., 2016, see Figure 1(a); and others). This pattern, and thus the location of the node, varies and as a result may adjust the drivers of variability that the time-series station at HOT actually experiences or result in regime shifts. This ultimately serves to make it difficult to ascribe the overall variability signal captured in the data at HOT to any specific source of forcing as discussed by other studies (Brix et al., 2004; Kavanaugh et al., 2018; McKinley et al., 2006). This may be especially true for some biological signals, which would further explain the lack of correlation between our observations and the δ^{13}C-DIC record.

The HOT time-series record also shows interesting anomalies in recent years, especially over the time period that encompasses the North Pacific warm anomalies that were prevalent over a large portion of the northeast Pacific between 2013 and 2015 (Bond et al., 2015; Cavole et al., 2016). In 2012–the period preceding the warm anomaly–the largest positive sDIC anomalies observed in the record coincided with negative SST anomalies along with a short-lived deep MLD and a corresponding negative anomaly in δ^{13}C-DIC. This combination of anomalies suggests a localized and short-lived mixing event which entrained DIC rich water with low δ^{13}C-DIC into the mixed layer.

In late 2013, a transition to a positive PDO occurred, immediately followed by the 2015/2016 ENSO event. Also, in late 2013, the SST at HOT shifted to a positive anomaly that persisted through the beginning of 2016, reflecting the propagation of the North Pacific warm anomalies to the region at HOT. Positive pCO_2 anomalies in 2013 and 2014 also appear to reflect the impact of these North Pacific warm anomalies (Sutton et al., 2017). Our record extends

beyond Sutton et al. (2017) which ended in 2014, and also shows notable negative anomalies in both sDIC and pCO_2 immediately following the warm anomaly during the 2015/2016 ENSO period.

3.4.3 Summary

In these time-series records of nearly three decades, we show that the long-term trends in sDIC and δ^{13}C-DIC at both S-BATS and HOT are consistent with earlier studies and independent time-series records (Bates et al., 2014; Gruber et al., 2002; Keeling et al., 2004; Quay et al., 2017). We find that the trend in sDIC at both stations is close to what we expect if full equilibration with the atmosphere is assumed. We also observe seasonal cycles of the time-series variables at both S-BATS and HOT that are consistent with earlier studies (Bates et al., 1998, 1996; Brix et al., 2004; Gruber et al., 1998; Winn et al., 1998). We examined the seasonal cycles over the full record and find that we do not observe any long-term changes in the seasonal cycle of sDIC, δ^{13}C-DIC, or pCO_2.

Finally, we explored the interannual variability and relationships between our observations and dominant modes of climate variability. We find relationships that are similar to earlier studies at both S-BATS and HOT (Bates, 2001, 2012, 2007; Bates et al., 1996; Brix et al., 2004; Conway et al., 1994; Gruber et al., 2002). For example, at S-BATS we see strong correlation between the winter-time NAO and sDIC, SST, and MLD. At HOT, we see correlation between the PDO and sDIC and pCO_2. With the extended record we now show significant correlation between the PDO and SST and MLD at HOT, as well as significant correlation between NINO3.4 and sDIC and MLD at HOT, neither of which was not evident with the shorter record.

This valuable dataset can be used to explore many aspects of the global carbon cycle including anthropogenic carbon uptake in the oceans and variations in marine productivity. It should also be used to test carbon parameters in ocean global circulation models, several of which now include stable isotope biogeochemistry in seawater, and to establish greater confidence in carbon budget estimates and climate predictions.

3.5 ACKNOWLEDGEMENTS

We would like to acknowledge Andrew Dickson, Guy Emanuele, and the Dickson Lab for all of the work they have contributed to maintaining this time-series record. In addition, we would like to thank the Bermuda Institute for Ocean Science (BIOS) and Hawaii Ocean Time-series (HOT) station personnel without whom these samples could not have been collected and this dataset would not be possible. Funding for this work was provided by the Schmidt Foundation.

Chapter 3, in part is currently being prepared for submission for publication of the material. Brooks, Mariela K; Lueker, Timothy J; Dickson, Andrew G, Emanuele III, Guy; Bollenbacher, Alane; Keeling, Ralph F. The dissertation author was the primary investigator and author of this material.

3.6 REFERENCES

Bacastow, R.B., Keeling, C.D., Lueker, T.J., Wahlen, M., 1996. The ^{13}C Suess effect in the world surface oceans and its implication for oceanic uptake of CO2: Analysis of observations at Bermuda. Global Biogeochemical Cycles 10, 335–346.

Bates, N., 2001. Interannual variability of oceanic CO_2 and biogeochemical properties in the Western North Atlantic subtropical gyre. Deep-Sea Research II 48, 1507–1528.

Bates, N., Astor, Y., Church, M., Currie, K., Dore, J., Gonaález-Dávila, M., Lorenzoni, L., Muller-Karger, F., Olafsson, J., Santa-Casiano, M., 2014. A Time-Series View of Changing Ocean Chemistry Due to Ocean Uptake of Anthropogenic CO_2 and Ocean Acidification. Oceanography 27, 126–141. https://doi.org/10.5670/oceanog.2014.16.

Bates, N.R., 2012. Multi-decadal uptake of carbon dioxide into subtropical mode water of the North Atlantic Ocean. Biogeosciences 9, 2649–2659. https://doi.org/10.5194/bg-9-2649-2012.

Bates, N.R., 2007. Interannual variability of the oceanic CO_2 sink in the subtropical gyre of the North Atlantic Ocean over the last 2 decades. Journal of Geophysical Research 112. https://doi.org/10.1029/2006JC003759.

Bates, N.R., Michaels, A.F., Knap, A.H., 1996. Seasonal and interannual variability of oceanic carbon dioxide species at the US JGOFS Bermuda Atlantic Time-series Study (BATS) site. Deep Sea Research Part II: Topical Studies in Oceanography 43, 347–383.

Bates, N.R., Takahashi, T., Chipman, D.W., Knap, A.H., 1998. Variability of pCO_2 on diel to seasonal timescales in the Sargasso Sea near Bermuda. Journal of Geophysical Research: Oceans 103, 15567–15585. https://doi.org/10.1029/98JC00247.

Bond, N.A., Cronin, M.F., Freeland, H., Mantua, N., 2015. Causes and impacts of the 2014 warm anomaly in the NE Pacific. Geophysical Research Letters 42, 3414–3420. https://doi.org/10.1002/2015GL063306.

Brix, H., Gruber, N., Keeling, C.D., 2004. Interannual variability of the upper ocean carbon cycle at station ALOHA near Hawaii. Global Biogeochemical Cycles 18. https:// doi.org/10.1029/2004GB002245.

Broecker, W.S., Peng, T.-H., 1974. Gas exchange rates between air and sea. Tellus 26, 21–35. https://doi.org/10.1111/j.2153-3490.1974.tb01948.x.

Cavole, L., Demko, A., Diner, R., Giddings, A., Koester, I., Pagniello, C., Paulsen, M.-L., Ramirez-Valdez, A., Schwenck, S., Yen, N., Zill, M., Franks, P., 2016. Biological Impacts of the 2013–2015 Warm-Water Anomaly in the Northeast Pacific: Winners, Losers, and the Future. Oceanography 29. https://doi.org/10.5670/oceanog.2016.32.

Chatterjee, A., Gierach, M.M., Sutton, A.J., Feely, R.A., Crisp, D., Eldering, A., Gunson, M.R., O'Dell, C.W., Stephens, B.B., Schimel, D.S., 2017. Influence of El Niño on atmospheric CO_2 over the tropical Pacific Ocean: Findings from NASA's OCO-2 mission. Science 358, eaam5776. https://doi.org/10.1126/science.aam5776.

Conway, T.J., Tans, P.P., Waterman, L.S., Thoning, K.W., Kitzis, D.R., Masarie, K.A., Zhang, N., 1994. Evidence for interannual variability of the carbon cycle from the National Oceanic and Atmospheric Administration/Climate Monitoring and Diagnostics Laboratory Global Air Sampling Network. Journal of Geophysical Research 99, 22831–22855. https://doi.org/10.1029/94JD01951.

Di Lorenzo, E., Schneider, N., Cobb, K.M., Franks, P.J.S., Chhak, K., Miller, A.J., McWilliams, J.C., Bograd, S.J., Arango, H., Curchitser, E., Powell, T.M., Rivière, P., 2008. North

Pacific Gyre Oscillation links ocean climate and ecosystem change. Geophysical Research Letters 35. https://doi.org/10.1029/2007GL032838.

Dickson, A.G., 1990. Standard potential of the reaction: AgCl(s) +1/2H_2(g) = Ag(s) + HCl(aq), and and the standard acidity constant of the ion HSO_4 in synthetic sea water from 273.15 to 318.15 K. Journal of Chemical Thermodynamics 113–127.

Dickson, A.G., Afghan, J.D., Anderson, G.C., 2003. Reference materials for oceanic CO_2 analysis: a method for the certification of total alkalinity. Marine Chemistry 80, 185–197. https://doi.org/10.1016/S0304-4203(02)00133-0.

Dickson, A.G., Sabine, C.L., Christian, J.R., Bargeron, C.P., North Pacific Marine Science Organization (Eds.), 2007. Guide to best practices for ocean CO_2 measurements, PICES special publication. North Pacific Marine Science Organization, Sidney, BC.

DOE, 1994. Handbook of methods for the analysis of the various parameters of the carbon dioxide system in sea water; version 2, A. G. Dickson & C. Goyet, eds., ORNL/CDIAC-74.

Dore, J.E., Lukas, R., Sadler, D.W., Church, M.J., Karl, D.M., 2009. Physical and biogeochemical modulation of ocean acidification in the central North Pacific. Proceedings of the National Academy of Sciences 106, 12235–12240.

Dore, J.E., Lukas, R., Sadler, D.W., Karl, D.M., 2003. Climate-driven changes to the atmospheric CO_2 sink in the subtropical North Pacific Ocean. Nature 424, 754–757. https://doi.org/10.1038/nature01885.

Ebisuzaki, W., 1997. A Method to Estimate the Statistical Significance of a Correlation When the Data Are Serially Correlated. Journal of Climate 10, 2147–2153. https://doi.org/10.1175/1520-0442(1997)010<2147:AMTETS>2.0.CO;2

Graven, H.D., Keeling, R.F., Piper, S.C., Patra, P.K., Stephens, B.B., Wofsy, S.C., Welp, L.R., Sweeney, C., Tans, P.P., Kelley, J.J., Daube, B.C., Kort, E.A., Santoni, G.W., Bent, J.D., 2013. Enhanced Seasonal Exchange of CO_2 by Northern Ecosystems Since 1960. Science 341, 1085–1089. https://doi.org/10.1126/science.1239207.

Gruber, N., Keeling, C.D., 2001. An improved estimate of the isotopic air-sea disequilibrium of CO_2: Implications for the oceanic uptake of anthropogenic CO2. Geophysical Research Letters 28, 555–558. https://doi.org/10.1029/2000GL011853.

Gruber, N., Keeling, C.D., 1999. Seasonal Carbon Cycle in the Sargasso Sea near Bermuda, 1st ed, Bulletin of the Scripps Institution of Oceanography. University of California Press.

Gruber, N., Keeling, C.D., Bacastow, R.B., Guenther, P.R., Lueker, T.J., Wahlen, M., Meijer, H.A.J., Mook, W.G., Stocker, T.F., 1999. Spatiotemporal patterns of carbon-13 in the

global surface oceans and the oceanic suess effect. Global Biogeochemical Cycles 13, 307–335. https://doi.org/10.1029/1999GB900019.

Gruber, N., Keeling, C.D., Bates, N.R., 2002. Interannual Variability in the North Atlantic Ocean Carbon Sink. Science 298.

Gruber, N., Keeling, C.D., Stocker, T.F., 1998. Carbon-13 constraints on the seasonal inorganic carbon budget at the BATS site in the northwestern Sargasso Sea. Deep-Sea Research I 45, 673–717.

Gruber, N., Sarmiento, J.L., Stocker, T.F., 1996. An improved method for detecting anthropogenic CO_2 in the oceans. Global Biogeochemical Cycles 10, 809–837.

Guenther, P.R., Bollenbacher, A.F., Keeling, C.D., Stewart, E.F., Wahlen, M., 2001. Calibration methodology for the Scripps 13C/12C and 18O/16O stable isotope program, 1996-2000. A Report Prepared for the Global Environmental Monitoring Program of the World Meteorological Organization.

Hasson, A., Puy, M., Boutin, J., Guilyardi, E., Morrow, R., 2018. Northward Pathway Across the Tropical North Pacific Ocean Revealed by Surface Salinity: How do El Niño Anomalies Reach Hawaii? Journal of Geophysical Research: Oceans 123, 2697–2715. https://doi.org/10.1002/2017JC013423.

Heimann, M., Maier-Reimer, E., 1996. On the relations between the oceanic uptake of CO_2 and its carbon isotopes. Global Biogeochemical Cycles 10, 89–110.

Jones, D.C., Ito, T., Takano, Y., Hsu, W.-C., 2014. Spatial and seasonal variability of the air-sea equilibration timescale of carbon dioxide. Global Biogeochemical Cycles 28, 1163–1178. https://doi.org/10.1002/2014GB004813.

Karl, D.M., Lukas, R., 1996. The Hawaii Ocean Time-series (HOT) program: Background, rationale and field implementation. Deep Sea Research Part II: Topical Studies in Oceanography 43, 129–156.

Kavanaugh, M.T., Church, M.J., Davis, C.O., Karl, D.M., Letelier, R.M., Doney, S.C., 2018. ALOHA From the Edge: Reconciling Three Decades of in Situ Eulerian Observations and Geographic Variability in the North Pacific Subtropical Gyre. Frontiers in Marine Science 5. https://doi.org/10.3389/fmars.2018.00130.

Keeling, C.D., 1993. Lecture 2: Surface ocean CO_2, in: The Global Carbon Cycle. NATO ASI Series, Series I: Global Environmental Change. Springer, Berlin, Heidelberg.

Keeling, C.D., Bacastow, R.B., Carter, A.F., Piper, S.C., Whorf, T.P., Heimann, M., Mook, W.G., Roeloffzen, H., 1989. A three-dimensional model of atmospheric CO_2 transport based on observed winds: 1. Analysis of observational data, in: Peterson, D.H. (Ed.),

Geophysical Monograph Series. American Geophysical Union, Washington, D. C., pp. 165–236. https://doi.org/10.1029/GM055p0165.

Keeling, C.D., Brix, H., Gruber, N., 2004. Seasonal and long-term dynamics of the upper ocean carbon cycle at Station ALOHA near Hawaii. Global Biogeochemical Cycles 18. https://doi.org/10.1029/2004GB002227.

Keeling, C.D., Piper, S.C., Bacastow, R.B., Wahlen, M., Whorf, T.P., Heimann, M., Meijer, H.A., 2001. Exchanges of atmospheric CO_2 and $^{13}CO_2$ with the terrestrial biosphere and oceans from 1978 to 2000.

Keller, K.M., Joos, F., Raible, C.C., Cocco, V., Frölicher, T.L., Dunne, J.P., Gehlen, M., Bopp, L., Orr, J.C., Tjiputra, J., Heinze, C., Segschneider, J., Roy, T., Metzl, N., 2012. Variability of the ocean carbon cycle in response to the North Atlantic Oscillation. Tellus B: Chemical and Physical Meteorology 64, 18738. https://doi.org/10.3402/tellusb.v64i0.18738.

Kwiatkowski, L., Orr, J.C., 2018. Diverging seasonal extremes for ocean acidification during the twenty-first century. Nature Climate Change 8, 141–145. https://doi.org/10.1038/s41558-017-0054-0.

Landschützer, P., Gruber, N., Bakker, D.C.E., Stemmler, I., Six, K.D., 2018. Strengthening seasonal marine CO_2 variations due to increasing atmospheric CO_2. Nature Climate Change 8, 146–150. https://doi.org/10.1038/s41558-017-0057-x.

Le Quéré, C., Andrew, R.M., Friedlingstein, P., Sitch, S., Hauck, J., Pongratz, J., Pickers, P.A., Korsbakken, J.I., Peters, G.P., Canadell, J.G., Arneth, A., Arora, V.K., Barbero, L., Bastos, A., Bopp, L., Chevallier, F., Chini, L.P., Ciais, P., Doney, S.C., Gkritzalis, T., Goll, D.S., Harris, I., Haverd, V., Hoffman, F.M., Hoppema, M., Houghton, R.A., Hurtt, G., Ilyina, T., Jain, A.K., Johannessen, T., Jones, C.D., Kato, E., Keeling, R.F., Goldewijk, K.K., Landschützer, P., Lefèvre, N., Lienert, S., Liu, Z., Lombardozzi, D., Metzl, N., Munro, D.R., Ono, T., Patra, P., Peregon, A., Peters, W., Peylin, P., Pfeil, B., Pierrot, D., Poulter, B., Rehder, G., Resplandy, L., Robertson, E., Rocher, M., Rödenbeck, C., Schuster, U., Schwinger, J., Séférian, R., Skjelvan, I., Steinhoff, T., Sutton, A., Tans, P.P., Tian, H., Tilbrook, B., Tubiello, F.N., 2018. Global Carbon Budget 2018. Earth System Science Data 10, 2141–2194.

Letscher, R.T., Primeau, F., Moore, J.K., 2016. Nutrient budgets in the subtropical ocean gyres dominated by lateral transport. Nature Geoscience 9, 815. https://doi.org/10.1038/ngeo2812.

Levitus, S., 1982. Climatological Atlas of the World Ocean. Eos Trans. AGU 13, 173. https://doi.org/10.1029/EO064i049p00962-02.

Lewis, E., Wallace, D.W.R., 1998. Program Developed for CO_2 System Calculations [WWW Document]. ORNL/CDIAC-105, Carbon Dioxide Information Analysis Center, Oak

Ridge National Laboratory. URL https://salish-sea.pnnl.gov/media/ORNL-CDIAC-105.pdf (accessed 5.23.19).

Lueker, T.J., Dickson, A.G., Keeling, C.D., 2000. Ocean pCO_2 calculated from dissolved inorganic carbon, alkalinity, and equations for K1 and K2: validation based on laboratory measurements of CO_2 in gas and seawater at equilibrium. Marine Chemistry 105–119.

Lueker, T.J., Keeling, C.D., Guenther, P.R., Wahlen, M., 1998. Inorganic carbon variations in surface ocean water near Bermuda (SIO Technical Report). UC San Diego: Scripps Institution of Oceanography.

Mantua, N., Hare, S.R., Zhang, Y., Wallace, J.M., Francis, R.C., 1997. A Pacific Interdecadal Climate Oscillation with Impacts on Salmon Production. Bulletin of the American Meteorological Society 78, 1069–1080.

Marchal, O., Monfray, P., Bates, N.R., 1996. Spring-summer imbalance of dissolved inorganic carbon in the mixed layer of the north-western Sargasso Sea. Tellus B: Chemical and Physical Meteorology 48, 115–134. https://doi.org/10.3402/tellusb.v48i1.15831.

McDougall, T.J., Barker, P.M., 2011. Getting started with TEOS-10 and the Gibbs Seawater (GSW) Oceanographic Toolbox. SCOR/IAPSO WG127, p. 28pp.

McKinley, G.A., Takahashi, T., Buitenhuis, E., Chai, F., Christian, J.R., Doney, S.C., Jiang, M.-S., Lindsay, K., Moore, J.K., Le Quéré, C., Lima, I., Murtugudde, R., Shi, L., Wetzel, P., 2006. North Pacific carbon cycle response to climate variability on seasonal to decadal timescales. J. Geophys. Res. 111, C07S06. https://doi.org/10.1029/2005JC003173.

McNeil, B.I., Matear, R.J., Tilbrook, B., 2001. Does carbon 13 track anthropogenic CO_2 in the Southern Ocean?. Global Biogeochemical Cycles 15, 597–613. https://doi.org/10.1029/2000GB001352.

Michaels, A.F., Knap, A.H., 1996. Overview of the U.S. JGOFS Bermuda Atlantic Time-series Study and the Hydrostation S program. Deep Sea Research Part II: Topical Studies in Oceanography 43, 157–198. https://doi.org/10.1016/0967-0645(96)00004-5.

Newman, M., Alexander, M.A., Ault, T.R., Cobb, K.M., Deser, C., Di Lorenzo, E., Mantua, N.J., Miller, A.J., Minobe, S., Nakamura, H., Schneider, N., Vimont, D.J., Phillips, A.S., Scott, J.D., Smith, C.A., 2016. The Pacific Decadal Oscillation, Revisited. Journal of Climate 29, 4399–4427. https://doi.org/10.1175/JCLI-D-15-0508.1.

Quay, P., Sonnerup, R., Munro, D., Sweeney, C., 2017. Anthropogenic CO_2 accumulation and uptake rates in the Pacific Ocean based on changes in the 13C/12C of dissolved inorganic carbon. Global Biogeochemical Cycles 2016GB005460. https://doi.org/10.1002/2016GB005460.

Quay, P., Sonnerup, R., Westby, T., Stutsman, J., McNichol, A., 2003. Changes in the $^{13}C/^{12}C$ of dissolved inorganic carbon in the ocean as a tracer of anthropogenic CO2 uptake. Global Biogeochemical Cycles 17, 1004. https://doi.org/10.1029/2001GB001817.

Quay, P., Stutsman, J., 2003. Surface layer carbon budget for the subtropical N. Pacific: constraints at station ALOHA. Deep Sea Research Part I: Oceanographic Research Papers 50, 1045–1061. https://doi.org/10.1016/S0967-0637(03)00116-X.

Sabine, C.L., Tanhua, T., 2010. Estimation of Anthropogenic CO_2 Inventories in the Ocean. Annual Review of Marine Science 2, 175–198. https://doi.org/10.1146/annurev-marine-120308-080947.

Sarmiento, J.L., Gruber, N., 2006. Ocean biogeochemical dynamics. Princeton University Press, Princeton.

Sarmiento, J.L., Le Quéré, C., 1996. Oceanic carbon dioxide uptake in a model of century-scale global warming. Science 274, 1346–1350. https://doi.org/10.1126/science.274.5291.1346

Siegenthaler, U., Sarmiento, J.L., 1993. Atmospheric carbon dioxide and the ocean. Nature 365, 119–125. https://doi.org/10.1038/365119a0.

Sonnerup, R.E., Quay, P.D., McNichol, A.P., Bullister, J.L., Westby, T.A., Anderson, H.L., 1999. Reconstructing the oceanic ^{13}C Suess Effect. Global Biogeochemical Cycles 13, 857–872. https://doi.org/10.1029/1999GB900027.

Sutton, A.J., Wanninkhof, R., Sabine, C.L., Feely, R.A., Cronin, M.F., Weller, R.A., 2017. Variability and trends in surface seawater pCO_2 and CO_2 flux in the Pacific Ocean: Pacific Ocean CO2 Flux Trends. Geophysical Research Letters 44, 5627–5636. https://doi.org/10.1002/2017GL073814.

Tagliabue, A., Bopp, L., 2008. Towards understanding global variability in ocean carbon-13: VARIABILITY IN OCEAN CARBON-13. Global Biogeochemical Cycles 22. https://doi.org/10.1029/2007GB003037.

Tanaka, T., Watanabe, Y.W., Watanabe, S., Noriki, S., Tsurushima, N., Nojiri, Y., 2003. Oceanic Suess effect of $\delta^{13}C$ in subpolar region: The North Pacific. Geophysical Research Letters 30. https://doi.org/10.1029/2003GL018503.

Tans, P.P., Berry, J.A., Keeling, R.F., 1993. Oceanic $^{13}C/^{12}C$ observations: A new window on ocean CO_2 uptake. Global Biogeochemical Cycles 7, 353–368. https://doi.org/10.1029/93GB00053.

Tans, P.P., Fung, I.Y., Takahashi, T., 1990. Observational constraints on the global atmospheric CO_2 budget. Science 247, 1431–1438. https://doi.org/10.1126/science.247.4949.1431.

Uppström, L.R., 1974. The boron/chlorinity ratio of deep-sea water from the Pacific Ocean. Deep-Sea Research, Instruments and Methods 21, 161–162.

van Heuven, S., Pierrot, D., Rae, J.W.B., Lewis, E., Wallace, D.W.R., 2011. MATLAB Program Developed for CO_2 System Calculations.

Watanabe, Y.W., Chiba, T., Tanaka, T., 2011. Recent change in the oceanic uptake rate of anthropogenic carbon in the North Pacific subpolar region determined by using a carbon-13 time series. Journal of Geophysical Research 116. https://doi.org/10.1029/2010 JC006199.

Winn, C.D., Li, Y.-H., Mackenzie, F.T., Karl, D.M., 1998. Rising surface ocean dissolved inorganic carbon at the Hawaii Ocean Time-series site. Marine Chemistry 60, 33–47. https://doi.org/10.1016/S0304-4203(97)00085-6.

Winn, C.D., Mackenzie, F.T., Carrillo, C.J., Sabine, C.L., Karl, D.M., 1994. Air-sea carbon dioxide exchange in the North Pacific Subtropical Gyre: Implications for the Global Carbon Budget. Global Biogeochemical Cycles 8, 157–163. https://doi.org/10.1029/94GB00387.

Table 3.1: Summary of rates of change for δ^{13}C-DIC, sDIC, sALK, pCO_2, SST, Salinity, and MLD for S-BATS and HOT Station ALOHA. Rates (shown in bold) were calculated using least squares linear regression on seasonally detrended data. Long-term trends for δ^{13}C-DIC and sDIC at minimum temperature values shown in bottom rows. 95% confidence intervals are reported in parentheses.

Parameter	Units	S-BATS 1983-2000	S-BATS 2001-2017	S-BATS 1983-2017	HOT 1989-2000	HOT 2001-2016	HOT 1989-2016
δ^{13}C-DIC	‰ yr^{-1}	**-0.0238**	**-0.0296**	**-0.0264**	**-0.0274**	**-0.0231**	**-0.0259**
		(-0.0249, -0.0228)	(-0.0306, -0.0286)	(-0.0268, -0.0260)	(-0.0295, -0.0253)	(-0.0245, -0.0217)	(-0.0265, -0.0252)
$\delta^{13}C_{atm}$	‰ yr^{-1}	**-0.0238**	**-0.0282**	**-0.0257**	**-0.0236**	**-0.0278**	**-0.0255**
		(-0.0255, -0.0221)	(-0.0298, -0.0265)	(-0.0263, -0.0251)	(-0.0259, -0.0213)	(-0.0293, -0.0264)	(-0.0261, -0.0248)
sDIC	µmol kg^{-1} yr^{-1}	**+0.62**	**+1.32**	**+1.07**	**+1.30**	**+1.72**	**+1.21**
		(+0.51, +0.74)	(+1.20, +1.45)	(+1.02, +1.12)	(+1.09, +1.51)	(+1.52, +1.93)	(+1.12, +1.30)
sALK	µmol kg^{-1} yr^{-1}	**-0.04**	**+0.29**	**+0.15**	**-0.27**	**+0.60**	**+0.22**
		(-0.12, +0.04)	(+0.22, +0.37)	(+0.12, +0.18)	(-0.44, -0.10)	(+0.49, +0.71)	(+0.16, +0.27)
pCO_2	µatm yr^{-1}	**+1.67**	**+2.01**	**+1.88**	**+2.46**	**+2.32**	**+1.99**
		(+1.45, +1.89)	(+1.72, +2.30)	(+1.79, +1.98)	(+2.11, +2.81)	(+1.98, +2.66)	(+1.85, +2.13)
$pCO_{2\text{-atm}}$	µatm yr^{-1}	**+1.48**	**+2.20**	**+1.82**	**+1.54**	**+2.13**	**+1.90**
		(+1.45, +1.51)	(+2.17, +2.24)	(+1.81, +1.85)	(+1.50, +1.58)	(+2.11, +2.15)	(+1.88, +1.92)
SST	°C yr^{-1}	**+0.04**	**+0.01**	**+0.02**	**-0.03**	**+0.0002**	**+0.01**
		(+0.02, +0.05)	(-0.01, +0.03)	(+0.01, +0.03)	(-0.05, 0.0)	(-0.02, +0.02)	(0, +0.02)
Salinity	psu yr^{-1}	**+0.009**	**-0.005**	**+0.001**	**+0.029**	**+0.005**	**+0.010**
		(+0.006, +0.011)	(-0.007, -0.001)	(0.0, +0.003)	(+0.018, +0.039)	(-0.001, 0.010)	(+0.008, +0.013)
MLD	m yr^{-1}	**+0.68**	**+0.24**	**+0.11**	**+1.35**	**+0.04**	**+0.45**
		(-0.29, +1.64)	(-0.42, +0.90)	(-0.20, +0.41)	(+0.38, +2.33)	(-0.61, +0.69)	(+0.17, +0.74)
Trends at annual minimum temperature							
δ^{13}C-DIC	‰ yr^{-1}			**-0.0257**			**-0.0261**
				(-0.0273, -0.0240)			(-0.0287, -0.0234)
sDIC	µmol kg^{-1} yr^{-1}			**+1.04**			**+1.19**
				(+0.84, +1.24)			(+0.91, +1.48)

Table 3.2: Mean seasonal amplitude and standard deviation for S-BATS and HOT.

Parameter	Units	S-BATS Amplitude	Max Month	Min Month	HOT Amplitude	Max Month	Min Month
δ^{13}C-DIC	‰	0.159 ± 0.039	*Oct*	*Mar*	0.083 ± 0.051	*Oct*	*Feb*
sDIC	µmol kg^{-1}	25.09 ± 4.8	*Mar*	*Sep*	11.7 ± 6.2	*Apr*	*Oct*
pCO_2	µatm	66.5 ± 8.2	*Aug*	*Mar*	20.9 ± 6.9	*Sep*	*Mar*
SST	ºC	7.3 ± 0.7	*Aug*	*Mar*	2.7 ± 0.5	*Sep*	*Mar*
MLD	m	110 ± 39	*Feb*	*Jun*	27 ± 21	*Jan*	*Jun*

Table 3.3: Correlation* for sDIC, δ^{13}C-DIC, and SST seasonal amplitudes.

S-BATS Seasonal Amplitude Correlation

Parameter	Units	δ^{13}C-DIC	sDIC	pCO_2	SST	MLD
δ^{13}C-DIC	‰	1	-	-	-	-
sDIC	µmol kg^{-1}	**+0.71** *(97%)*	1	-	-	-
pCO_2	µatm	-0.23 *(87%)*	-0.10 *(69%)*	1	-	-
SST	ºC	**+0.54** *(96%)*	**+0.69** *(>99%)*	**+0.38** *(95%)*	1	-
MLD	m	+0.32 *(85%)*	**+0.41** *(96%)*	+0.16 *(77%)*	**+0.49** *(95%)*	1

HOT Seasonal Amplitude Correlation

		δ^{13}C-DIC	sDIC	pCO_2	SST	MLD
δ^{13}C-DIC	‰	1	-	-	-	-
sDIC	µmol kg^{-1}	**+0.73** *(97%)*	1	-	-	-
pCO_2	µatm	**-0.64** *(>99%)*	**-0.59** *(>99%)*	1	-	-
SST	ºC	+0.34 *(91%)*	**+0.53** *(96%)*	+0.07 *(61%)*	1	-
MLD	m	+0.21 *(83%)*	+0.26 *(88%)*	-0.19 *(83%)*	-0.28 *(92%)*	1

*Values in parentheses give likelihood (in percentage) that correlations are not random, determined using an Ebisuzaki (1997) significance test.

Table 3.4: Correlation coefficients for interannual variability of residual anomalies*–determined from spline fit in Figures 3.10 and 3.11 (subsampled at monthly intervals). NAO correlations use mean winter months (DJFM) for each variable; while PDO, NINO3.4, and NPGO correlations use monthly data.

S-BATS Correlation							
	δ^{13}C-DIC	sDIC	sALK	pCO_2	SST	Sal	MLD
δ^{13}C-DIC	1	-	-	-	-	-	-
sDIC	**-0.59**	1	-	-	-	-	-
	(>99%)						
sALK	+0.05	+0.12	1	-	-	-	-
	(60%)	*(75%)*					
pCO_2	-0.18	+0.01	**-0.61**	1	-	-	-
	(88%)	*(53%)*	*(>99%)*				
SST	**+0.37**	**-0.79**	-0.04	**+0.36**	1	-	-
	(97%)	*(>99%)*	*(59%)*	*(>99%)*			
Sal	+0.11	+0.004	-0.21	+0.14	+0.18	1	-
	(80%)	*(47%)*	*(91%)*	*(80%)*	*(90%)*		
MLD	-0.12	**+0.28**	+0.04	-0.09	**-0.28**	+0.10	1
	(82%)	*(96%)*	*(62%)*	*(75%)*	*(97%)*	*(70%)*	
NAO_{DJFM}	+0.15	**-0.57**	+0.20	-0.08	**+0.52**	-0.09	**-0.29**
	(80%)	*(>99%)*	*(86%)*	*(67%)*	*(97%)*	*(73%)*	*(95%)*
HOT Station ALOHA Correlation							
	δ^{13}C-DIC	sDIC	sALK	pCO_2	SST	Sal	MLD
δ^{13}C-DIC	1	-	-	-	-	-	-
sDIC	-0.20	1	-	-	-	-	-
	(86%)						
sALK	-0.02	**+0.49**	1	-	-	-	-
	(51%)	*(95%)*					
pCO_2	-0.09	**+0.54**	-0.10	1	-	-	-
	(71%)	*(>99%)*	*(64%)*				
SST	+0.10	**-0.64**	-0.21	+0.11	1	-	-
	(70%)	*(>99%)*	*(87%)*	*(69%)*			
Sal	+0.27	+0.29	-0.07	**+0.37**	**-0.36**	1	-
	(86%)	*(85%)*	*(66%)*	*(95%)*	*(96%)*		
MLD	-0.12	**+0.52**	+0.13	+0.09	**-0.64**	**+0.29**	1
	(77%)	*(97%)*	*(72%)*	*(67%)*	*(>99%)*	*(96%)*	
PDO	+0.15	**-0.49**	-0.09	**-0.27**	**+0.39**	-0.14	**-0.30**
	(75%)	*(>99%)*	*(73%)*	*(97%)*	*(96%)*	*(77%)*	*(97%)*
NINO3.4	+0.17	**-0.33**	-0.05	-0.22	+0.21	-0.04	**-0.32**
	(83%)	*(96%)*	*(64%)*	*(92%)*	*(84%)*	*(58%)*	*(98%)*
NPGO	+0.08	+0.34	-0.01	+0.28	-0.26	+0.29	**+0.41**
	(66%)	*(92%)*	*(54%)*	*(91%)*	*(90%)*	*(85%)*	*(>99%)*

*Values in parentheses give likelihood (in percentage) that correlations are not random, determined using an Ebisuzaki (1997) significance test.

3.8: FIGURES

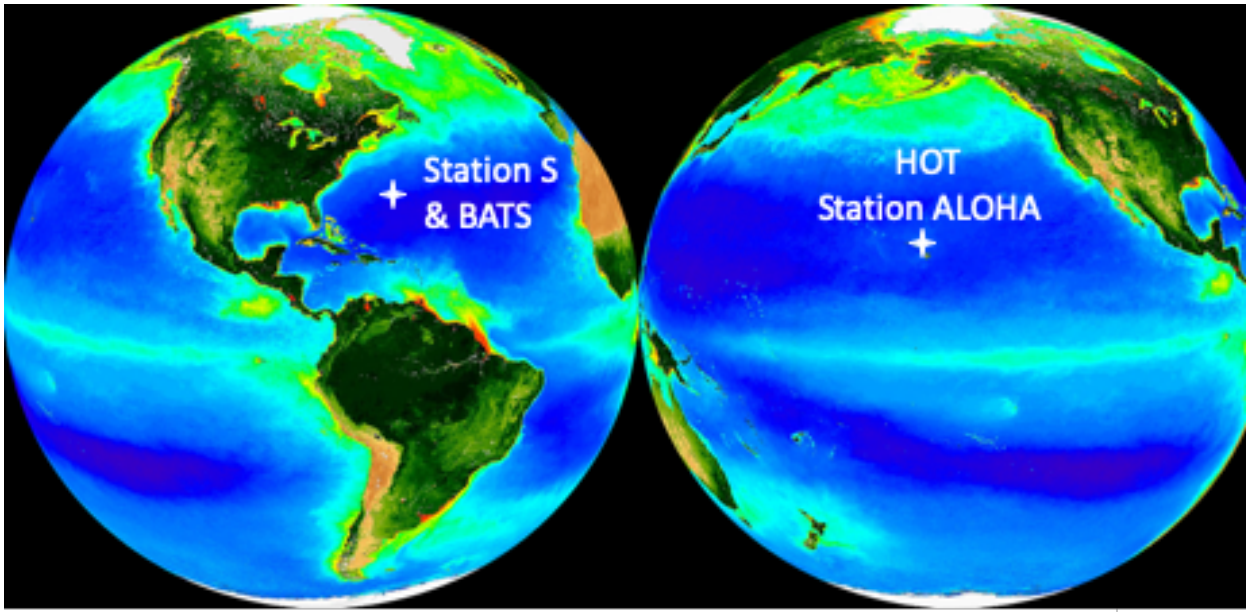

Figure 3.1: Map of time-series station locations. Station S and BATS are located 26 km and 80 km southeast of Bermuda in the North Atlantic subtropical gyre respectively. HOT Station ALOHA is located ~100 km north of ‘Oahu, Hawaii in the North Pacific subtropical gyre. (Map source: SeaWiFS showing satellite chlorophyll data).

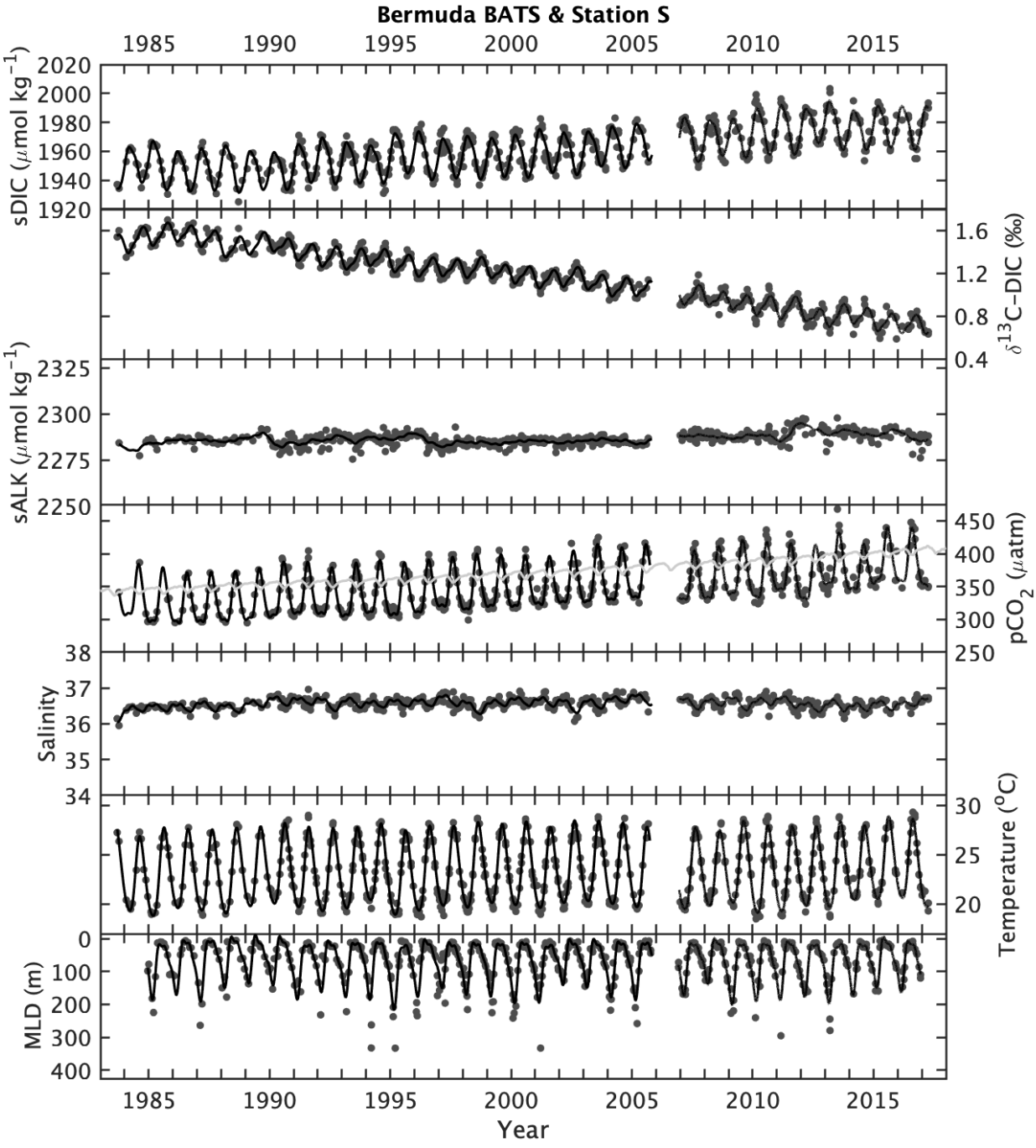

Figure 3.2: S-BATS (10m) time-series records of sDIC, δ^{13}C-DIC, ALK, pCO_2, Salinity, SST, and Mixed Layer Depth (MLD). Plots show the time-series data (dark gray filled circles) with the fit (solid black line) which consists of a quadratic in combination with 4-, 6-, and 12-month harmonics plus a cubic spline function. The middle pCO_2 panel includes atmospheric data (solid light gray line) from the Scripps CO_2 program La Jolla station. The gap evident at Station S and BATS between 2005 and 2006 is due to the failure of a sample storage refrigerator at SIO.

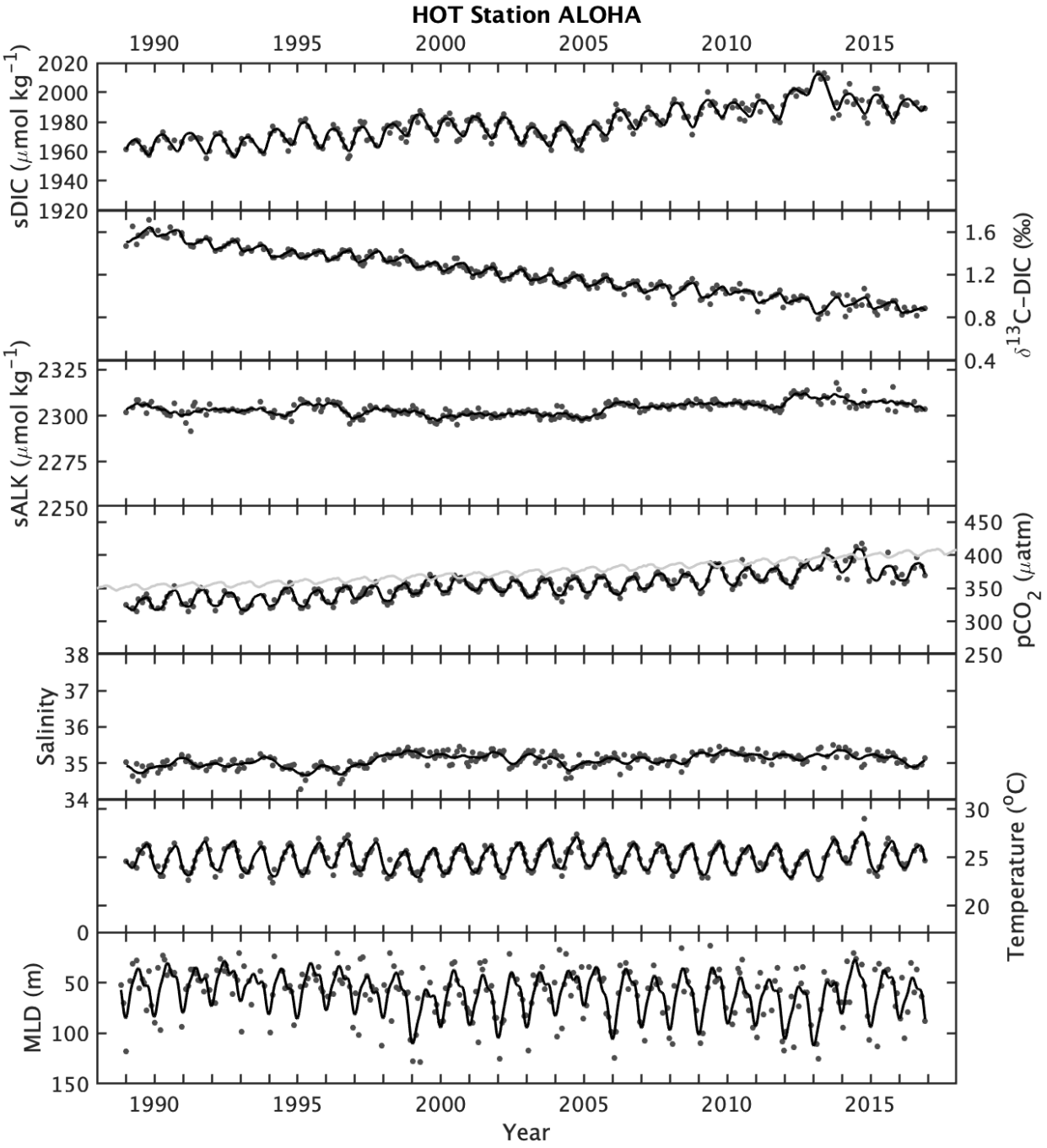

Figure 3.3: HOT Station ALOHA (5m) time-series records of sDIC, δ^{13}C-DIC, ALK, pCO_2, Salinity, SST, and Mixed Layer Depth (MLD). Plots show the time-series data (dark gray circles) with the fit (solid black line) which consists of a quadratic in combination with 4-, 6-, and 12-month harmonics plus a cubic spline function. The middle pCO_2 panel includes atmospheric data (solid light gray line) from the Scripps CO_2 program Kumukahi station.

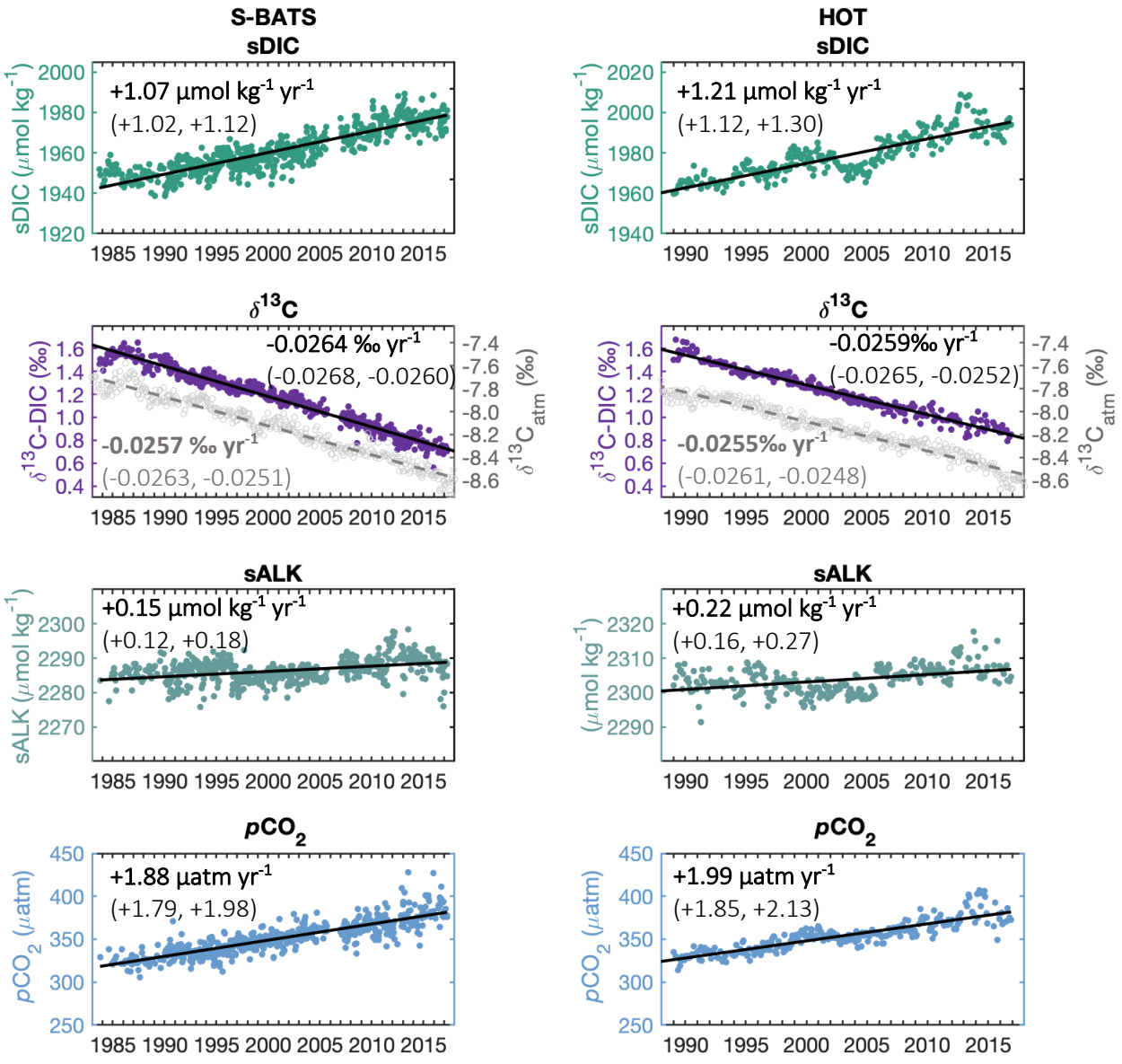

Figure 3.4: Deseasonalized sDIC, δ^{13}C-DIC (purple), $\delta^{13}C_{atm}$ (light gray open circles), sALK, and seawater pCO_2 with least-squares linear regression fit (solid lines for seawater variables, dashed line for atmospheric $\delta^{13}C_{atm}$). Linear trends include 95% confidence intervals in parentheses. Trends for all variables are summarized in Table 1.

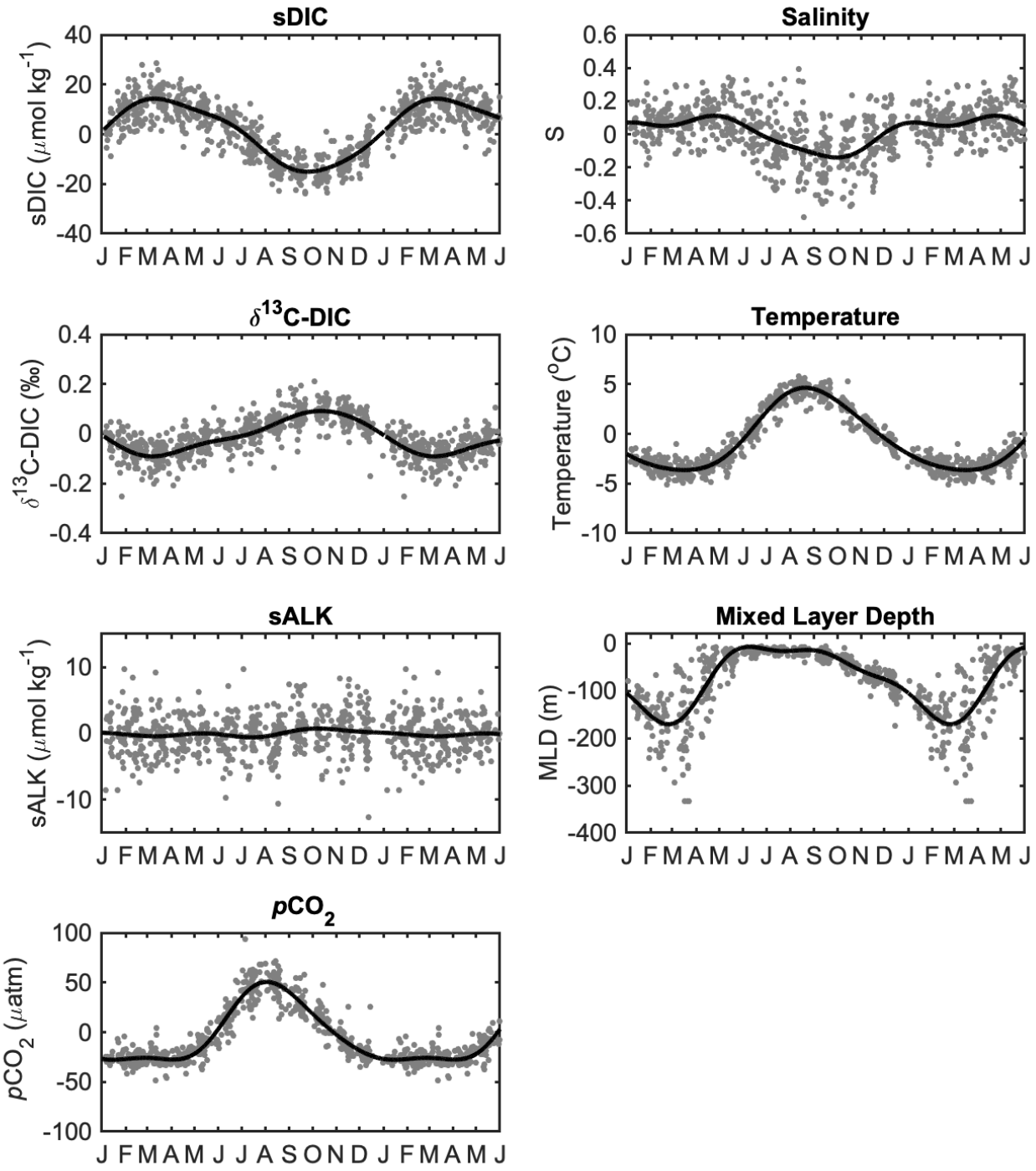

Figure 3.5: S-BATS data collapsed into a single year to show the seasonal cycle. The black line represents the BATS + Station S mean seasonal cycle, calculated using 4-, 6-, and 12-month harmonics.

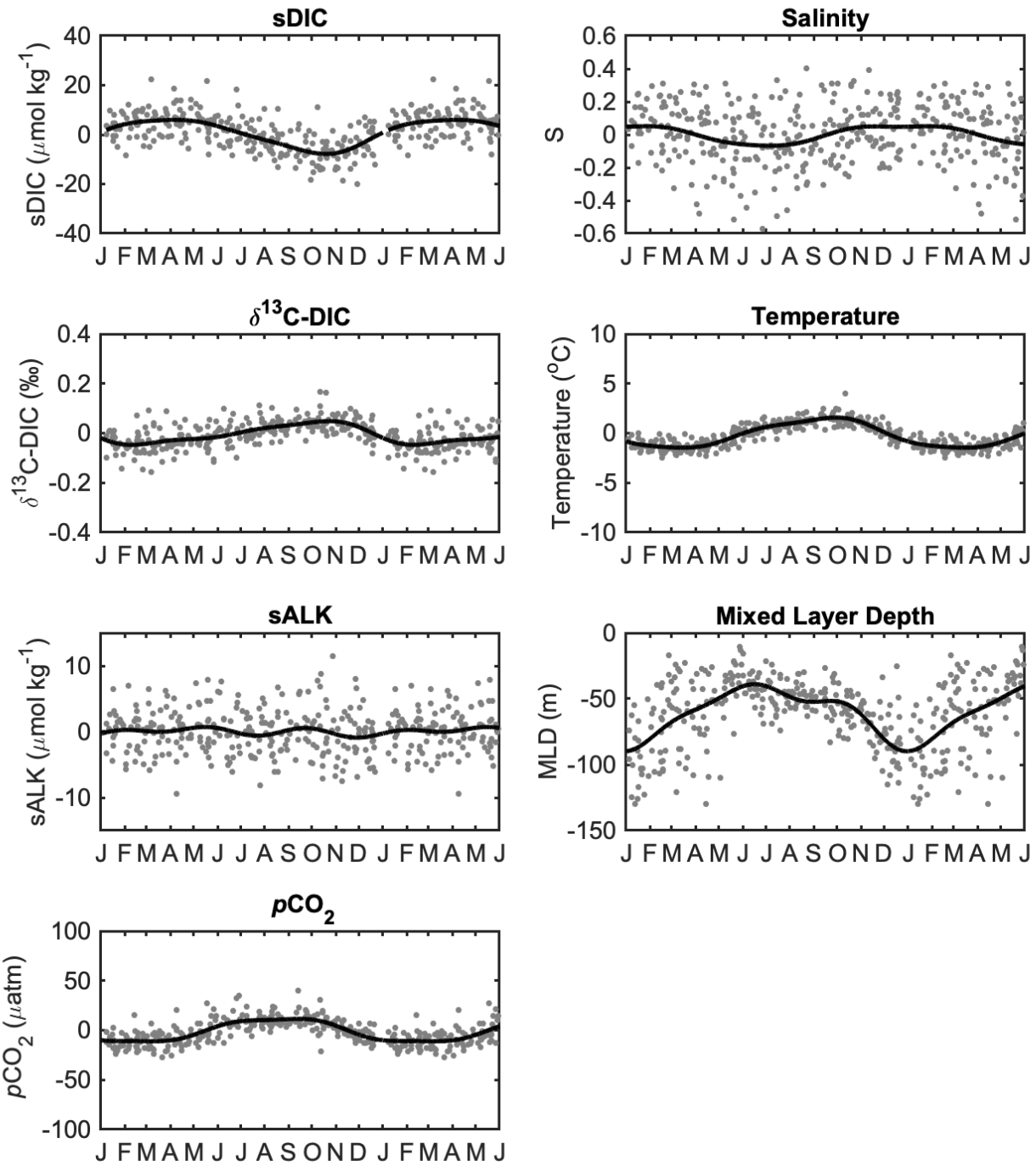

Figure 3.6: HOT Station ALOHA data collapsed into a single year to show the seasonal cycle. The black line represents the BATS + Station S mean seasonal cycle. The mean seasonal cycle (solid line) was calculated using 4-, 6-, and 12-month harmonics with the long-term trend removed.

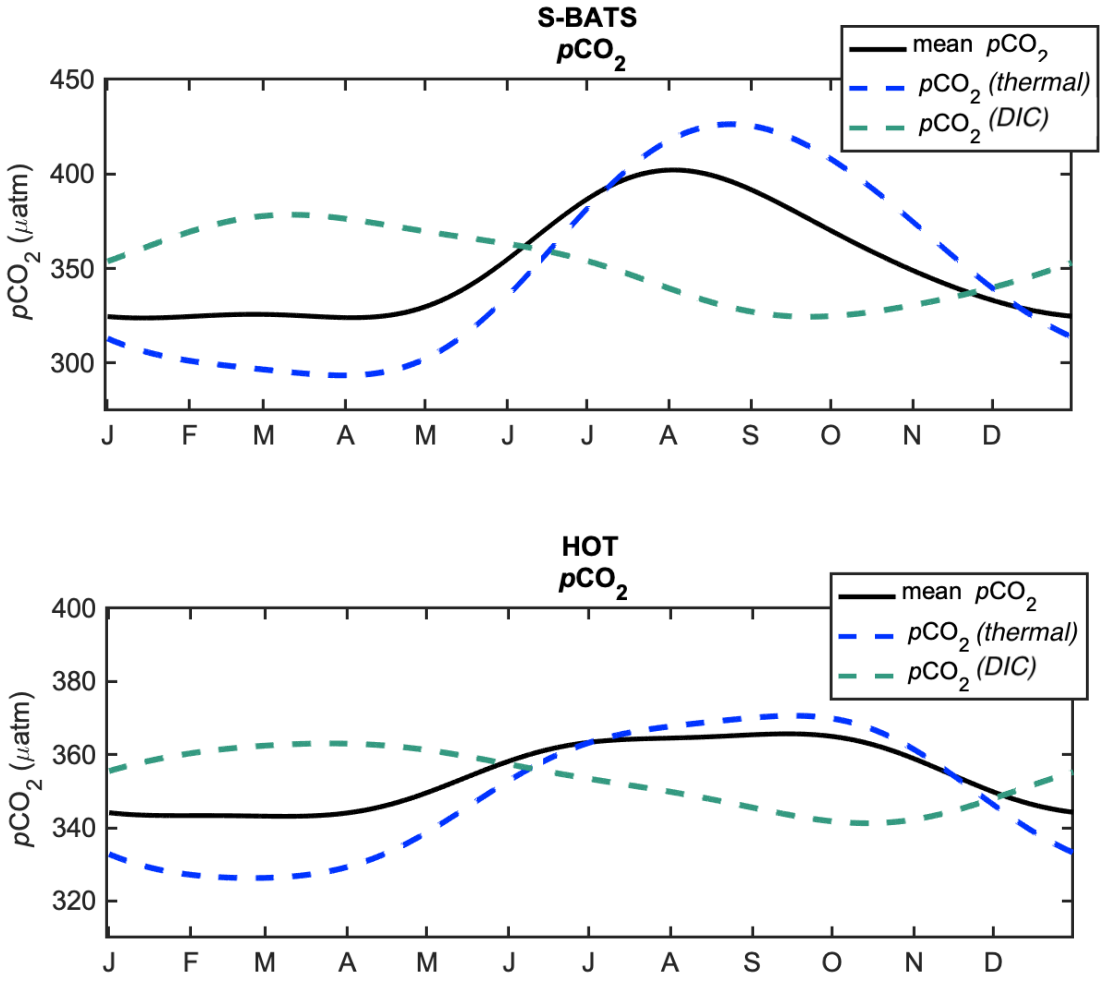

Figure 3.7: S-BATS (top) and HOT (bottom) mean seasonal cycle of pCO_2 (black, solid line) with the relative contributions to this seasonal cycle from SST (blue, dashed line) and sDIC (teal, dashed line) variations. The thermal component (blue) shows expected pCO2 changes when DIC is held constant at a mean of 1962 µmol kg^{-1} (S-BATS) and 1978 µmol kg^{-1} (HOT)). The sDIC contribution (teal) shows expected pCO_2 changes from DIC when SST is held constant at a mean value of 23.5ºC (BATS) and 24.8ºC (HOT).

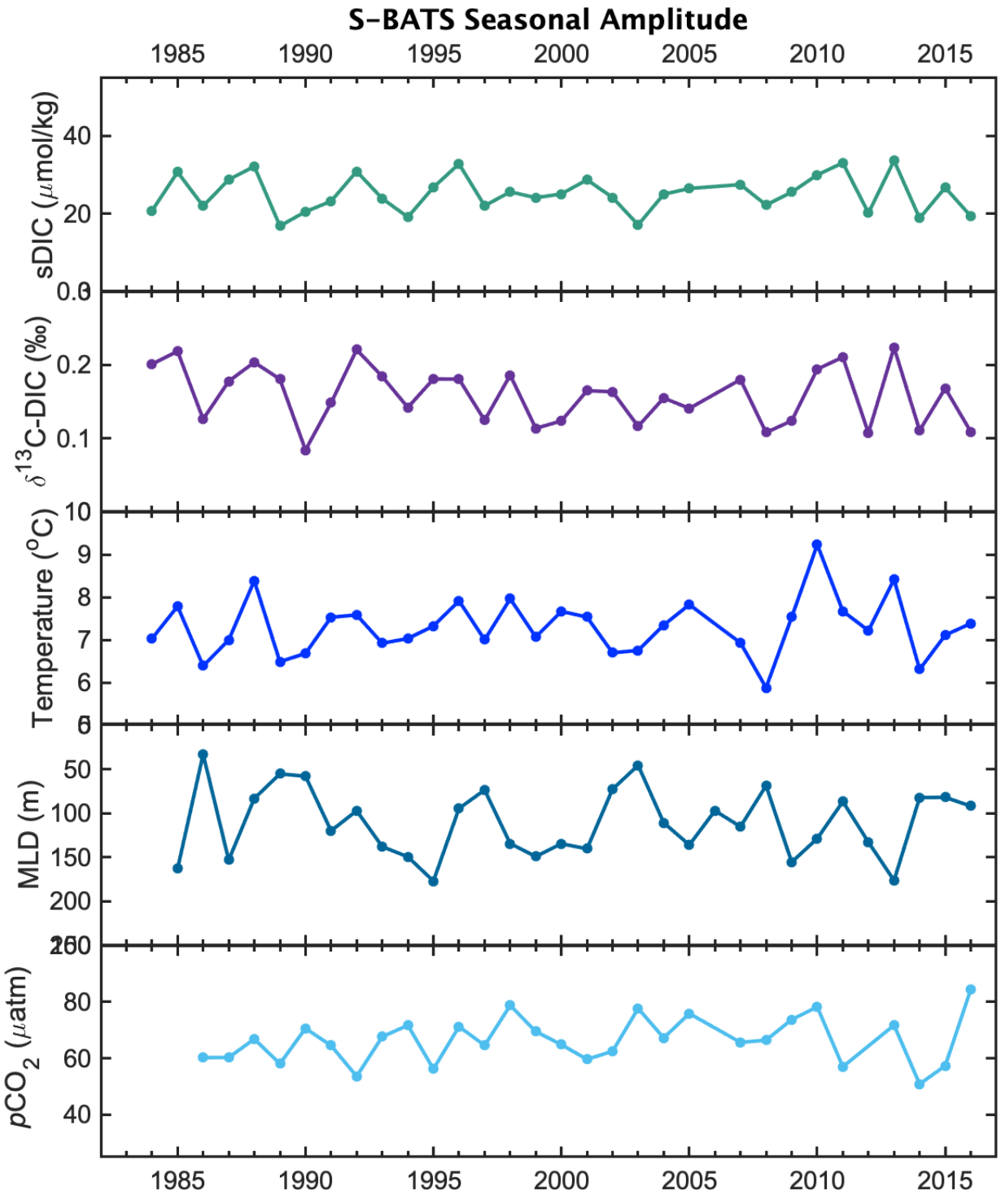

Figure 3.8: S-BATS annual seasonal amplitude for the time-series record for sDIC, δ^{13}C-DIC, SST, MLD, and pCO_2.

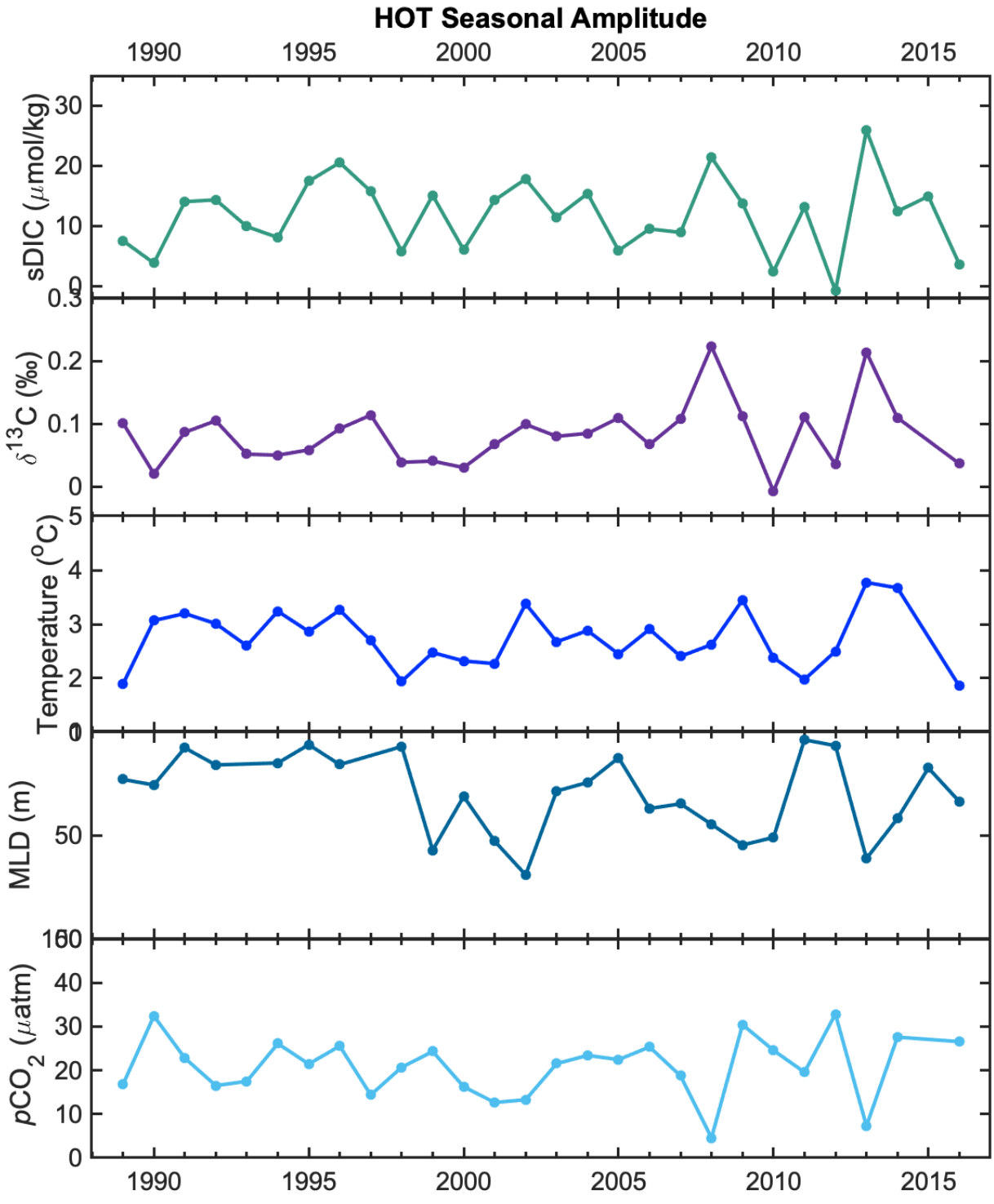

Figure 3.9: HOT annual seasonal amplitude over the time-series record for sDIC, δ^{13}C-DIC, SST, MLD, and pCO_2.

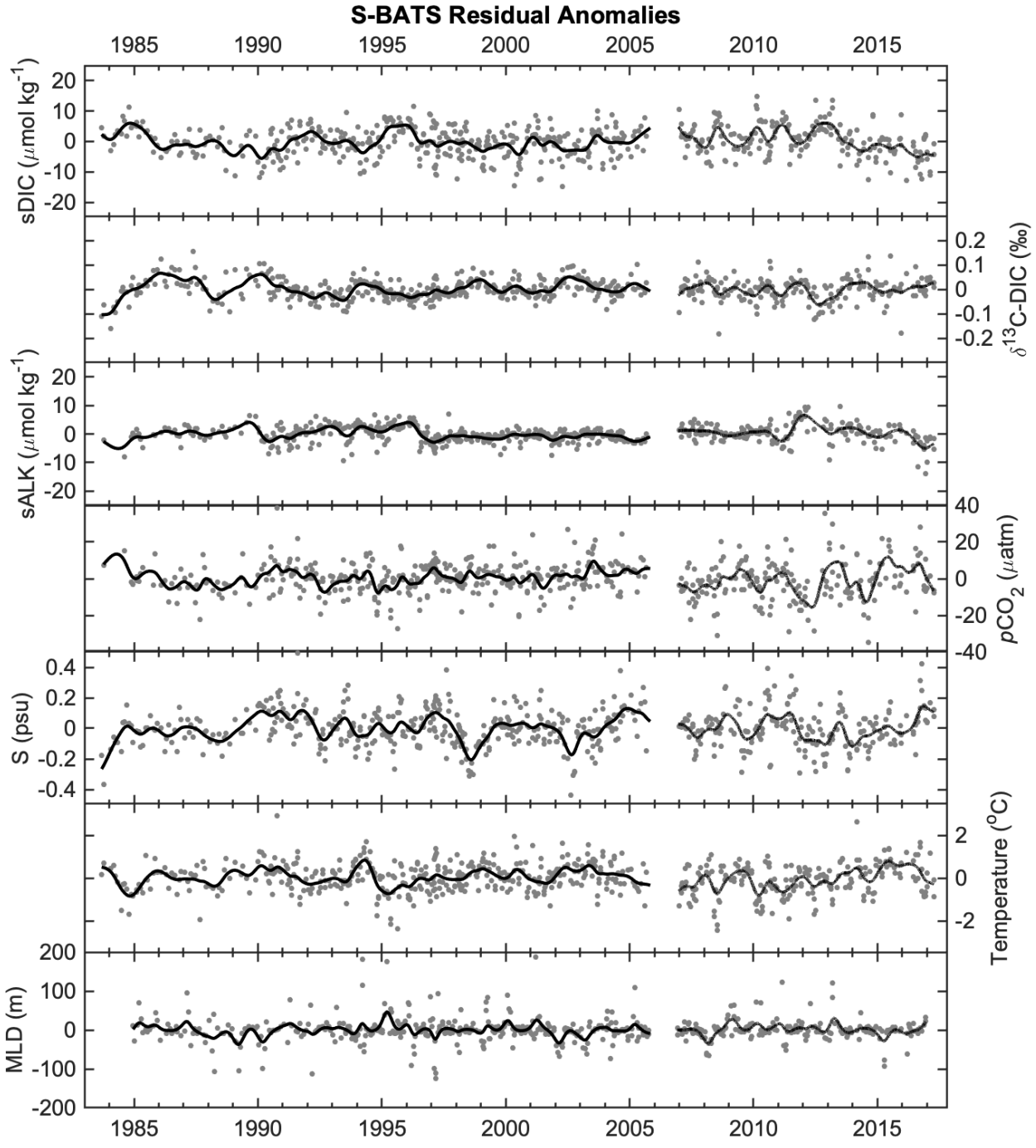

Figure 3.10: S-BATS residual anomalies, showing interannual variability remaining after removing the long-term trend and mean seasonal cycle.

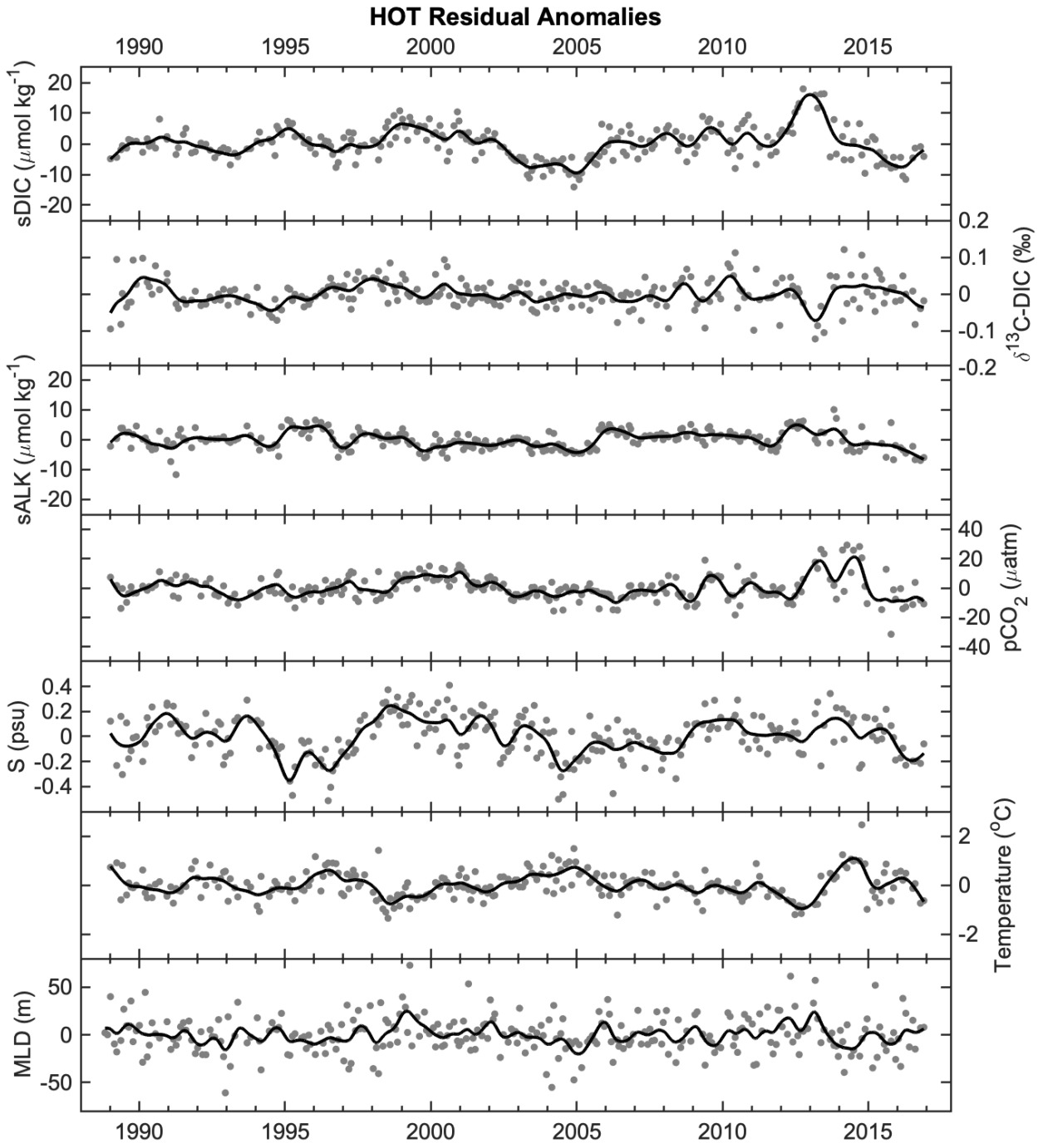

Figure 3.11: HOT residual anomalies, showing interannual variability remaining after removing the long-term trend and mean seasonal cycle.

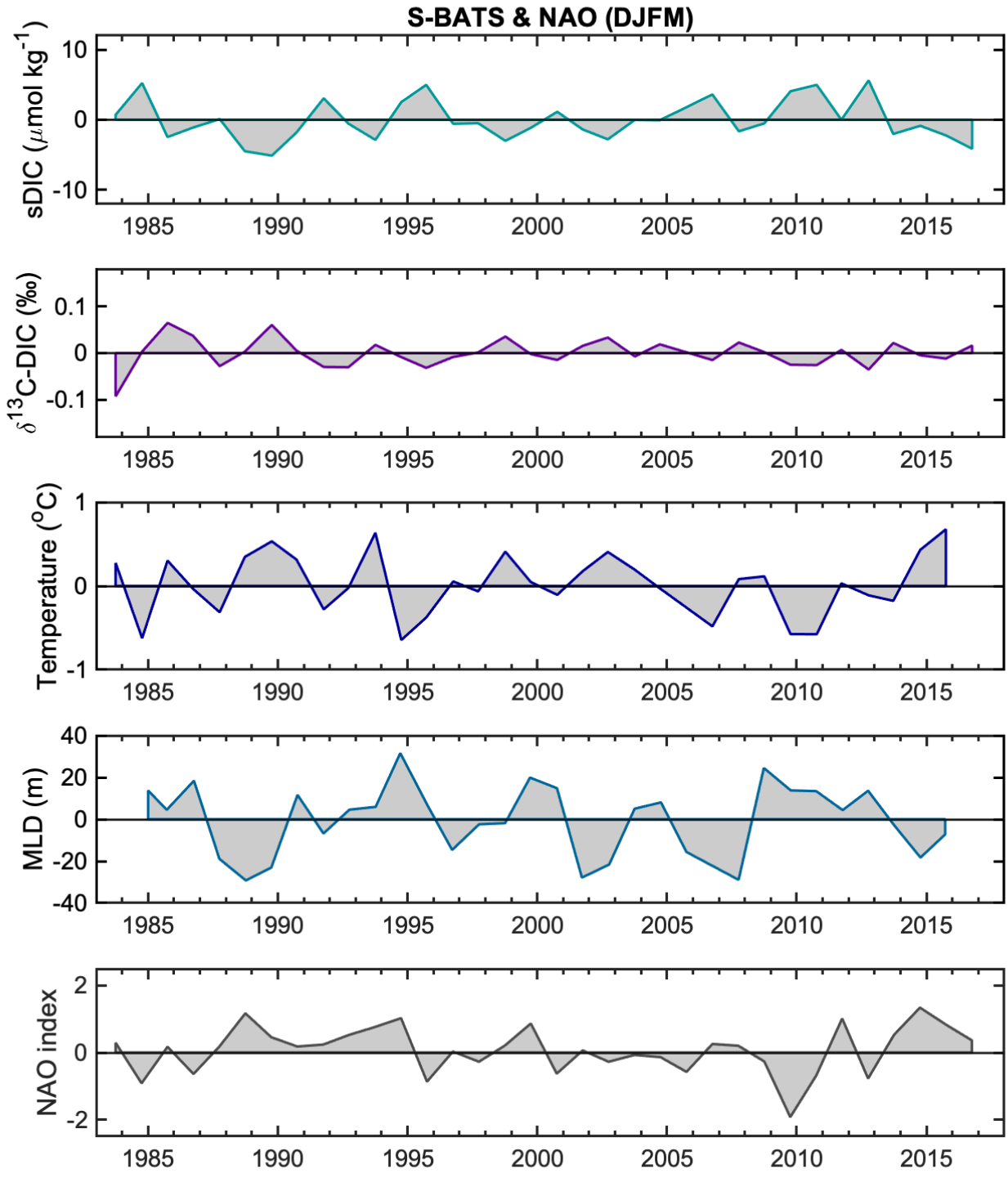

Figure 3.12: S-BATS Residual winter anomalies of sDIC, δ^{13}C-DIC, SST, and MLD with winter months of the NAO index. All values have been averaged over winter months DJFM (following Gruber et al. (2002)).

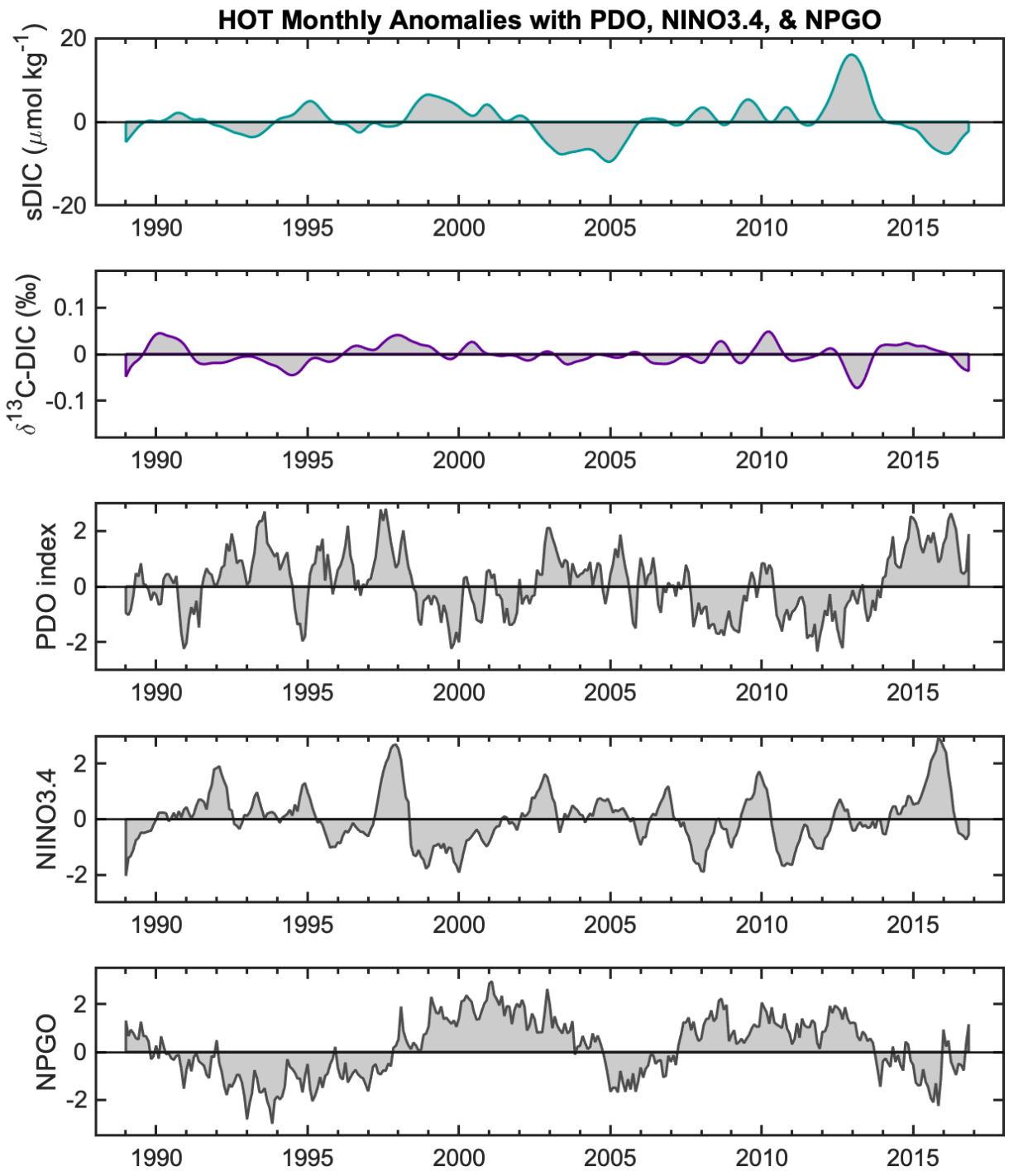

Figure 3.13: HOT residual monthly anomalies of sDIC and δ^{13}C-DIC with corresponding plots of monthly PDO, NINO3.4, and NPGO indices.

CHAPTER 4: UPPER OCEAN CARBON CYCLE VARIABILITY IN SUBTROPICAL GYRES

ABSTRACT

The ocean plays a critical role in the global carbon cycle, especially as atmospheric anthropogenic carbon emissions continue to accumulate. Net community production (NCP), defined as net primary production minus community respiration, is a fundamental part of the natural carbon cycle variability in the surface ocean. We use established time-series records of DIC and δ^{13}C-DIC and compare with a Community Earth System Model (CESM2) hindcast simulation which includes stable carbon isotopes in the modeled biogeochemistry. We first use the observations to evaluate the model at the time-series sites and then explore basin-scale relationships within the model, focusing on interannual variability and spatially coherent patterns within the subtropical gyres. The model has relatively low SST bias that is weakly negative to neutral across the North Atlantic subtropical gyre (< 0.4 °C) and North Pacific subtropical gyre (< 0.5 °C). We find that the model underestimates the interannual variability at S-BATS, capturing the variability to various degrees for δ^{13}C-DIC (49%) and sDIC (75%). In contrast, at HOT the model overestimates variability in both δ^{13}C-DIC (113%) and sDIC (158%). We compare relative changes in sDIC and δ^{13}C-DIC and find that they are well represented in the surface ocean near HOT and BATS. We also show that there are coherent patterns of variability between modeled δ^{13}C-DIC, sDIC, and NCP at BATS and the surrounding surface ocean variability in the North Atlantic subtropical gyre. HOT also exhibits coherent patterns of variability between modeled δ^{13}C-DIC, sDIC, and NCP and the surrounding surface ocean variability in the North Pacific subtropical gyre, although to a lesser extent. This is in part due the location of HOT on the node of the east-west pattern of variability dominant in the North

Pacific. We also illustrate that BATS interannual variability in sDIC, NCP, and δ^{13}C-DIC appears to be dominated by vertical mixing, while the variability at HOT is most likely dominated by water mass shifts and horizontal advection.

4.1 INTRODUCTION

The ocean plays a critical role in the global carbon cycle. According to recent estimates, approximately 24% of anthropogenic carbon emissions enter the ocean (Le Quéré et al., 2018), and it is important to understand the ocean's role in the carbon cycle and how that may be changing over time. There is substantial variability associated with the oceanic carbon cycle, including carbon uptake and export from the surface mixed layer (Bates, 2007; Brix et al., 2004; Gruber et al., 2002; Quay and Stutsman, 2003). Improving our understanding of the mechanisms driving variability in the upper ocean carbon cycle will help us to better understand natural variability as well as how ocean carbon uptake and storage may respond to climate change forcing (Sabine and Tanhua, 2010).

Net community production (NCP) is defined as net primary production minus community respiration (Williams, 1993) and resulting organic matter can be exported as sinking particles out of the surface mixed layer leading to long-term carbon storage in the deep ocean. Subtropical gyres encompass ~40% of the Earth's surface (Karl, 2002, 1999; McClain et al., 2004) and could be responsible for as much as 60% of global organic carbon export from the surface ocean (Quay and Stutsman, 2003). The North Pacific Subtropical Gyre (NPSG) alone covers ~$2x10^7$ km^2 between 15^{o}N and 35^{o}N (Karl, 1999). Subtropical gyres are characterized by anticyclonic circulation – convergent surface flow yielding net downwelling, with minimal vertical mixing. These are highly stratified, oligotrophic regions where nutrients are often below detectable limits in the surface ocean. While the rate of productivity is not as high as it is in other regions of the

ocean, the sheer size of the oligotrophic biome makes it a powerful contributor to global integrals of productivity.

NCP directly impacts dissolved inorganic carbon (DIC) concentrations and stable carbon isotopes of DIC (δ^{13}C-DIC) through photosynthesis and respiration. During photosynthesis, DIC is reduced and isotopic fractionation occurs, in which the lighter carbon isotope is used preferentially, and δ^{13}C-DIC is enriched (becomes more positive). In contrast, during respiration, DIC increases and as organic material with depleted (more negative) δ^{13}C values is remineralized, the δ^{13}C-DIC pool also becomes more negative. In this way, the seasonal cycle of DIC and δ^{13}C-DIC are negatively correlated, and a portion of their seasonal and interannual signals reflect the forcing of the seasonality and variability of NCP. Because of measurable signal of photosynthetic fractionation on the $^{13}C/^{12}C$ ratio of DIC, δ^{13}C-DIC can be used as a tracer to infer NCP.

Taking advantage of this relationship between NCP, DIC, and δ^{13}C-DIC, NCP has been estimated in previous studies which use a box model based on long-term time-series records of DIC and δ^{13}C-DIC in the surface mixed layer (Brix et al., 2004; Gruber et al., 2002, 1998; Keeling et al., 2004; Quay and Stutsman, 2003). These time-series are obtained from the Hawaii Ocean Time-series (HOT) Station ALOHA near Hawaii and the Bermuda Atlantic Time-series Study (BATS) and Station S near Bermuda. Time-series observations of DIC and δ^{13}C-DIC as well as estimates of NCP show that there is considerable interannual variability in these signals. In addition to impacts from photosynthesis and respiration, these records also show sensitivity to a combination of the physical forcing controlling air-sea gas exchange, vertical mixing and entrainment, as well as horizontal advection–all of which can impact the observed interannual variability.

Large-scale modes of climate variability (i.e. the North Atlantic Oscillation (NAO), the El Nino Southern Oscillation (ENSO), the Pacific Decadal Oscillation (PDO), and the North Pacific Gyre Oscillation (NPGO)) are often associated with spatially coherent patterns of sea surface temperature (SST) and wind speed anomalies, as well as changes in trade wind forcing and gyre circulation (Di Lorenzo et al., 2008; Hurrell et al., 2003; Karl, 1999; Newman et al., 2016). These forcing parameters directly impact many biogeochemically relevant processes, including air-sea gas exchange, vertical mixing and entrainment, and gyre circulation dynamics. The impacts of the forcing associated with these climate indices can be observed at HOT and BATS, where there is correlation between dominant modes of climate variability and the interannual variability of the carbon cycle (Bates, 2012; Brix et al., 2004; Doddridge and Marshall, 2018; Gruber et al., 2002; Kavanaugh et al., 2014; Palter et al., 2005; Sarmiento et al., 2004). An important question is whether similar links between carbon parameters (e.g. NCP, DIC, and δ^{13}C-DIC) and these modes of climate variability are found, not just at these stations, but throughout the subtropical gyres.

The NAO is directly related to shifts in the westerlies and therefore the mean wind speed and direction over the North Atlantic. NAO forcing helps to determine the strength of winter storms, especially in the western North Atlantic Subtropical Gyre. During periods of negative NAO, the region near Bermuda experiences stronger winter storms and wind speeds with negative anomalies in SST and a deepening of winter mixed layer depth (MLD). At BATS, these negative SST and positive MLD anomalies are well correlated with positive DIC anomalies and negative δ^{13}C-DIC anomalies resulting from entrainment of DIC and nutrient rich waters from below the mixed layer which are also depleted in δ^{13}C (Gruber et al., 2002; Chapter 3). In addition, NCP variability is negatively correlated with the NAO in which positive NCP

anomalies are observed during negative periods of the NAO due to the increased nutrient supply from this enhanced vertical mixing. These periods of strengthened winter mixing can then establish the magnitude of NCP, DIC, and δ^{13}C-DIC values observed in the mixed layer for the remainder of the year (Gruber et al., 2002; Lueker et al., 1998).

Using a box model approach with δ^{13}C-DIC and sDIC measurements from HOT in the North Pacific, Brix et al. (2004) show that interannual variability of upper ocean salinity normalized DIC (sDIC) at HOT is driven primarily by air-sea gas exchange, NCP variability, and lateral transport. However, only weak correlations were found between the time-series records and the PDO and ENSO, potentially resulting from the location of HOT which exists in a region centered between the east-west bimodal pattern of PDO forcing (Brix et al., 2004; Kavanaugh et al., 2018; McKinley et al., 2006; Yasunaka et al., 2014). Circulation shifts and climate patterns may adjust where that node is relative to HOT in a given year which plays an important role in water mass interactions and subsequent biogeochemical characteristics observed in the time-series data. This feature of the North Pacific and the HOT location suggests that the interannual variability observed here may not be widely representative of the subtropical gyre, and may be further complicated by regime shifts depending on whether HOT is further embedded in the eastern or western (or neutral) expression of the PDO (Kavanaugh et al., 2018). It also suggests that additional drivers of variability dominate NCP and δ^{13}C-DIC variability in the North Pacific subtropical gyre. It is also possible that the previously published record lengths were insufficient to fully capture the interdecadal climate modes present in the North Pacific, as illustrated by the higher correlation observed in the recently updated records (Brooks, Chapter 3).

Studies at these time-series locations have often extrapolated their estimates out to encompass the carbon cycle behavior across the North Atlantic or North Pacific subtropical gyre.

However, the station records have not always agreed well with satellite or transect measurements over the wider subtropical gyre areas either (Kavanaugh et al., 2018). While highly valuable, these time-series records are, understandably, limited both spatially and temporally. An important need is to quantify a real footprint of these stations, i.e. the domain over which carbon parameters correlate strongly with the variations at the stations themselves.

The time-series records of δ^{13}C-DIC and DIC at HOT and BATS quantify interannual and secular variability in the carbon cycle in the surface waters of the subtropical gyres. δ^{13}C-DIC provides constraints on NCP not provided by DIC alone (Gruber et al., 1998; Quay and Stutsman, 2003). Making use of the time-series records, we are in a unique position to be able to understand the impacts of climate variability and change on the upper ocean carbon cycle in subtropical gyres. To do this, it is critical to understand how the time-series stations fit into the broader geographic and dynamical context of the gyres and ocean basins where they are located. Using a Community Earth System Model (CESM) hindcast simulation which includes stable carbon isotopes in the modeled biogeochemistry, we use the observations to verify the model at the time-series sites and then explore basin-scale relationships within the model.

The primary goal of this chapter is to explore the mechanisms that drive carbon cycle variability in these oligotrophic regions by addressing the following questions:

1. What is the spatial structure and magnitude of sDIC, δ^{13}C-DIC, and NCP variability in surface waters within the subtropical gyres of the North Pacific and Atlantic?
2. What are the dominant controls of NCP, δ^{13}C-DIC, and sDIC variability in these gyres?
3. Over what spatial scales is the interannual variability in sDIC, δ^{13}C-DIC, and NCP at HOT and BATS correlated with the variability in surrounding waters?

4.2 METHODS

4.2.1 Model Data - CESM

We use model output from a CESM hindcast simulation that includes carbon isotopes in the modeled biogeochemistry. These runs are forced with CORE interannually varying forcing from year 1960 to 2009 with atmospheric CO_2 is set to a constant 284.7 ppm, consistent with pre-industrial conditions. Using this forcing provides an indication of the expected response of the natural carbon cycle to the actual changes in climate that occurred in this time period. The impact of rising atmospheric CO_2 on ocean carbon chemistry is not included. The horizontal resolution is nominally 1°x1° with 60 vertical layers in the ocean. The vertical layers in the surface ocean are spaced by 10 m down to 160 m, below which spacing varies and increases to 250 m by ~3600 m depth, thereafter remaining constant down to the modeled maximum depth of 5500 m. The model was run for five 62-year forcing cycles, and we analyze the last 50 years of these 62-year cycles (1960 to 2009). We focus on the following carbon cycle variables in our analysis: NCP, δ^{13}C-DIC, and salinity normalized DIC (sDIC). Within the model, linear trends were removed prior to computing correlation coefficients so as to remove model drift. We focus on the interannual variability signal from this hindcast simulation.

4.2.2 Observational Datasets

We use interpolated World Ocean Atlas (WOA13 v2) data for temperature (Locarnini et al., 2013) and salinity (Zweng et al., 2013) decadally averaged over years 1955 to 2012, and annual mean nitrate (Garcia et al., 2013). We use GLODAP v2016b for DIC and ALK gridded datasets which includes data between 1972 and 2013 (Lauvset et al., 2016). We use the difference between CESM and WOA datasets in the 10 m to 20 m layer to evaluate model bias. We also use Scripps Seawater Carbon time-series data from HOT Station ALOHA (1989 to

2016) and the Bermuda Atlantic Time-series Study (BATS, 1988 to 2017) and Station S (1983 to 2017) which include measurements of sDIC, δ^{13}C-DIC, sALK, salinity, temperature, and MLD to compare with model output at these locations (see Chapter 3). We compare the gridded datasets as well as the time-series records with CESM modeled values across the North Pacific and North Atlantic.

4.2.3 Climate Indices: Sources of Data

The North Atlantic Oscillation (NAO) is based on the relative difference in sea level pressure between the Icelandic high-pressure system and the Bermuda-Azores low pressure system. The NAO is directly related to shifts in the westerlies and therefore the mean wind speed and direction over the North Atlantic, which can determine the strength and location of winter storms in the North Atlantic. During a negative NAO period, westerlies are shifted northward and the strength of winter storms tend to increase near Bermuda in the western North Atlantic. We obtained monthly NAO index data from the National Oceanic and Atmospheric Administration (NOAA) National Weather Service (NWS) Climate Prediction Center website for the NAO (https://cpc.ncep.noaa.gov/data/teledoc/nao.shtml). The strength of the NAO signal is typically greatest in the winter months, so we use the winter mean value of the NAO index during December, January, February and March (DJFM) similar to previous studies (Gruber et al., 2002).

We consider three monthly datasets of dominant modes of variability in the North Pacific which are related to shifts in trade-wind forcing, changes in gyre circulation dynamics, and surface ocean properties. These include the Pacific Decadal Oscillation (PDO), the NINO3.4, and the North Pacific Gyre Oscillation (NPGO). The PDO monthly index is based on the leading principal component of the monthly SST anomalies in the Pacific Ocean, north of 20°N (Mantua

et al., 1997). We obtained PDO index standardized monthly data from Joint Institute for the University of Washington Joint Institute for the Study of the Atmosphere and Ocean (JISAO) website (http://research.jisao.washington.edu/pdo/). We use the NINO3.4 index to represent the El Niño Southern Oscillation (ENSO) climate variability which is based on monthly SST anomalies over the Pacific Ocean region within 5°N to 5°S and 170°W to 120°W. Monthly NINO3.4 data were obtained from the NOAA National Weather Service Climate Prediction Center (https://www.cpc.ncep.noaa.gov/data/indices).Monthly data for the NPGO – based on the second EOF of sea surface height (SSH) variability in the Northeast Pacific (Di Lorenzo et al., 2008) – were obtained from Di Lorenzo's NPGO website (www.o3d.org/npgo).

4.2.4 Data Analysis

HOT is located at 22° 45'N, 159° 00'W and BATS is located at 31° 50'N, 64° 10'W. To compare model output with time-series data from HOT and BATS, we isolate a ~1 degree grid cell located near the latitude and longitude of these stations. We compute the long-term climatological mean at each grid cell over the 50 year period between 1960 and 2009. For sDIC and δ^{13}C-DIC surface values, we use the second layer in the model (10 m to 20 m) to most closely correspond to the sampling depths in the mixed layer for the time-series data at HOT and BATS which ranges from 5 to 25 m. We remove the effects of precipitation and evaporation on DIC values by normalizing to salinity = 35, expressed as salinity normalized DIC (sDIC).

To examine interannual variability we compute annual mean values for each of the time-series records. These annual mean values are used to compare between the time-series records and model output annual mean values. We also use correlation to explore the relationships between the observed and modeled variability, between the modeled variables, as well as between the model and dominant climate modes of variability in the North Atlantic and North

Pacific. For time-series correlations, we use a significance test based on the Ebisuzaki method (Ebisuzaki, 1997) to avoid overconfidence due to autocorrelation. This method assesses statistical significance in the presence of autocorrelation by using an ensemble of (synthetic) time-series with the same power spectrum (and hence the same autocorrelation) as the observed or modeled CESM time-series. We use 1000 iterations and report the likelihood that the correlation is not random by determining the percentage of synthetically derived correlations that are weaker than the correlation from the observed or CESM dataset.

4.3 RESULTS

4.3.1 Comparisons with World Ocean Atlas and Time-series Observations

We compare observational surface seawater data from CESM model output and WOA gridded physical variables and nutrients (temperature, salinity, nitrate) to evaluate model bias on broader basin scales (Figure 4.1). In the North Pacific Subtropical Gyre, we find a negative bias in temperature (< 0.5 °C) and salinity (< 0.5 g kg^{-1}) near Hawaii. Across the subtropical gyre region there is slight negative to zero bias in NO_3 (< 1 μmol L^{-1}). In the North Atlantic Subtropical Gyre, we find with a weak negative to neutral bias in temperature, and weak positive bias in salinity near Bermuda. There is a positive bias in temperature (< 0.4 °C) and negative bias in salinity (< 1 g kg^{-1}) in the southern region of the subtropical gyre. Near and just north of BATS, there is a negative bias in NO_3 (up to 2 μmol L^{-1}), with little to no bias across the southern portion of the gyre.

We also compare interannual variability of the annual mean values from observed time-series data and CESM output from HOT and BATS time-series locations (shown in Figure 4.2). Most notably we see that the model annual mean variability for δ^{13}C-DIC, sDIC, temperature, and salinity at BATS is underestimated, capturing 49% (δ^{13}C-DIC), 75% (sDIC), 48%

(temperature), and 71% (salinity) of the time-series record observed variability for these variables.

At HOT, the magnitude of δ^{13}C-DIC and sDIC variability are overestimated, with the model capturing 113% (δ^{13}C-DIC) and 158% (sDIC) of the observed variability. CESM captures 92% of the observed temperature variability at HOT, which is the best represented of the variables we consider and likely reflects effective CORE forcing within the model. Lastly, we find that salinity variability is somewhat underestimated, with the model capturing 77% of the observed variability. We summarize the standard deviation in the interannual variability of both the time-series observations and CESM variables at HOT and BATS in Table 4.1.

In addition to looking at how the magnitude of variability compares between the model and observations at the time-series locations, we also evaluate how well they correlate with each other. At BATS we found that correlations between modeled and observed δ^{13}C-DIC, sDIC, and salinity were significant, but temperature correlation at BATS was weak and insignificant. At HOT, modeled annual mean temperature correlates well ($r = +0.86$) with the observations, but the correlations between modeled and observed δ^{13}C-DIC, sDIC, and salinity are weak and insignificant. The correlation coefficients between the observations and modeled variability are summarized in Table 4.2.

Overall, within the subtropics, we find that the modeled fields experience relatively low biases for temperature, salinity, and nitrate when compared to WOA gridded data. While there may be larger biases present at higher latitudes, these regions are outside of the focus of this study. Broadly speaking, the CESM data provides internally consistent relationships between the variables of interest, even if the magnitude of the signals do not precisely align with the observations.

4.3.2 Interannual Variability at HOT and BATS and Broader Spatial Variability

We show that there is interannual variability in δ^{13}C-DIC, sDIC, NCP, temperature, and salinity within CESM time-series output at HOT and BATS (Figure 4.2). Comparisons between the two stations show that the sDIC variability is more than twice as large at HOT compared to BATS, and δ^{13}C-DIC variability is also somewhat greater at HOT. In contrast, NCP variability at BATS is greater than the variability in NCP at HOT.

The CESM modeled fields allow us to extend our analysis to the scale of the subtropical gyres across the ocean basins and examine broader spatial variability as well. Figure 4.3 shows maps of the long-term climatological mean fields and standard deviations for sDIC and δ^{13}C-DIC in the North Pacific and North Atlantic between 1960 and 2009. In the subtropical gyre regions of the North Pacific and North Atlantic, long-term climatological mean values of sDIC are approximately 1940 to 2025 μmol kg^{-1} with variability between approximately 5 and 10 μmol kg^{-1}. The long-term climatological mean values of δ^{13}C-DIC are approximately +1.9 to +2.4 ‰ with variability between 0.01 and 0.03 ‰. Figure 4.4 shows maps of the long-term climatological mean NCP field between 1960 and 2009. The mean NCP value is approximately 0.5 to 3 mol C m^{-2} yr^{-1} with variability between 0.2 to 2 mol C m^{-2} yr^{-1}. Similarly, Figure 4.5 shows modeled long-term climatological mean and variability of temperature and salinity fields in the North Pacific and North Atlantic.

The long-term climatological mean spatial variability and standard deviation within the mapped regions (see Figure 4.3, Figure 4.4, and Figure 4.5) show distinct spatial patterns between the North Atlantic and North Pacific subtropical gyres. In the North Atlantic, δ^{13}C-DIC exhibits a north-south gradient with higher values to the south and east, lower values to the north, with a minimum centered in the northwest at 40ºN before increasing significantly in the subpolar

region. sDIC shows a steep and consistent north-south gradient, with higher values to the north and lower values to the south. The annual mean standard deviation is relatively constant throughout the subtropical gyre, with significantly greater variability observed at the western boundary current and northern boundary of the subtropical gyre for both sDIC and δ^{13}C-DIC.

In the North Pacific, δ^{13}C-DIC exhibits a more prominent east-west gradient with higher values to the east and lower values to the west, with a minimum along the Kuroshio. δ^{13}C-DIC also increases to the north outside of the subtropical gyre region. sDIC shows a steep and consistent north-south gradient, with a slightly weaker but also consistent east-west gradient. The lowest sDIC values are found in the southwest region of the subtropical gyre. Here in the North Pacific, the annual mean standard deviation is relatively small consistent through the subtropical gyre for δ^{13}C-DIC, and shows more variability in sDIC throughout the subtropical gyre, with significantly greater variability observed at the Kuroshio and Kuroshio extension along the northern boundary of the subtropical gyre for both sDIC and δ^{13}C-DIC in the North Pacific.

In the North Atlantic, NCP shows minimum values in the southwest corner of the subtropical gyre, with increasing values to the north and east. In the North Pacific, NCP has a wedge-like shape with the broader edge and minimum values along the east around 24ºN. This wedge narrows into the western North Pacific along a weak positive gradient. NCP increase both to the north and south with high NCP evident along the Kuroshio and Kuroshio extension. There is moderate variability in the annual mean standard deviation for NCP in both the North Atlantic and North Pacific subtropical gyres, with greater variability observed along the western boundary currents in both regions.

In both the North Pacific and North Atlantic, SST values show a consistent north-south gradient with colder water to the north, and warmer water to the south. The SST annual mean

standard deviation in the North Atlantic varies somewhat less than the North Pacific, and in both cases the highest variability is observed along the western boundary currents and northern boundaries of the subtropical gyres. In the North Atlantic, salinity decreases somewhat to the north and increases to the south with a maximum along 24ºN toward the southeast region of the subtropics. In the North Pacific, salinity patterns in the are centered around an oval shaped maximum oriented with the approximate center of the subtropical gyre and centered around 24ºN with negative gradients radiating outward in all directions. The annual mean standard deviation for salinity is quite small for salinity in both regions.

The locations of the BATS and HOT time-series stations result in different gradients and patterns relative to each of these variables. BATS is located such that the gradient in δ^{13}C-DIC and salinity decrease to the north, and increases to the south while sDIC, NCP, and SST all increase to the north and decreases to the south. At BATS, the lateral gradients are all relatively weak. HOT is located such that there are both lateral and longitudinal gradients in δ^{13}C-DIC, sDIC, salinity, and to a lesser extent, NCP. At HOT, δ^{13}C-DIC decreases to the northwest and increases to the east and north, while sDIC increases sharply to the north and east with a more gradual decrease to the west. NCP at HOT increases to the north and south and decreases to the east, and salinity decreases in all directions, although to a somewhat lesser extent east and west. At both HOT and BATS, the SST gradient is positive to the north.

To explore spatial correlation scales, we compared the variability at BATS and HOT to the surrounding regions for each station. We find strong correlation throughout the North Atlantic Subtropical Gyre between the variability at BATS and surrounding area for sDIC, δ^{13}C-DIC, NCP, temperature (Figures 4.6, 4.7 4.8, and 4.10). In the North Pacific we see that HOT is

correlated with nearby surface water variability, along the dominant path of circulation in this portion of the subtropical gyre for sDIC, δ^{13}C-DIC, and NCP to varying extents.

4.3.3 Time-series Station Spatial Scales of Correlation

We evaluate the spatial scales over which the interannual variability in sDIC, δ^{13}C-DIC, and NCP along with other oceanographic variables at HOT and BATS are correlated with the variability in surrounding waters within the model. To do this, the modeled interannual variability at HOT and BATS were correlated within the North Pacific and North Atlantic respectively. These correlations between HOT and BATS sDIC and δ^{13}C-DIC with surrounding waters are mapped in Figure 4.6 and Figure 4.7. NCP correlation maps between the time-series sites and surrounding region are shown in Figure 4.8. We further explore the relationship between δ^{13}C-DIC and NCP, Figure 4.9 which shows the strong correlation between the δ^{13}C-DIC and NCP interannual variability at each grid cell location. Figure 4.10 shows correlation between the time-series sites and surrounding region for area surface temperature fields.

4.3.4 Correlation with Climate Indices

To explore mechanisms driving interannual variability, we compute the correlation between CESM variables and dominant modes of climate variability. We summarize these correlations and their significance in Table 4.3. We also show correlation maps with climate mode indices regressed onto each grid cell of the variables of interest. Figure 4.11 shows the mapped correlation between the NAO and North Atlantic values of sDIC, δ^{13}C-DIC, temperature, and NCP. These maps show relatively broad areas of significant NAO correlation with sDIC (negative) and δ^{13}C-DIC (positive) centered around the gyre near BATS. The NAO correlation with temperature and NCP is patchy within the subtropical gyre.

Figure 4.12 shows the mapped correlation between the PDO and sDIC, δ^{13}C-DIC, temperature, and NCP at each grid cell. The correlation with the PDO consistently places HOT in a node between regions of significant positive and negative correlations in the North Pacific basin. Figure 4.13 and Figure 4.14 show maps of the NPGO and ENSO3.4 correlated respectively with sDIC, δ^{13}C-DIC, temperature, and NCP. These figures show some correlation with ENSO3.4 and NPGO, however the significance of these correlations disappears near HOT and illustrates further its position on the node of North Pacific variability patterns, not just of the PDO, but also of NPGO and ENSO3.4.

4.4 DISCUSSION

4.4.1 Structure of sDIC, δ^{13}C-DIC, and NCP variability in the North Pacific and North Atlantic subtropical gyres

The homogenous variability that we see in the North Atlantic Subtropical Gyre supports the idea that interannual variability at BATS is spatially coherent with the broader subtropical gyre region in the North Atlantic e.g. (Bates, 2007; Gruber et al., 2002). In contrast, the North Pacific subtropical gyre encompasses a much larger region and the two dominant patterns of variability observed here (especially in sDIC and SST) are divided roughly into the east and west Pacific (Karl, 1999; Kavanaugh et al., 2018; Yasunaka et al., 2014). As a result, the spatial correlation scale at HOT does not encompass the full extent of the gyre, but instead a subset of this region. It is important to note that these spatial correlation assessments only capture the region over which there is instantaneous correlation of variability, or decorrelation length scales of the time-series locations. This does not include a full assessment of the lag correlations or temporal influence of potential up stream forcing, which may yield longer scales of correlation.

4.4.2 Controls on sDIC, δ^{13}C-DIC, and NCP variability at HOT and BATS

The model results indicate a strong role for variability in SST in driving variability in sDIC at both stations. This is supported by the significant negative correlation between SST and sDIC interannual variability at BATS (r = -0.83) and HOT (r = -0.56) (see Table 4.3). At BATS, this correlation appears to be strongly connected to SST anomalies in combination with the role of MLD which can reach down to 400 m (Chapter 3). However, HOT does not exhibit the same relationship with MLD. MLD at HOT is typically much shallower relative to BATS, reaching depths of ~125m at most (Chapter 3).

Figure 4.15 shows property-property plots of sDIC and δ^{13}C-DIC for the mean seasonal cycle, interannual variability (annual mean), and vertical profiles down to 200m, and provides valuable information about what processes may influence variability on different timescales (seasonal and interannual) as well as how sDIC and δ^{13}C-DIC vary along the vertical gradient. Observations are shown in black and CESM output is shown in teal. Of interest is the slope of these property-property plots. Figure 4.15 shows that the modeled slopes for both annual mean variability and seasonal cycle agree well with the observed slopes for both stations (HOT and BATS). This agreement suggests that the CESM model may correctly identify the dominant processes responsible for variability in sDIC and δ^{13}C-DIC on different timescales, even while the model struggles to correctly represent the magnitude of the variability.

At BATS, the changes in sDIC and δ^{13}C-DIC on seasonal and interannual timescales appear to occur more or less along the same slope. In addition, these slopes correspond well to the vertical profile gradients in sDIC and δ^{13}C-DIC.The similarity of the relative gradients in the vertical profiles of sDIC and δ^{13}C-DIC in the North Atlantic helps to illustrate that vertical mixing is a strong driver on interannual (as well as seasonal) timescales, confirming what

previous studies have shown for this region e.g. (Bates, 2012; Bates et al., 1996; Gruber et al., 2002; Keller et al., 2012). The strength of vertical mixing is typically strongest in the winter months, dependent on temperature and the strength of winter storms which drive large variation in mixed layer depth and vertical entrainment. As previous studies have shown, this variability is correlated with the NAO (e.g. Chapter 3; Bates et al., 2012; Gruber et al., 2002) and we also see correlation between the NAO and δ^{13}C-DIC (r = +0.51), sDIC (-0.39), and SST (+0.28) at BATS (Table 4.3). The exception is that NCP does not appear to correlate significantly with the NAO here, but NCP is correlated with the other variables which do appear to be influenced by the NAO.

At HOT, the seasonal cycles and interannual variability in sDIC and δ^{13}C-DIC have slopes which are both distinct from the vertical slope and each other, suggesting different processes are responsible for variability on different timescales. This is consistent with earlier studies which have also indicated that the vertical gradients in sDIC and δ^{13}C-DIC are not the main driver for the seasonal cycle or interannual variability in the North Pacific where there are other dominant controls such as horizontal advection and strong precipitation and evaporation signals etc. (Brix et al., 2004; Dore et al., 2003; Letscher et al., 2016). To help understand this complexity, we show a scatter plot of sDIC and δ^{13}C-DIC formed along lateral transects in the location of HOT (Figure 4.16). The East-West transect shows a similar slope in the sDIC vs δ^{13}C-DIC gradients that resembles what we see on interannual timescales, suggesting that shifts in horizontal advection from the east could explain some of the interannual variability.

Part of the difference in variability drivers at HOT is also likely connected to a roughly bimodal east-west pattern of variability observed in the North Pacific, linked to dominant modes of climate variability in the region (Brix et al., 2004; Kavanaugh et al., 2018; McKinley et al.,

2006; Yasunaka et al., 2014). This bimodal pattern is especially apparent in SST, and includes a node or transition point between the east-west regions. The location of HOT near the node of east-west variability in the North Pacific (Karl, 1999; Brix et al, 2004; Kavanaugh et al., 2018; Yasunaka et al., 2014) yields interannual variability that is not dominantly linked to a single source of variability, but instead is susceptible to regime shifts. However, when correlating climate indices at each grid cell across the North Pacific (for example with the PDO, Figure 4.12) we see that there is broad spatial coherence and significant correlation on either side of that bimodal pattern, supporting the idea of two dominant regions of variability in the North Pacific subtropical gyre (Karl, 1999). This suggests that the drivers of variability in the rest of the gyre region are likely more strongly tied to the dominant modes of climate variability than some of the observations at HOT show, consistent with what previous studies have shown or hypothesized (Brix et al., 2004; Kavanaugh et al., 2018).

The significant correlation between sDIC at HOT and sDIC in the surrounding surface waters shows up in a similar bimodal pattern (Figure 4.6) that closely resembles what we see in the corresponding SST correlation in the North Pacific (Figure 4.10). This is likely due to the influence of solubility temperature dependency and the ~1year equilibration timescale of sDIC (Broecker and Peng, 1974; Jones et al., 2014). This bimodal pattern in SST is also correlated with the PDO, as illustrated by the correlation pattern of these two variables in Figure 4.12.

However, we do not expect SST to exert the same control over δ^{13}C-DIC variability because of the difference in equilibrium timescales, which for δ^{13}C-DIC is an order of magnitude greater at roughly 10 years (Broecker and Peng, 1974). As such, the dominant forcing for δ^{13}C-DIC variability on interannual timescales are instead focused within the surface ocean (biological forcing/NCP and horizontal advection), or, to a smaller extent in the NPSG, entrainment of

waters from below the mixed layer (vertical mixing). Indeed, we see that the correlation between δ^{13}C-DIC at HOT and the surrounding surface waters (Figure 4.7) shows up in a pattern that more closely resembles the pattern we see in the correlation between NCP annual mean values at HOT and the surrounding NPSG (Figure 4.8). This relationship helps to illustrate the strong connection between the influence of photosynthetic fractionation on the variability in δ^{13}C-DIC in surface seawater. This is further bolstered by how well δ^{13}C-DIC and NCP correlate at each grid cell location (Figure 4.9).

As mentioned above and shown in Figure 4.12-4.14, CESM places HOT near the nodes of the bimodal variability for all three indices PDO, NPGO, and NINO3.4. The exact position of the modeled nodes, which are typically oriented along a roughly northeast/southwest axis near HOT, depends both on the indices (PDO, NPGO, NINO3.4) and the variables (e.g. δ^{13}C-DIC, sDIC, and SST).

For the PDO, CESM places HOT on the southeast side of the node for all three variables δ^{13}C-DIC, sDIC, and SST), and the sign of the modeled correlation for all three variables (δ^{13}C-DIC (positive), sDIC (negative), and SST (positive)) (see Table 4.3) agrees with observations (Chapter 3, Table 3.4). Assuming CESM correctly simulates the general pattern of PDO variability, this suggests that, in the real ocean, HOT is also located on the southeast side of the PDO pattern and that the model has correctly simulated this detail.

For the NPGO, CESM places HOT on the southeast side of the modeled node in sDIC and SST, but on the northwest side of the node in δ^{13}C-DIC. The sign of the modeled correlation ((δ^{13}C-DIC (positive), sDIC (positive), and SST (negative), again agrees with the observations (Chapter 3, Table 3.4), suggesting that CESM has also correctly positioned the NPGO nodes in relation to HOT.

For NINO3.4, CESM places HOT on the southeast side of the modeled node in sDIC and on the northwest side of the modeled nodes in δ^{13}C-DIC and SST. In this case, while the model correctly represents the sign of the correlations with sDIC (negative), it misrepresents the sign of the observed correlations for δ^{13}C-DIC (positive) and SST (positive). This suggest that, in the real ocean, HOT is located on the southeast side of the nodes for NINO3.4 for all three variables (sDIC, δ^{13}C-DIC, SST), but that this detail is correctly captured in the model only for sDIC but not for δ^{13}C-DIC and SST.

These results show that, in the real ocean, HOT appears to be almost always located on the southeast side of the node for these dominant patterns of variability, the only exception being to the northwest side for the δ^{13}C-DIC versus NPGO correlation. This difference in δ^{13}C-DIC placement for the NPGO appears to follow the modeled pattern of NCP, which is also on the northwest side of the node and likely reflects the strong relationship between NCP and δ^{13}C-DIC variability within the surface ocean. These features are correctly captured in CESM for the PDO and NPGO, but not for NINO3.4.

4.4.2 Summary

In this chapter we showed that CESM modeled interannual variability in sDIC and δ^{13}C-DIC are relatively well captured at BATS, although variability is somewhat underestimated in the model. The variability at HOT in sDIC and δ^{13}C-DIC does not agree as well with observed variability. However, we also showed that the relationship between sDIC and δ^{13}C-DIC is fairly well represented on both seasonal and interannual timescales, suggesting that the dominant processes driving this variability in sDIC and δ^{13}C-DIC are likely well represented within the model, even while the timing and magnitude of variability isn't consistent between the model and observations.

We show evidence supporting the dominance of vertical processes in driving variability in carbon cycle at BATS on both seasonal and interannual timescales, and also show coherent patterns of variability across the North Atlantic Subtropical Gyre that are well correlated with the NAO. In contrast, at HOT we show that interannual variability is not dominated by vertical mixing, and instead likely driven by horizontal advection and/or gyre circulation shifts, with correlation patterns representing a subset of the broader North Pacific Subtropical Gyre. The observations indicate that HOT is situated slightly to the southeast of the node of variability in the North Pacific, and the model attribution of this station placement is in rough agreement. Our findings also support earlier publications that suggest that the HOT location may obscure patterns of variability due to proximity to the node of the east-west bimodal pattern of variability linked to the PDO and other dominant modes of climate variability in the North Pacific.

4.5 ACKNOWLEDGEMENTS

We would like to thank NCAR and the CESM community for providing support via the University Graduate Student Allocation and for allowing us to use model output and computing resources during this project.

Chapter 4 in part is being prepared for publication of the material. Brooks, Mariela K; Long, Matthew C; Keeling, Ralph F. The dissertation author was the primary investigator and author of this material.

4.6 REFERENCES

Bates, N.R., 2012. Multi-decadal uptake of carbon dioxide into subtropical mode water of the North Atlantic Ocean. Biogeosciences 9, 2649–2659. https://doi.org/10.5194/bg-9-2649-2012.

Bates, N.R., 2007. Interannual variability of the oceanic CO2 sink in the subtropical gyre of the North Atlantic Ocean over the last 2 decades. Journal of Geophysical Research 112. https://doi.org/10.1029/2006JC003759.

Bates, N.R., Michaels, A.F., Knap, A.H., 1996. Seasonal and interannual variability of oceanic carbon dioxide species at the US JGOFS Bermuda Atlantic Time-series Study (BATS) site. Deep Sea Research Part II: Topical Studies in Oceanography 43, 347–383.

Brix, H., Gruber, N., Keeling, C.D., 2004. Interannual variability of the upper ocean carbon cycle at station ALOHA near Hawaii. Global Biogeochemical Cycles 18. https://doi.org/10.1029/2004GB002245.

Broecker, W.S., Peng, T.-H., 1974. Gas exchange rates between air and sea. Tellus 26, 21–35. https://doi.org/10.1111/j.2153-3490.1974.tb01948.x.

Di Lorenzo, E., Schneider, N., Cobb, K.M., Franks, P.J.S., Chhak, K., Miller, A.J., McWilliams, J.C., Bograd, S.J., Arango, H., Curchitser, E., Powell, T.M., Rivière, P., 2008. North Pacific Gyre Oscillation links ocean climate and ecosystem change. Geophysical Research Letters 35. https://doi.org/10.1029/2007GL032838.

Dore, J.E., Lukas, R., Sadler, D.W., Karl, D.M., 2003. Climate-driven changes to the atmospheric CO2 sink in the subtropical North Pacific Ocean. Nature 424, 754–757. https://doi.org/10.1038/nature01885.

Ebisuzaki, W., 1997. A Method to Estimate the Statistical Significance of a Correlation When the Data Are Serially Correlated. Journal of Climate 10, 2147–2153. https://doi.org/10.1175/1520-0442(1997)010<2147:AMTETS>2.0.CO;2.

Garcia, H.E., Locarnini, R.A., Boyer, T.P., Antonov, J.I., Baranova, O.K., Zweng, M.M., Reagan, J.R., Johnson, D.R., 2013. World Ocean Atlas 2013. Vol. 4: Dissolved Inorganic Nutrients (phosphate, nitrate, silicate) (No. 76), NOAA Atlas NESDIS.

Gruber, N., Keeling, C.D., Bates, N.R., 2002. Interannual Variability in the North Atlantic Ocean Carbon Sink. Science 298.

Gruber, N., Keeling, C.D., Stocker, T.F., 1998. Carbon-13 constraints on the seasonal inorganic carbon budget at the BATS site in the northwestern Sargasso Sea. Deep-Sea Research I 45, 673–717.

Hurrell, J.W., Kushnir, Y., Ottersen, G., Visbeck, M., 2003. An overview of the North Atlantic Oscillation, in: Hurrell, J.W., Kushnir, Y., Ottersen, G., Visbeck, M. (Eds.), Geophysical Monograph Series. American Geophysical Union, Washington, D. C., pp. 1–35. https://doi.org/10.1029/134GM01.

Jones, D.C., Ito, T., Takano, Y., Hsu, W.-C., 2014. Spatial and seasonal variability of the air-sea equilibration timescale of carbon dioxide. Global Biogeochemical Cycles 28, 1163–1178. https://doi.org/10.1002/2014GB004813.

Karl, D.M., 2002. Nutrient dynamics in the deep blue sea. Trends in Microbiology 10, 410–418. https://doi.org/10.1016/S0966-842X(02)02430-7.

Karl, D.M., 1999. A Sea of Change: Biogeochemical Variability in the North Pacific Subtropical Gyre 34.

Kavanaugh, M.T., Church, M.J., Davis, C.O., Karl, D.M., Letelier, R.M., Doney, S.C., 2018. ALOHA From the Edge: Reconciling Three Decades of in Situ Eulerian Observations and Geographic Variability in the North Pacific Subtropical Gyre. Frontiers in Marine Science 5. https://doi.org/10.3389/fmars.2018.00130.

Keeling, C.D., Brix, H., Gruber, N., 2004. Seasonal and long-term dynamics of the upper ocean carbon cycle at Station ALOHA near Hawaii. Global Biogeochemical Cycles 18, n/a-n/a. https://doi.org/10.1029/2004GB002227.

Keller, K.M., Joos, F., Raible, C.C., Cocco, V., Frölicher, T.L., Dunne, J.P., Gehlen, M., Bopp, L., Orr, J.C., Tjiputra, J., Heinze, C., Segschneider, J., Roy, T., Metzl, N., 2012. Variability of the ocean carbon cycle in response to the North Atlantic Oscillation. Tellus B: Chemical and Physical Meteorology 64, 18738. https://doi.org/10.3402/tellusb.v64i0.18738.

Lauvset, S.K., Key, R.M., Olsen, A., van Heuven, S., Velo, A., Lin, X., Schirnick, C., Kozyr, A., Tanhua, T., Hoppema, M., Jutterström, S., Steinfeldt, R., Jeansson, E., Ishii, M., Perez, F.F., Suzuki, T., Watelet, S., 2016. A new global interior ocean mapped climatology: the 1◦ × 1◦ GLODAP version 2. Earth System Science Data 8, 325–340. https://doi.org/10.5194/essd-8-325-2016.

Le Quéré, C., Andrew, R.M., Friedlingstein, P., Sitch, S., Hauck, J., Pongratz, J., Pickers, P.A., Korsbakken, J.I., Peters, G.P., Canadell, J.G., Arneth, A., Arora, V.K., Barbero, L., Bastos, A., Bopp, L., Chevallier, F., Chini, L.P., Ciais, P., Doney, S.C., Gkritzalis, T., Goll, D.S., Harris, I., Haverd, V., Hoffman, F.M., Hoppema, M., Houghton, R.A., Hurtt, G., Ilyina, T., Jain, A.K., Johannessen, T., Jones, C.D., Kato, E., Keeling, R.F., Goldewijk, K.K., Landschützer, P., Lefèvre, N., Lienert, S., Liu, Z., Lombardozzi, D., Metzl, N., Munro, D.R., Ono, T., Patra, P., Peregon, A., Peters, W., Peylin, P., Pfeil, B., Pierrot, D., Poulter, B., Rehder, G., Resplandy, L., Robertson, E., Rocher, M., Rödenbeck, C., Schuster, U., Schwinger, J., Séférian, R., Skjelvan, I., Steinhoff, T., Sutton, A., Tans, P.P., Tian, H., Tilbrook, B., Tubiello, F.N., 2018. Global Carbon Budget 2018. Earth System Science Data 10, 2141–2194.

Letscher, R.T., Primeau, F., Moore, J.K., 2016. Nutrient budgets in the subtropical ocean gyres dominated by lateral transport. Nature Geoscience 9, 815. https://doi.org/10.1038/ngeo2812.

Locarnini, R.A., Mishonov, A.V., Antonov, J.I., Boyer, T.P., Garcia, H.E., Baranova, O.K., Zweng, M.M., Paver, C.R., Reagan, J.R., Johnson, D.R., Hamilton, M., Seidov, D., 2013. World Ocean Atlas 2013, Volume 1: Temperature (No. 73), NOAA Atlas NESDIS.

Lueker, T.J., Keeling, C.D., Guenther, P.R., Wahlen, M., 1998. Inorganic carbon variations in

surface ocean water near Bermuda (SIO Technical Report). UC San Diego: Scripps Institution of Oceanography.

McClain, C.R., Signorini, S.R., Christian, J.R., 2004. Subtropical gyre variability observed by ocean-color satellites. Deep Sea Research Part II: Topical Studies in Oceanography 51, 281–301. https://doi.org/10.1016/j.dsr2.2003.08.002.

McKinley, G.A., Takahashi, T., Buitenhuis, E., Chai, F., Christian, J.R., Doney, S.C., Jiang, M.-S., Lindsay, K., Moore, J.K., Le Quéré, C., Lima, I., Murtugudde, R., Shi, L., Wetzel, P., 2006. North Pacific carbon cycle response to climate variability on seasonal to decadal timescales. J. Geophys. Res. 111, C07S06. https://doi.org/10.1029/2005JC003173.

Newman, M., Alexander, M.A., Ault, T.R., Cobb, K.M., Deser, C., Di Lorenzo, E., Mantua, N.J., Miller, A.J., Minobe, S., Nakamura, H., Schneider, N., Vimont, D.J., Phillips, A.S., Scott, J.D., Smith, C.A., 2016. The Pacific Decadal Oscillation, Revisited. Journal of Climate 29, 4399–4427. https://doi.org/10.1175/JCLI-D-15-0508.1.

Quay, P., Stutsman, J., 2003. Surface layer carbon budget for the subtropical N. Pacific: constraints at station ALOHA. Deep Sea Research Part I: Oceanographic Research Papers 50, 1045–1061. https://doi.org/10.1016/S0967-0637(03)00116-X.

Sabine, C.L., Tanhua, T., 2010. Estimation of Anthropogenic CO2 Inventories in the Ocean. Annual Review of Marine Science 2, 175–198. https://doi.org/10.1146/annurev-marine-120308-080947.

Williams, P.J.B., 1993. On the definition of plankton production terms. ICES Marine Science Symposium 197, 9–19.

Yasunaka, S., Nojiri, Y., Nakaoka, S., Ono, T., Mukai, H., Usui, N., 2014. North Pacific dissolved inorganic carbon variations related to the Pacific Decadal Oscillation. Geophys. Res. Lett. 41, 2013GL058987. https://doi.org/10.1002/2013GL058987.

Zweng, M.M., Reagan, J.R., Antonov, J.I., Locarnini, R.A., Mishonov, A.V., Boyer, T.P., Garcia, H.E., Baranova, O.K., Johnson, D.R., Seidov, D., Biddle, M.M., 2013. World Ocean Atlas 2013, Volume 2: Salinity (No. 74), NOAA Atlas NESDIS.

4.7: TABLES

Table 4.1: Standard deviation of annual mean variability, comparison between observations (Obs) and modeled data (CESM) at HOT and S-BATS locations.

Parameter	HOT Obs	HOT CESM	S-BATS Obs	S-BATS CESM
δ^{13}C-DIC (‰)	±0.0166	±0.0187	±0.0277	±0.0136
sDIC (μmol kg^{-1})	±3.57	±5.63	±3.10	±2.34
NCP* (mol m^{-2} yr^{-1})	NaN	±0.14	NaN	±0.39
Temp (°C)	±0.36	±0.33	±0.50	±0.24
Salinity (psu)	±0.13	±0.07	±0.07	±0.05
MLD** (m)	±7.3	NaN	±9.7	NaN

*NCP estimates not available from time-series observations.

Table 4.2: Correlation coefficients between time-series observations and CESM interannual variability data at HOT and BATS. Statistically significant* correlations above a 95% confidence limit are shown in bold.

Parameter	HOT CESM vs Obs Correlation	S-BATS CESM vs Obs Correlation
δ^{13}C-DIC (‰)	+0.07 *(60.1%)*	+0.57 *(93.6%)*
sDIC (μmol kg^{-1})	+0.28 *(74.8%)*	**+0.53** *(96.7%)*
Temp (°C)	**+0.86** *(96.9%)*	+0.46 *(94.3%)*
Salinity (psu)	+0.24 *(79.3%)*	**+0.68** *(96.9%)*

*Values in parentheses give likelihood (in percentage) that correlations are not random determined using the Ebisuzaki (1997) significance test.

Table 4.3: Correlation coefficients of CESM interannual variability data at HOT and BATS locations. Statistically significant* correlations above a 95% confidence limit are shown in bold.

S-BATS Correlation

	δ^{13}C-DIC	sDIC	NCP	Temp	NAO_{DJFM}
δ^{13}C-DIC	1	-	-	-	-
sDIC	**-0.71** *(>99.9%)*	1	-	-	-
NCP	**+0.35** *(95.5%)*	**-0.56** *(>99.9%)*	1	-	-
Temp	**+0.67** *(>99.9%)*	**-0.83** *(>99.9%)*	**+0.53** *(96.9%)*	1	-
NAO_{DJFM}	**+0.51** *(96.9%)*	**-0.39** *(>99.9%)*	+0.21 *(90.8%)*	**+0.28** *(95.1%)*	1

HOT Station ALOHA Correlation

	δ^{13}C-DIC	sDIC	NCP	Temp	PDO	NINO3.4	NPGO
δ^{13}C-DIC	1	-	-	-	-	-	-
sDIC	**+0.70** *(96.7%)*	1	-	-	-	-	-
NCP	+0.30 *(89.1%)*	+0.35 *(88.5%)*	1	-	-	-	-
Temp	-0.02 *(53.3%)*	**-0.56** *(>99.9%)*	-0.05 *(61.1%)*	1	-	-	-
PDO	+0.31 *(88.3%)*	-0.19 *(89.6%)*	-0.01 *(56.3%)*	**+0.31** *(99.2%)*	1	-	-
NINO3.4	-0.08 *(68.4%)*	-0.11 *(74.2%)*	-0.21 *(85.7%)*	-0.14 *(52.0%)*	-	1	-
NPGO	+0.27 *(80.5%)*	+0.50 *(93.4%)*	+0.35 *(91.6%)*	-0.25 *(86.3%)*	-	-	1

*Values in parentheses give likelihood (in percentage) that correlations are not random–determined using the Ebisuzaki (1997) significance test.

4.8: FIGURES

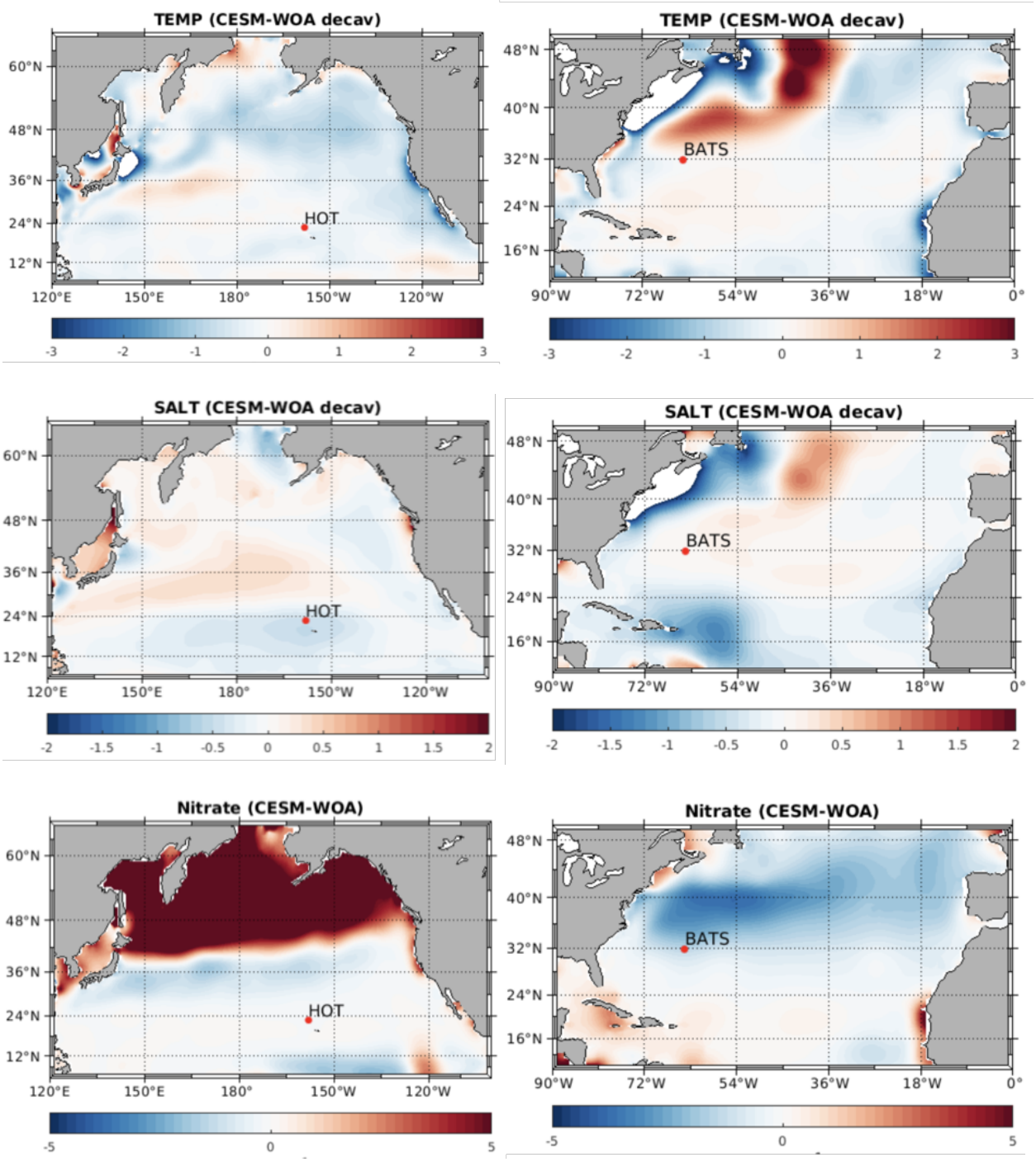

Figure 4.1: CESM bias of temperature (°C), salinity, and nitrate (μmol kg^{-1}) at 20 m compared with WOA gridded datasets. Mapped values show the difference between the long-term climatological average of CESM between 1960 and 2009 and the decadal average of WOA (1955-2012).

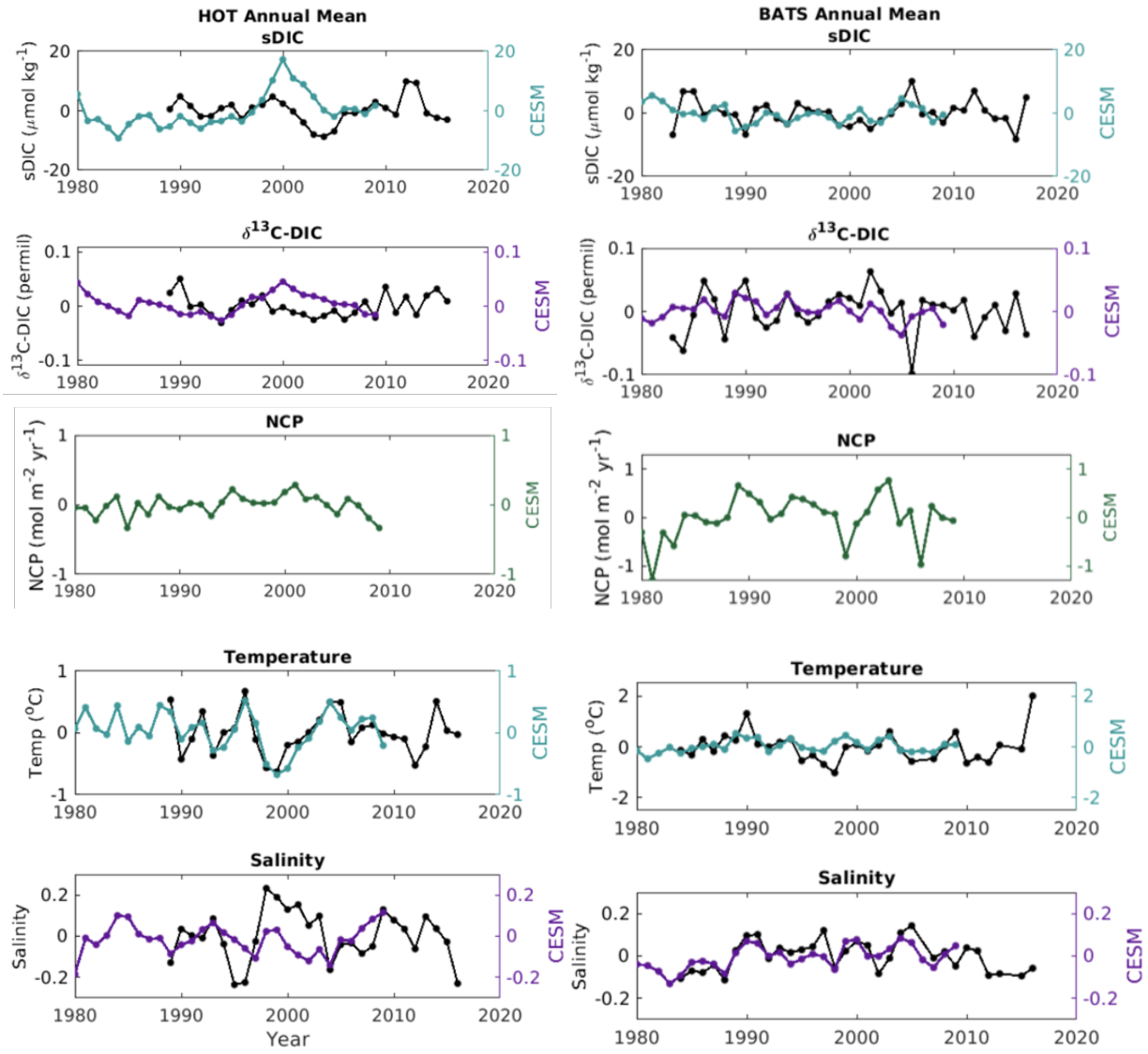

Figure 4.2: Observed (black) and CESM (colors) annually averaged with mean values removed leaving interannual variability for sDIC, δ^{13}C-DIC, NCP, SST, and salinity at HOT (left) and BATS (right). NCP time-series shows only modeled values.

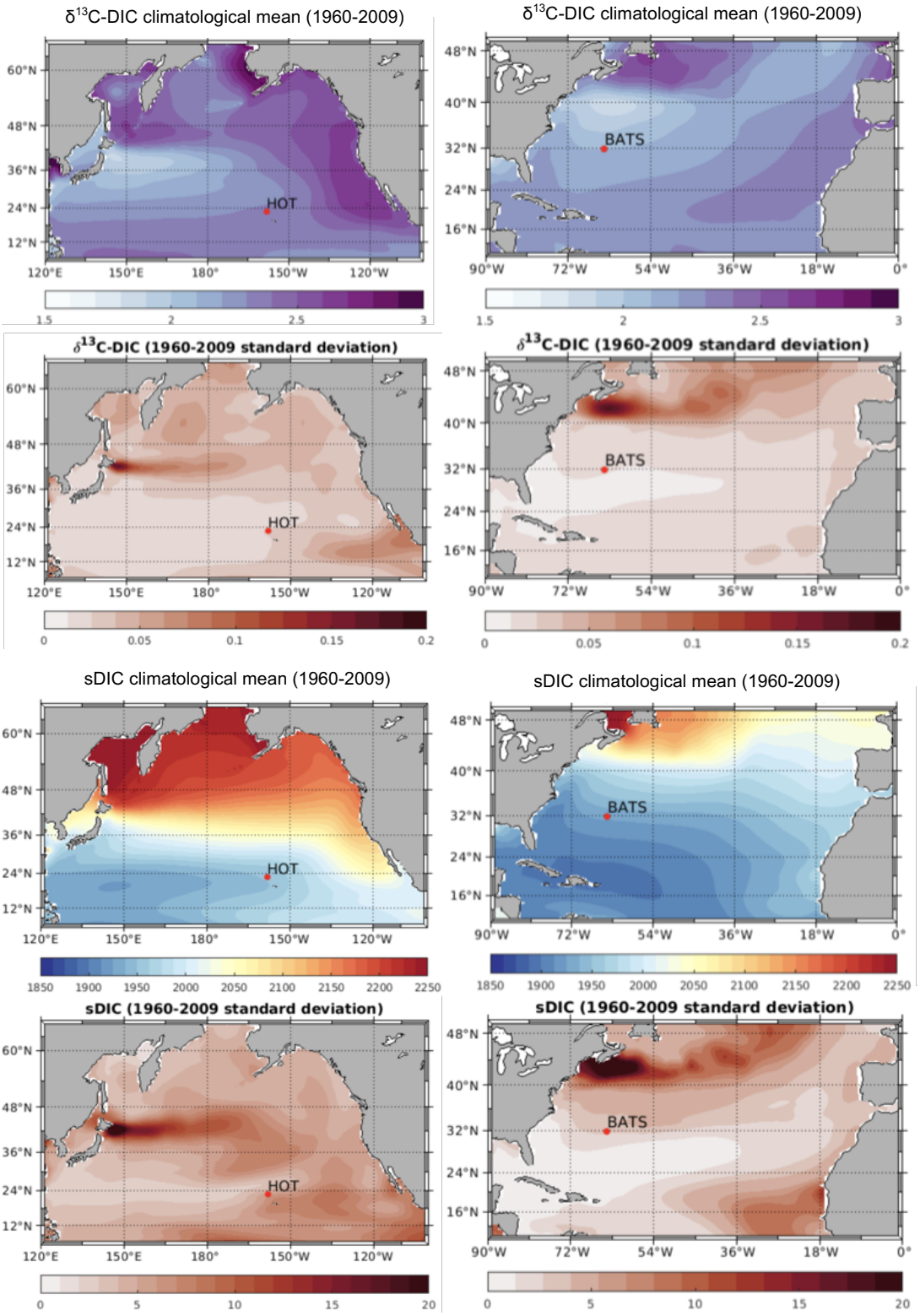

Figure 4.3: δ^{13}C-DIC (‰, top two rows) and sDIC (μmol kg^{-1}, bottom two rows) long-term climatological average and standard deviation between 1960 and 2009 in the North Pacific (left) and North Atlantic (right).

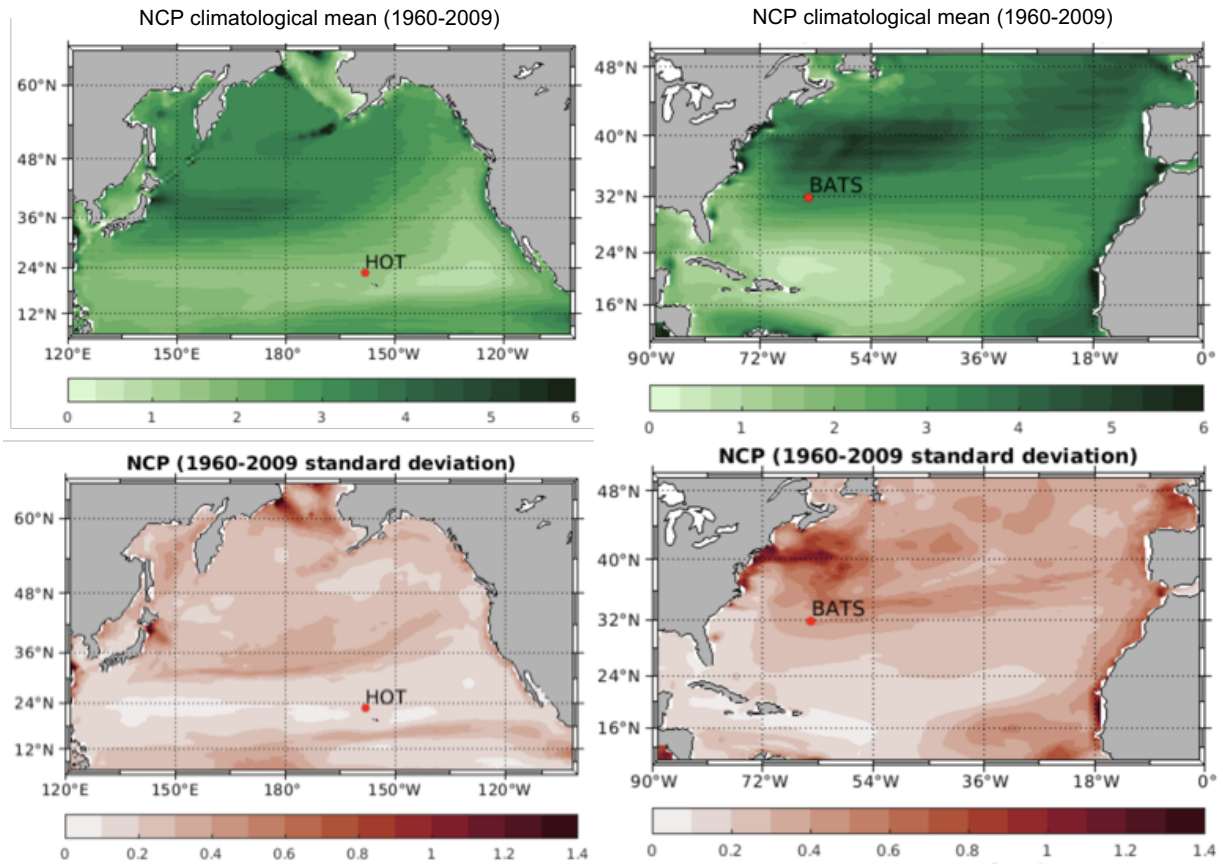

Figure 4.4: NCP (mol C m-2 yr-1) long-term climatological mean between 1960 and 2009 (top) and standard deviation (bottom) in the North Pacific (left) and North Atlantic (right).

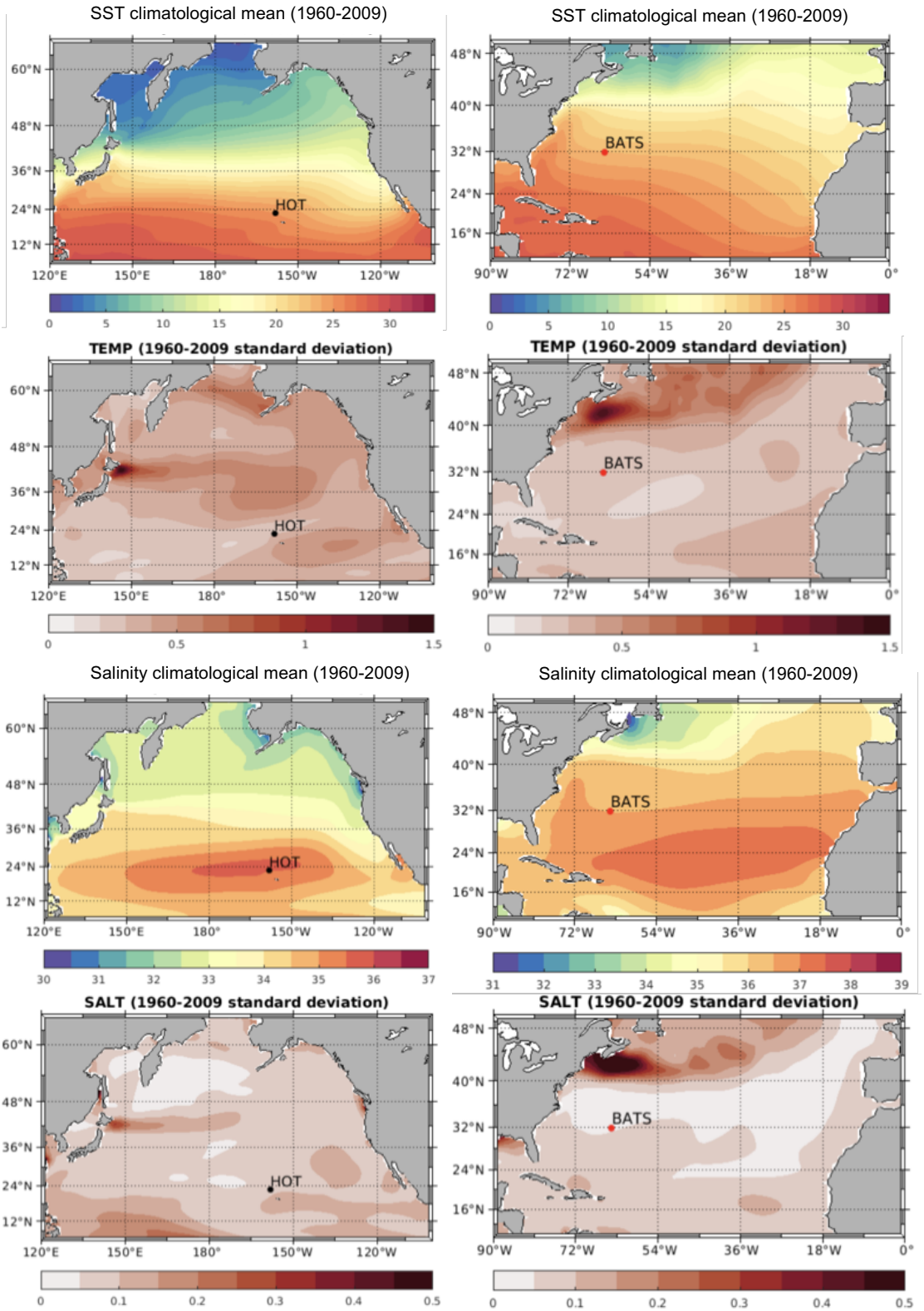

Figure 4.5: Long-term climatological mean and standard deviation between 1960 and 2009 for temperature (°C, top two rows) and salinity (bottom two rows) in the North Pacific (left) and North Atlantic (right).

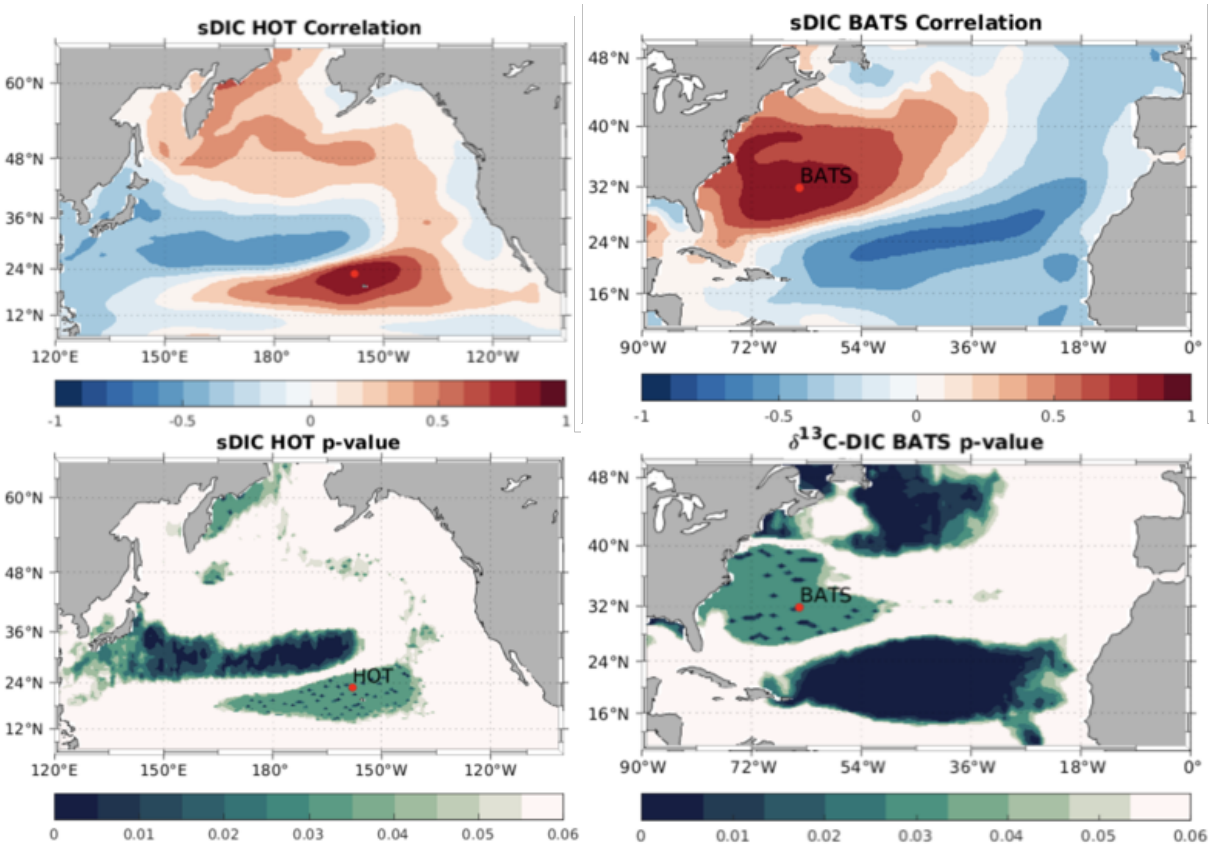

Figure 4.6: Correlation between CESM sDIC at HOT and BATS with the surrounding region.

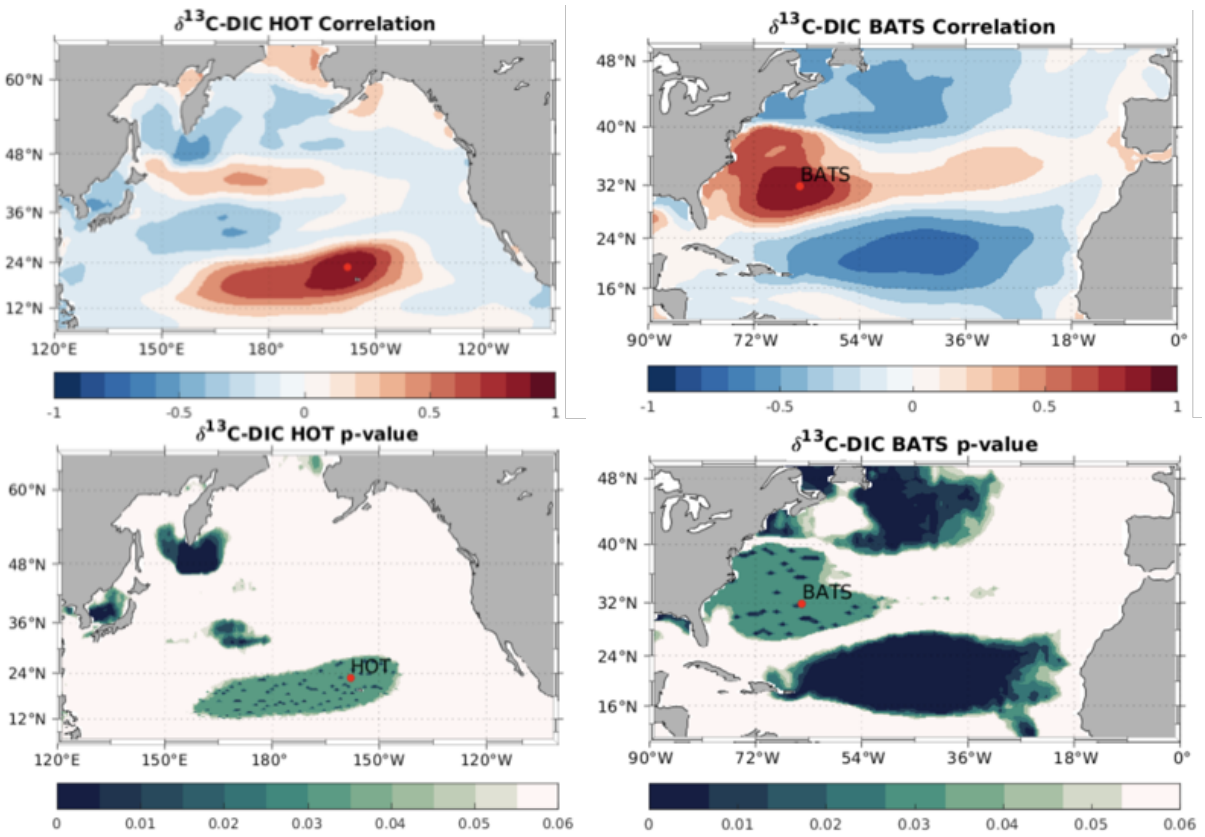

Figure 4.7: Correlation between CESM δ^{13}C-DIC bottom panels at HOT (left) and BATS (right) with the surrounding region.

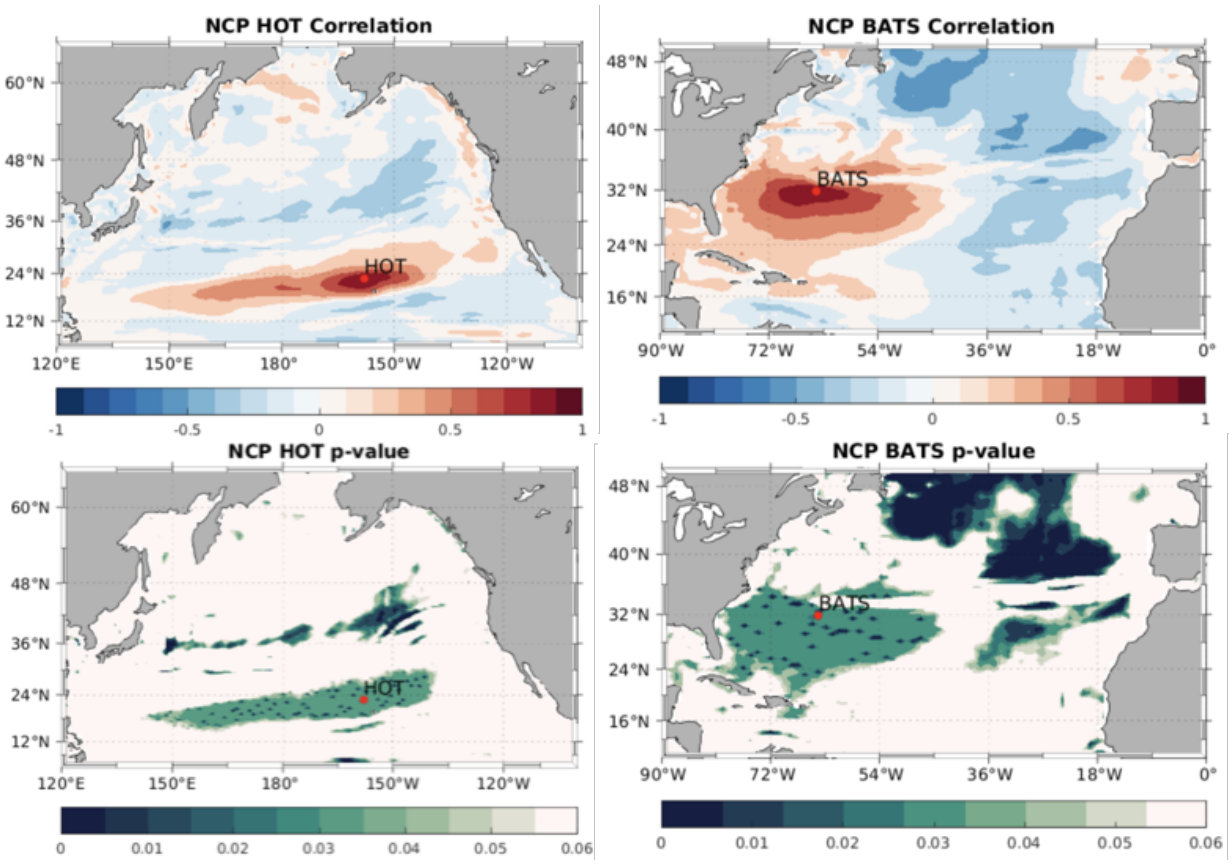

Figure 4.8: Correlation between NCP at HOT (left) and BATS (right) with the surrounding region.

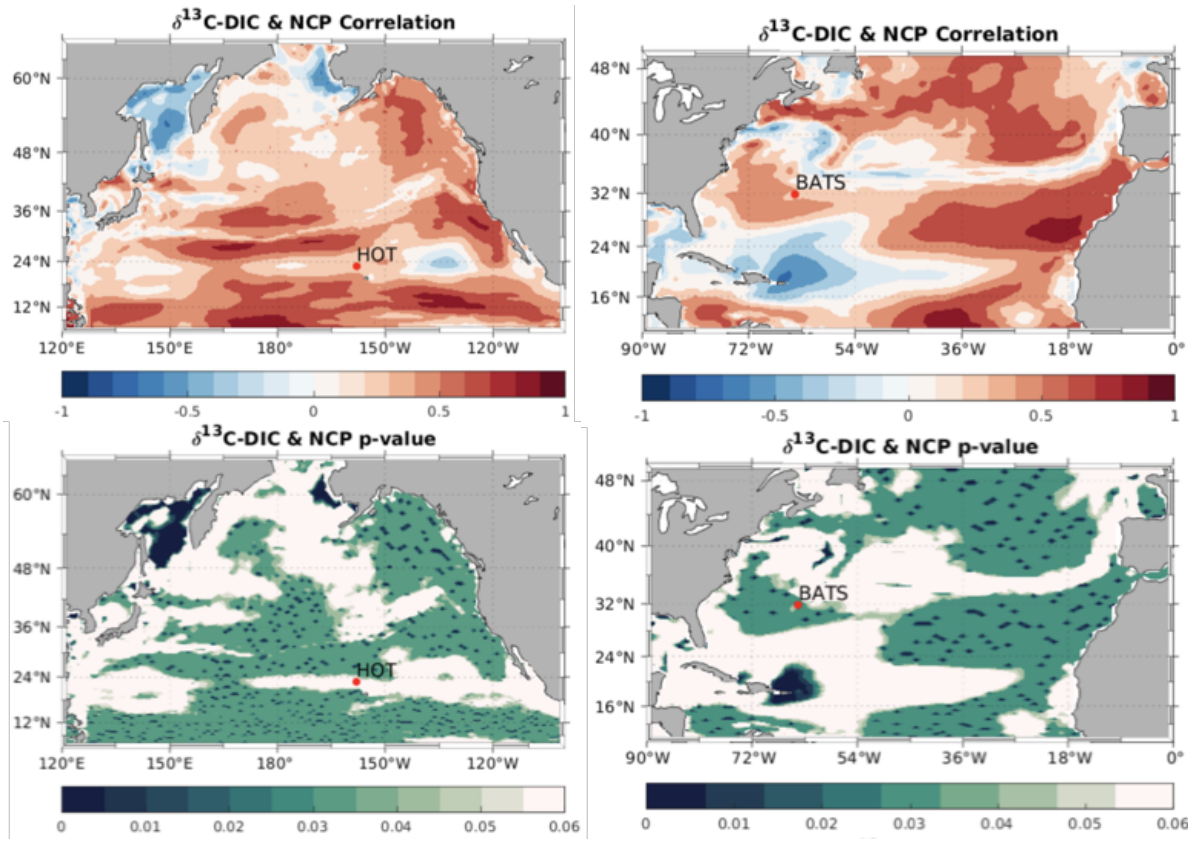

Figure 4.9: Correlation between δ^{13}C-DIC and NCP at each grid cell.

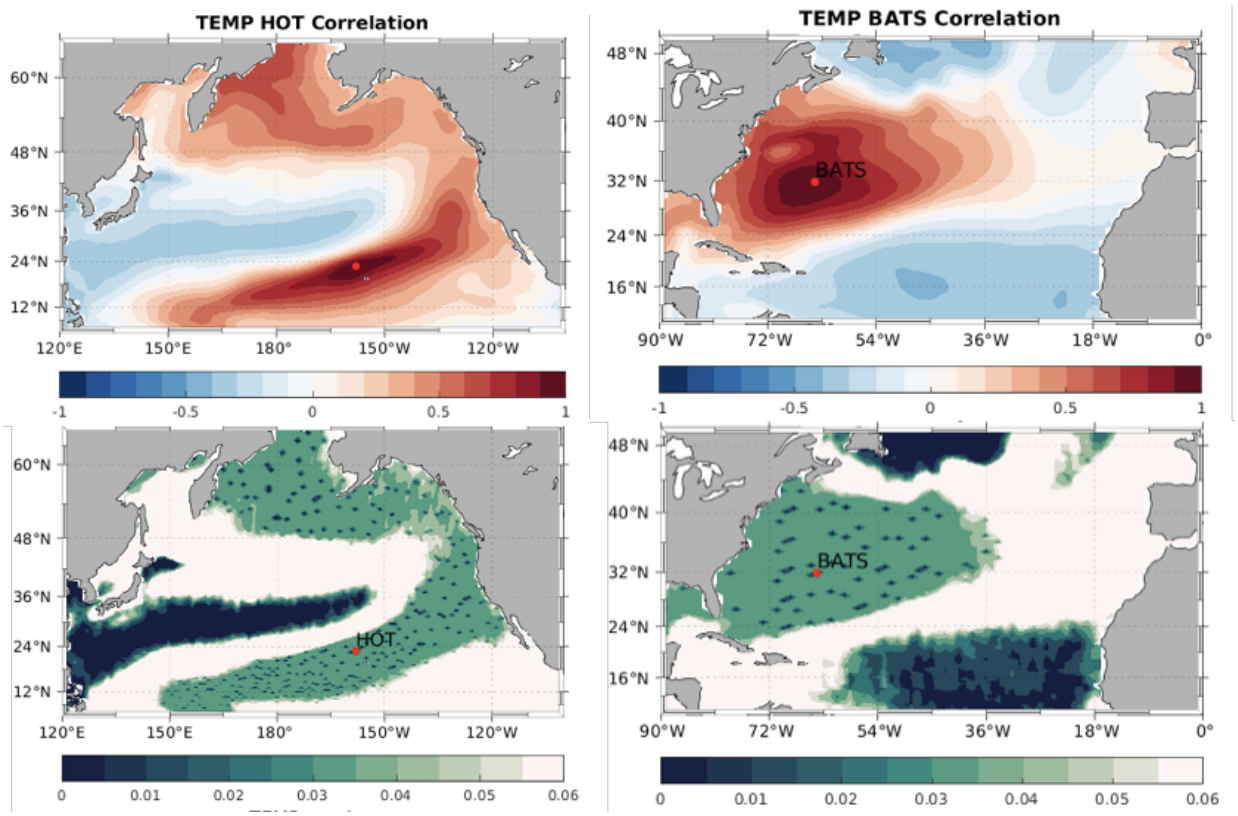

Figure 4.10: Correlation between SST at HOT (left) and BATS (right) with the surrounding region.

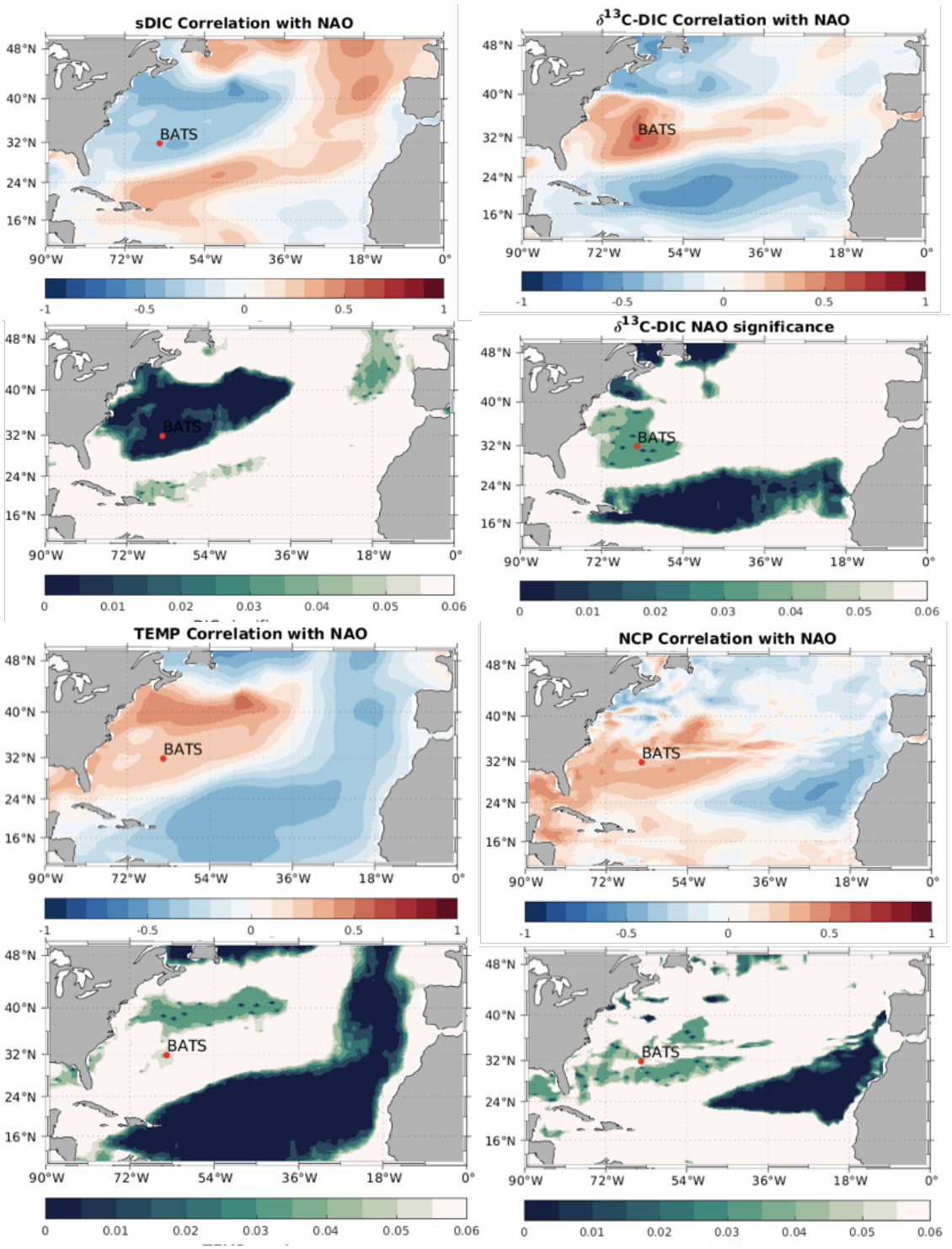

Figure 4.11: Correlation coefficients between the NAO index and sDIC, δ^{13}C-DIC, SST, and NCP are shown in red/blue maps. Areas of significant correlation (above the 95th percentile threshold) are shown in teal/blue maps below their respective correlation coefficient maps.

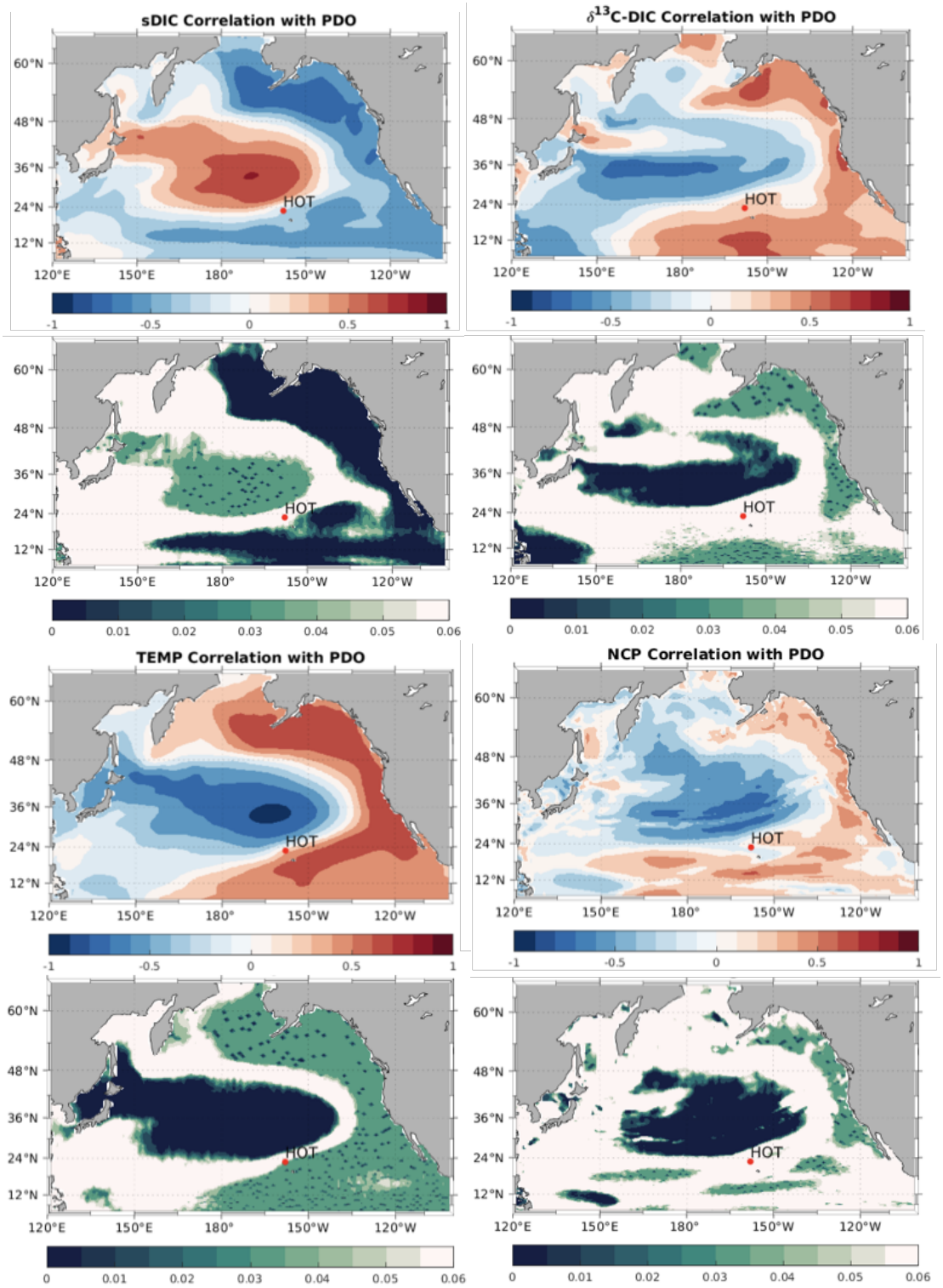

Figure 4.12: Correlation coefficients between the PDO index and sDIC, δ^{13}C-DIC, SST, and NCP are shown in red/blue maps. Areas of significant correlation (above the 95th percentile threshold) are shown in teal/blue maps below their respective correlation coefficient maps.

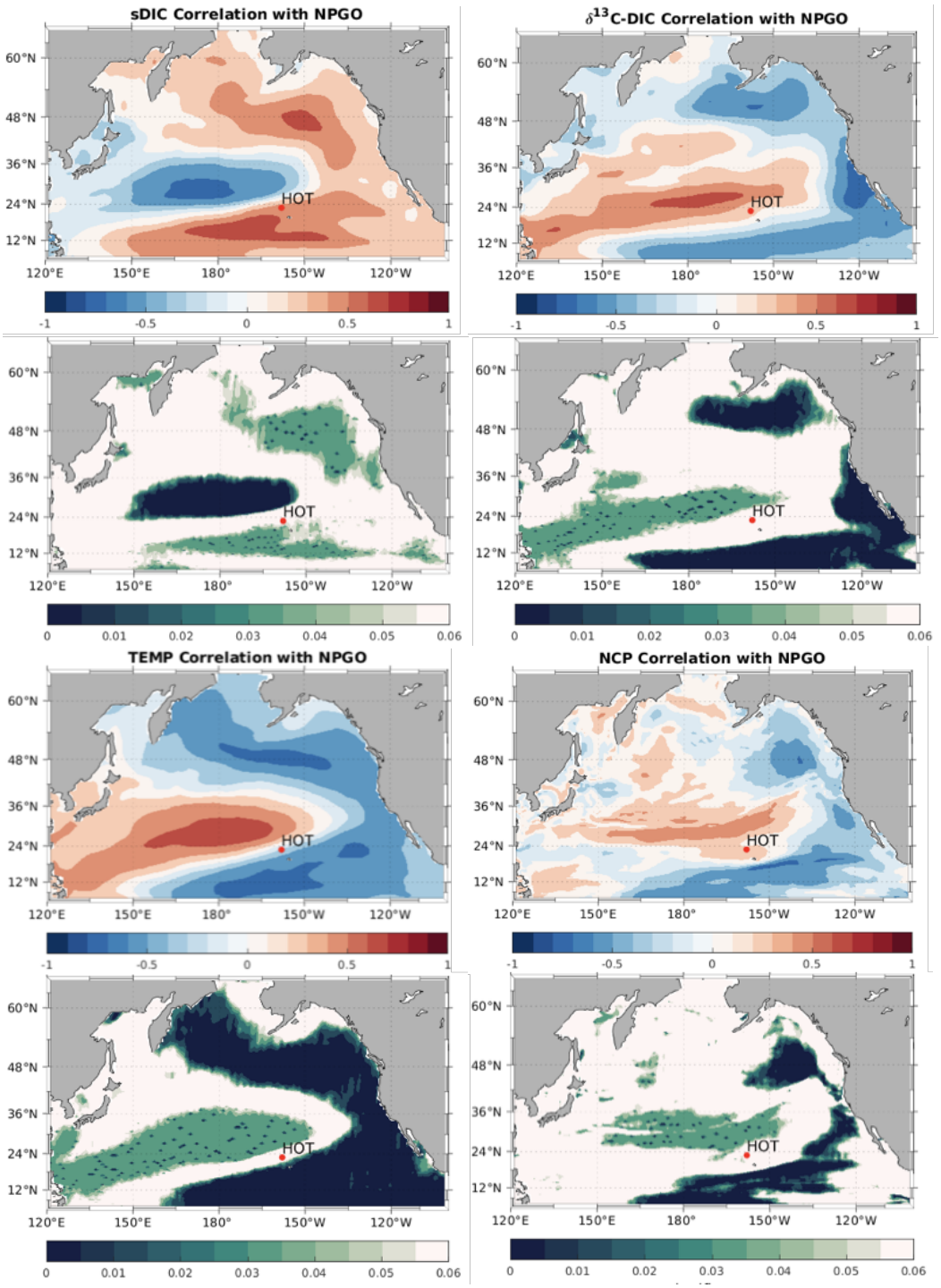

Figure 4.13: Correlation coefficients between the NPGO index and sDIC, δ^{13}C-DIC, SST, and NCP are shown in red/blue maps. Areas of significant correlation (above the 95th percentile threshold) are shown in teal/blue maps below their respective correlation coefficient maps.

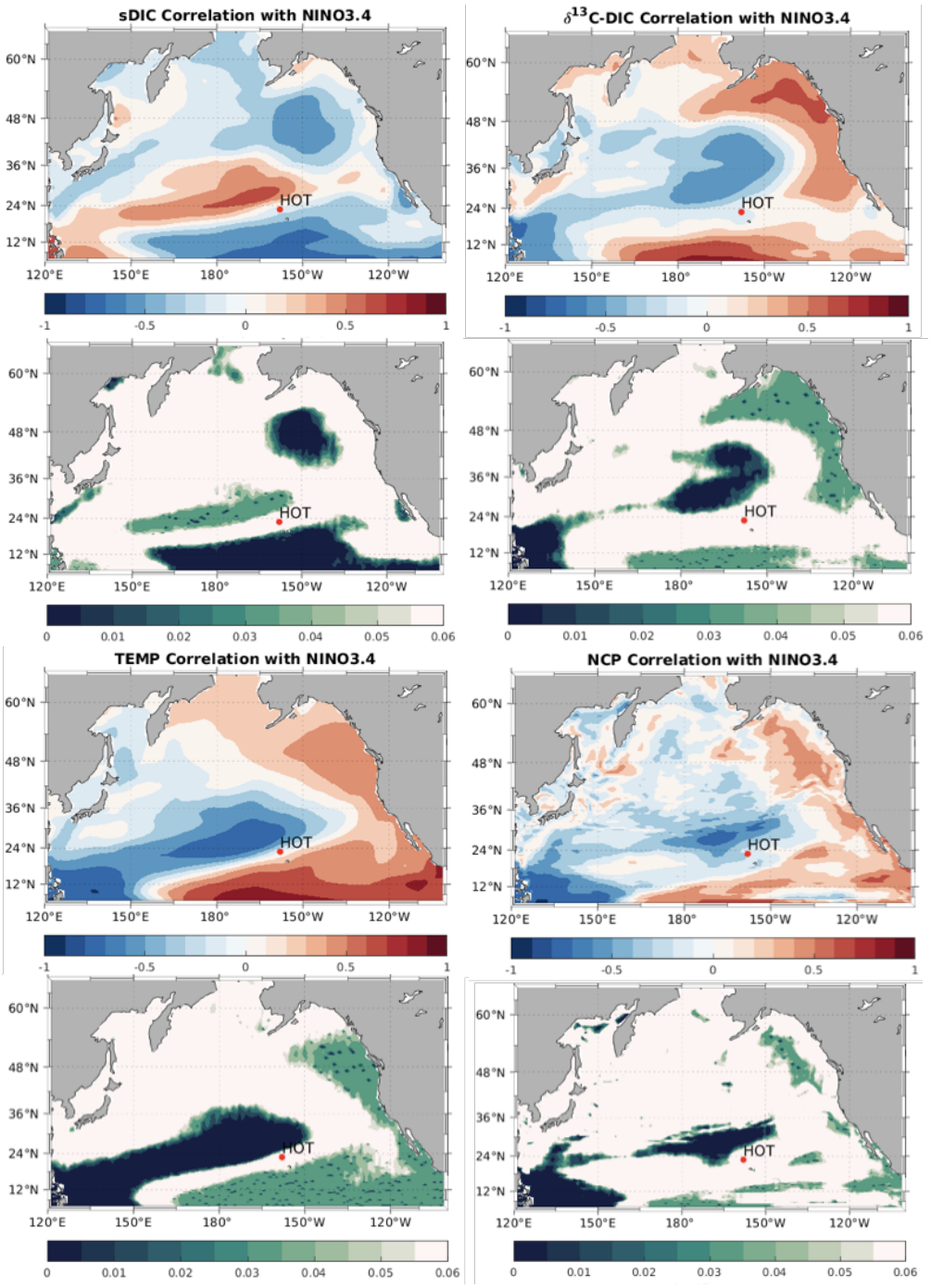

Figure 4.14: Correlation coefficients between the NINO3.4 index and sDIC, δ^{13}C-DIC, SST, and NCP are shown in red/blue maps. Areas of significant correlation (above the 95th percentile threshold) are shown in teal/blue maps below their respective correlation coefficient maps.

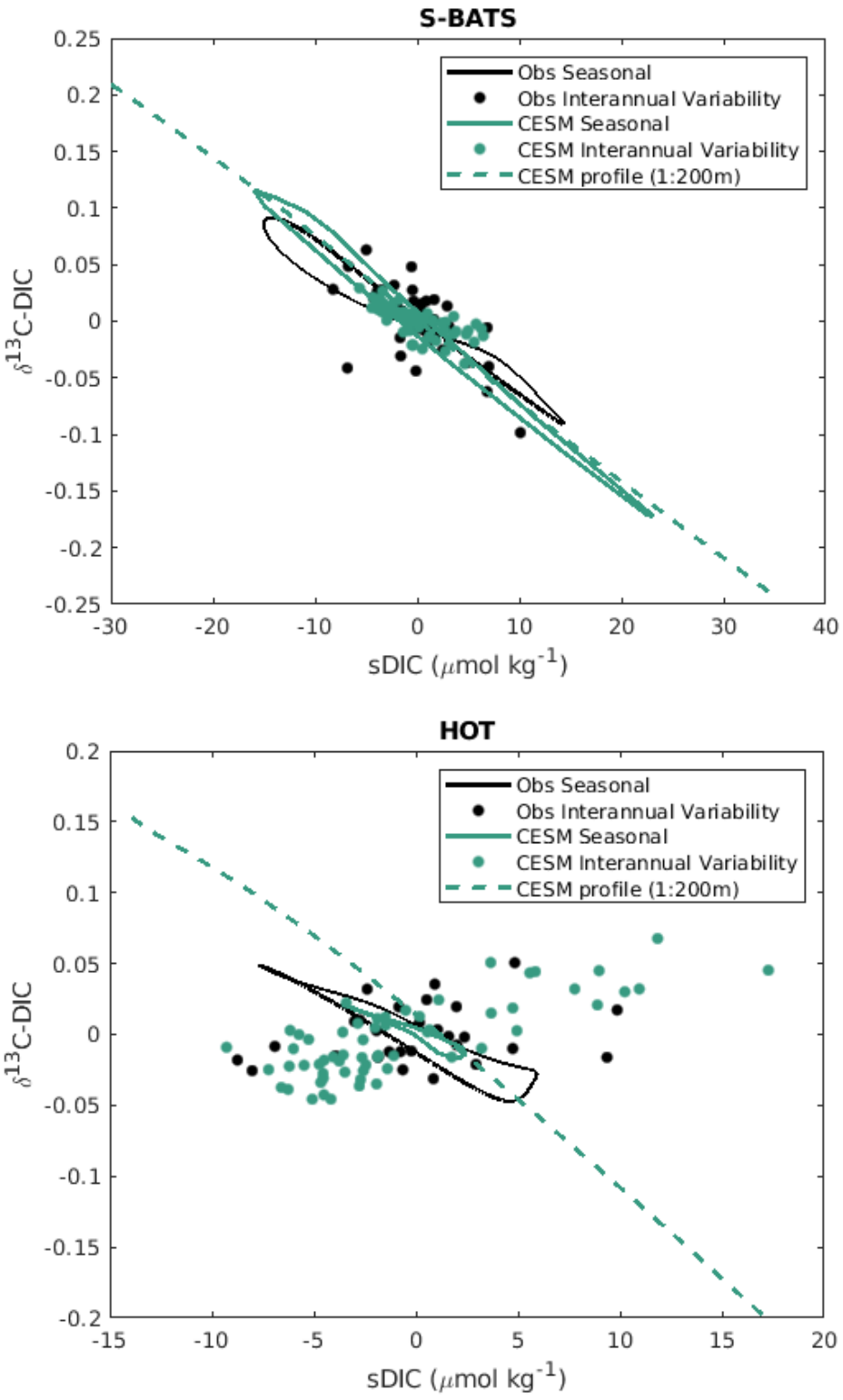

Figure 4.15: Property property plots of sDIC and δ^{13}C-DIC at HOT and S-BATS showing seasonal cycle, annual mean interannual variability, and vertical profile down to 200m. Observations are shown in black and CESM output shown in teal.

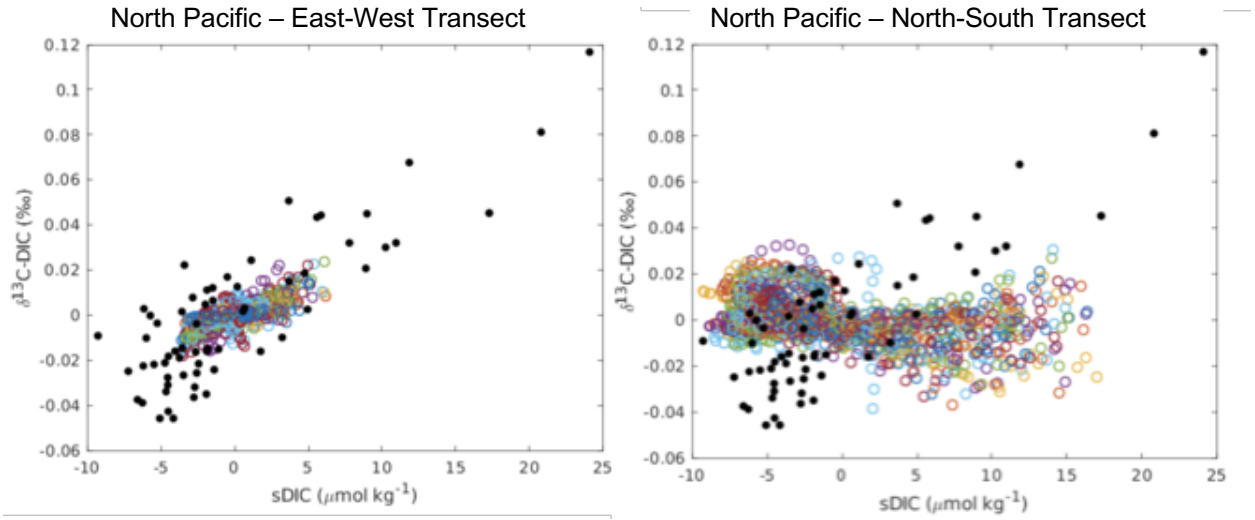

Figure 4.16: Black dots are interannual variability of sDIC and δ^{13}C-DIC at HOT shown as teal in Figure 4.15. Colored open circles show spatial transects through HOT, each color representing a different year. East-West transect (left) between ~169W to ~147W along ~22N. North-South transect (right) between ~18N to ~30N along ~158W.